TIME-LAPSE RESISTIVITY LOG RESPONSES IN HORIZONTAL WELLS, NAMORADO RESERVOIR, ALBACORA FIELD, OFFSHORE BRAZIL

by

Ricardo M. R. Gomes

ProQuest Number: 10794459

ProQuest 10794459

A thesis submitted to the Faculty and the Board of Trustees of the Colorado School of Mines in partial fulfillment of the requirements for the degree of Master of Science (Geology).

Golden, Colorado

Date 08 - 30 - 99

Signed: _____
Ricardo M. R. Gomes

Approved: _____
Dr. Neil F. Hurley
Thesis Advisor

Golden, Colorado

Date 9/1/99

_____
Dr. Roger M. Slatt
Professor and Head
Department of Geology and
Geological Engineering

ABSTRACT

The Upper Albian Namorado reservoir of Albacora field, offshore Brazil, is composed of sandstone turbidites with thin (20-30 cm) zones completely cemented by calcite. These internal reservoir heterogeneities interfere with fluid flow in the reservoir, resulting in non-economical oil productivity from conventional wells. Two horizontal wells were drilled to improve oil productivity in the Namorado reservoir. In both wells, resistivity log anomalies caused by electrical anisotropy and polarization horn effects, are related to the presence of calcite-cemented zones. Electrical anisotropy occurs when the resistivity measured in one direction in a formation is different from that measured in another direction. Polarization horns are spikes of resistivity tool response that occur on the layer boundaries in highly deviated and horizontal wells.

Time-lapse measurements made with a logging while drilling (LWD) 2 MHz resistivity tool in a horizontal well filled with salt-saturated mud were used to study the evolution of polarization horns and electrical anisotropy as a function of invasion. A petrophysical model of the reservoir, based on well logs and cores in a vertical well, was constructed to simulate resistivity log responses in vertical and horizontal wells. For that purpose, the Coates free fluid and Archie equations were used to calculate resistivities from mini-permeameter, porosity and rock type data. A conceptual invasion model was

applied in 1D and 3D tool-response modeling programs to understand the polarization horn effect. Results show that polarization horns develop at the boundary between high resistivity cemented layers and permeable reservoir sandstones after invasion by a conductive mud filtrate.

The petrophysical model was further used to quantify electrical anisotropy caused by intervals with or without calcite cementation, and to study the relationships between permeability and resistivity for the two types of layering in the reservoir. Results show that electrical anisotropy related to depositional processes and electrical anisotropy caused by calcite cementation are affected in different ways by hydrocarbon saturation. The electrical anisotropy related to depositional processes tends to disappear with increasing water saturation, whereas the electrical anisotropy caused by calcite-cemented layers increases when water saturation increases. Horizontal permeabilities, calculated from the arithmetic average of the permeabilties of individual layers, agree very well with the permeabilities obtained from the Coates and Archie equations using vertical resistivities. This correlation is valid for reservoirs with electrical anisotropy originated both by depositional causes or calcite cementation. Using the same approach, vertical permeabilities from the harmonic average of individual layers were compared to the permeabilities from Coates and Archie equations using horizontal resistivities. In the reservoirs with electrical anisotropy related to calcite-cemented layers, the presence of these high resistivity intervals strongly influences vertical permeability, preventing a good correlation.

An integrated forward modeling program was used to simulate polarization horns along two horizontal well trajectories. The purpose of this work was to match observed and simulated log traces, thereby confirming the validity of the geologic and invasion models that were developed for the Namorado reservoir.

TABLE OF CONTENTS

LIST OF FIGURES

LIST OF TABLES

LIST OF APPENDICES

* Electronic files with appendices are in attached floppy disks.

ACKNOWLEDGMENTS

Finally, I would like to express my deepest gratitude to my wife, Marisa, and my children, Marcos and Flávia, for all their love, emotional support and patience. This thesis is dedicated to them.

CHAPTER 1.

INTRODUCTION

The use of horizontal wells for exploration and development of oil and gas fields has increased tremendously in the last 15 years. The reason for this dramatic growth can be summarized in one small phrase: Optimization of profitability. A proper application of horizontal well technology will result in higher production rates, greater recoveries, and a reduction of the number of platforms or wells required to develop a field. In the future, predictions are for continued growth of this technology as new technical improvements, added to a gain in experience, result in even more economical and technical successes worldwide.

The advent and increasing growth of the horizontal well technique came along with new challenges leading to technical innovation in all segments of the activity. In the formation-evaluation realm, horizontal wells have prompted the development of new tools and methodologies for obtaining and interpreting logs in this new kind of environment. The current challenge is to understand what log measurements mean when obtained in a horizontal position. Betts et al. (1990) stated: "Interpreting logs from a horizontal well requires a new way of thinking, since established interpretation models may not work. Interpretation transforms assume radial symmetry around the well bore,

whereas in the horizontal well, radial anisotropy is the very thing you are looking for." The task is to understand what log measurements mean when the tools are positioned parallel to the bedding and when invasion is asymmetric, due to gravity effects or permeability anisotropy.

Resistivity logs, because of their depth of investigation, are particularly affected by the horizontal well logging environment. Electrical anisotropy, shoulder bed and apparent dip effects are the main features normally observed in resistivity measurements along highly deviated and horizontal wells. These effects can act alone or combined, and will also be affected by invasion of mud filtrate, which further complicates the log interpretation. If logging while drilling (LWD) tools with time-lapse runs are available, the invasion component can be isolated. This provides an opportunity to depict its effects on the log measurements. However, most of the time, resistivity-modeling programs are necessary to achieve a correct log interpretation in this kind of environment.

The purpose of this thesis is to study resistivity log responses in two horizontal wells drilled through a turbidite sandstone reservoir in the Albacora field of the Campos basin, offshore Brazil. Time-lapse logs from a LWD 2MHz resistivity tool proved to be the key for establishing relationships between major reservoir heterogeneities and the evolution of polarization horns and electrical anisotropy with invasion.

1.1- Horizontal Wells in the Albacora Field-The Log Interpretation Problem

.The history of horizontal well drilling in the Brazilian state oil company (Petrobrás) started in the 1980's, when some horizontal wells were drilled experimentally. The positive results encouraged Petrobrás to design development programs using this technology in onshore and offshore fields.

The first offshore project occurred in the Namorado reservoir of the Albacora field, Campos basin (**Figure 1**). In this deep water area (water depths range from 250 to 2,000 m), Upper Albian turbidite sandstones occur saturated with good quality oil (25° to 30° API), but the reservoir is affected by diagenetic heterogeneities in the form of calcite-cemented layers. Cemented layers interfere with fluid flow in the reservoir, resulting in non-economical oil productivity from vertical wells. Technical and economic studies indicated that viable commercial production would only be achieved by the use of horizontal wells together with a water injection program. So, a development strategy including 7 horizontal producers and 6 vertical injectors was delineated for the reservoir. Location of the first two horizontal wells and offsetting vertical wells is shown in the structural map of the Namorado reservoir (**Figure 2**).

The first horizontal well (ABH-1) was successfully drilled with brackish mud and logged using a pipe-conveyed technique with standard logging tools. Despite normal logging operations and tool calibrations, the induction resistivity readings presented higher mean values than similar logs from the previous vertical wells in the Namorado
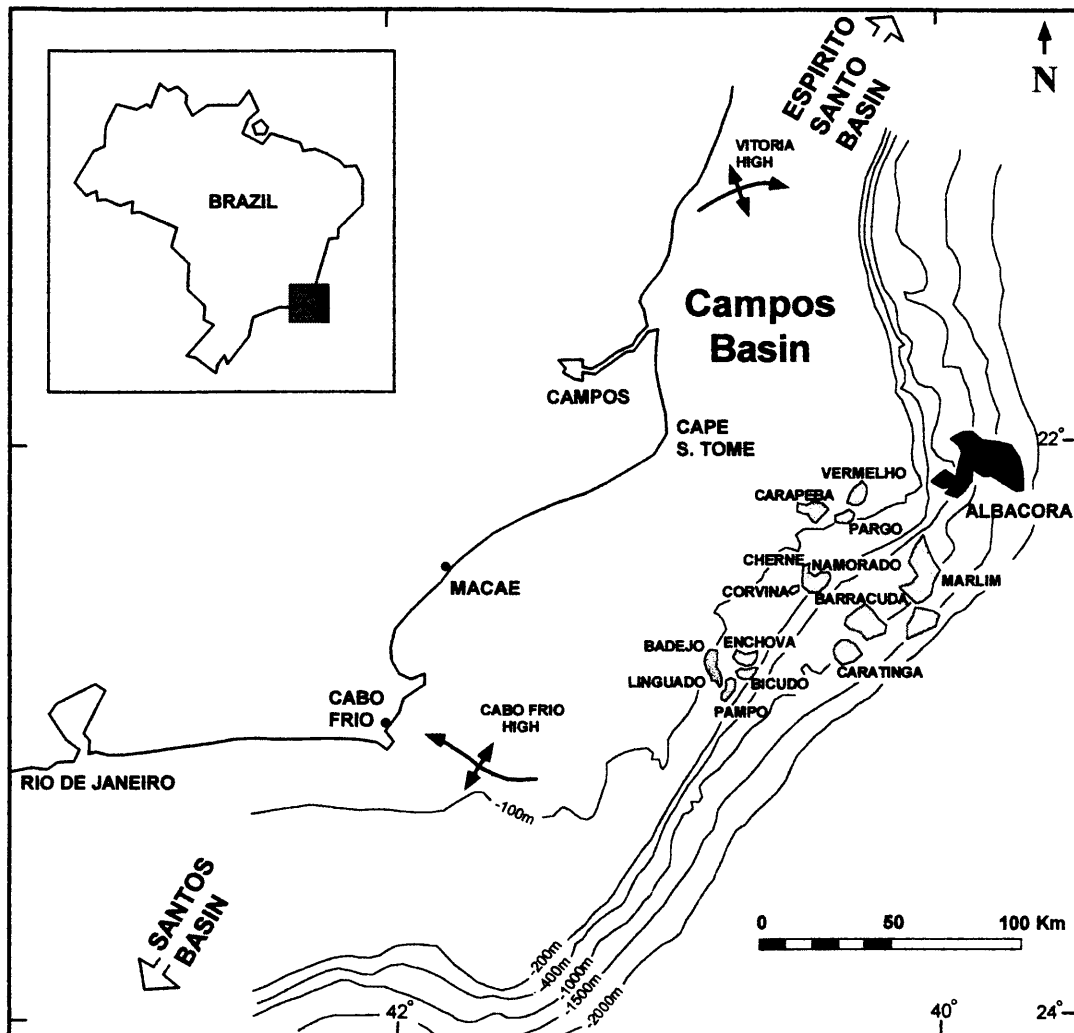
Figure 1 - Index map with location of Campos basin and Albacora field, offshore
Brazil. Adapted from Guardado et al. (1990).
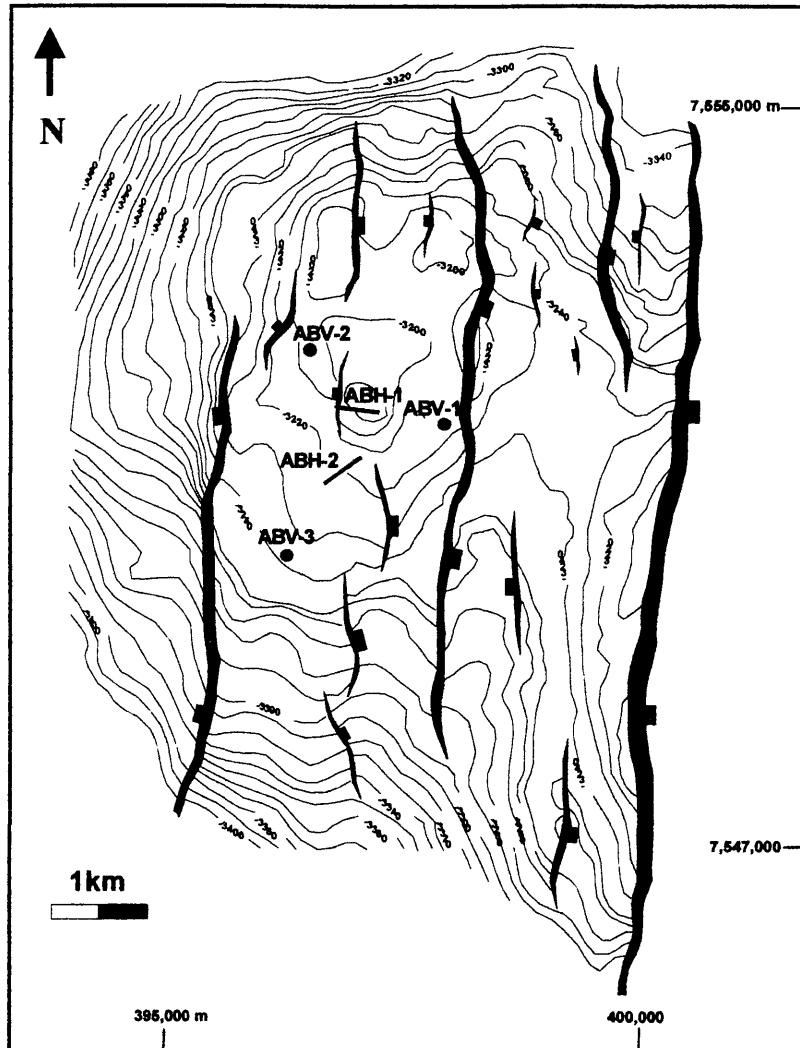
Figure 2 - Structural map of the Upper Albian reservoir in the Albacora field, showing the location of horizontal wells ABH-1 and ABH-2, and offsetting vertical wells ABV-1, ABV-2 and ABV-3. The dark lines are faults with the tick mark on the downthrown side. Contour interval is 10 m. UTM north-south zone 24 (from Petrobrás, 1997).

reservoir, and abnormal resistivity spikes occurred throughout the logged reservoir interval (**Figure 3**).

The second horizontal well (ABH-2) was drilled with salt-saturated mud and logged using a LWD 2MHz resistivity tool. Seven time-lapse logs were obtained between 60 and 1120 hours after drilling. Later logging passes showed growing resistivity spikes with increasing elapsed time. In the initial LWD logs, these spikes were absent. Resistivity readings were locally higher than previous vertical wells, and separation was pronounced between deep and shallow resistivity curves (**Figure 4**).

1.2- Research objectives

The primary objective of this research is to explain the anomalous resistivity log responses in the horizontal wells drilled through the Namorado reservoir of Albacora field, improving the knowledge of the main effects acting in the horizontal well logging environment.

To this end, the study is divided into six steps: (1) Discuss the main environmental effects acting in horizontal wells, and their influence on log interpretation for different types of resistivity logging tools. (2) Provide an overview of the geologic setting for the Upper Albian deep-water reservoirs in the Albacora field, with their sedimentology, depositional environment, stratigraphy, reservoir quality and internal heterogeneities. (3) Perform reservoir characterization for the turbidite reservoirs. Logs, cores and mini-permeameter data were integrated to establish geologic correlation
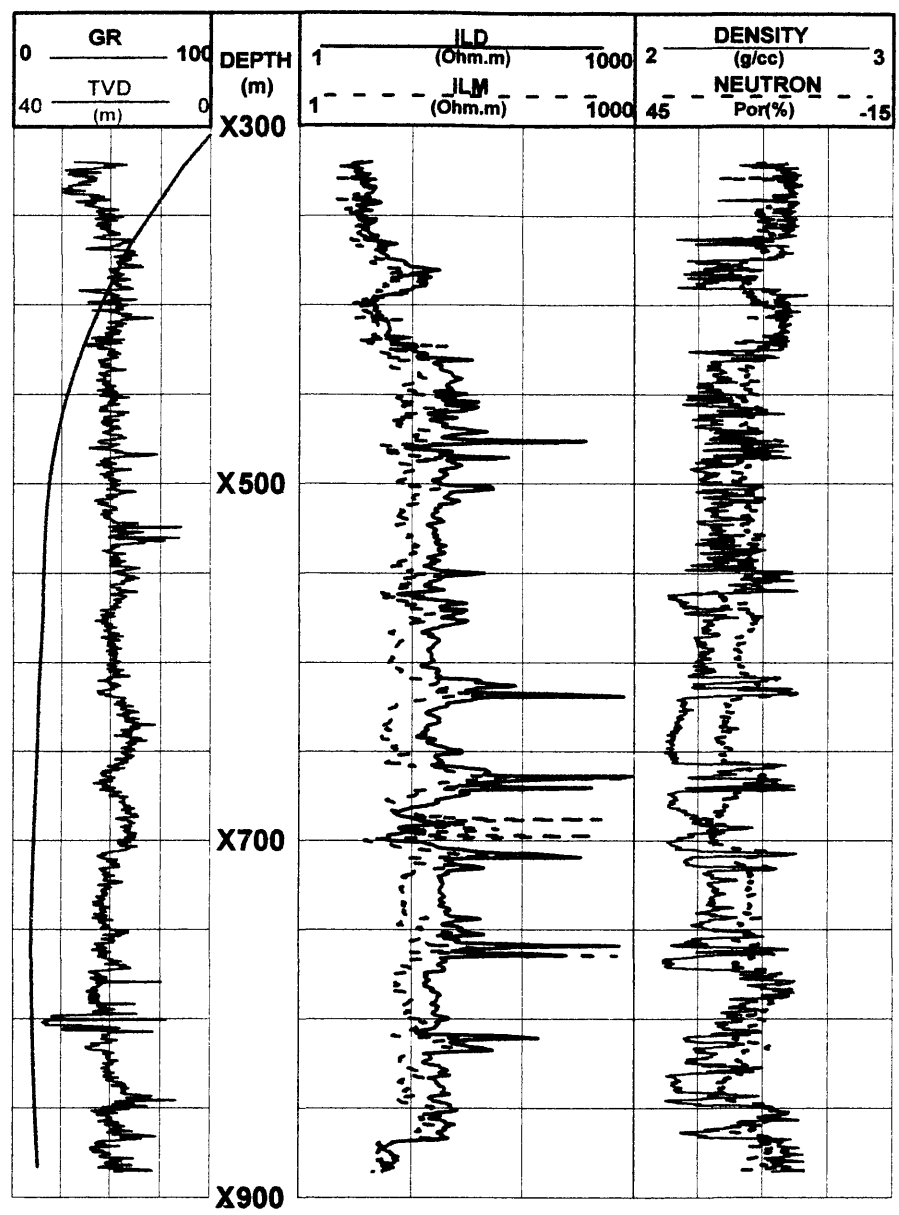
Figure 3 - Wireline logs in ABH-1 well. Spikes on resistivity curves occur throughout the drilled section of the reservoir (X425 - X875 m). Resistivities are plotted on a semi-log scale. The TVD scale represents the relative vertical depth variation along the horizontal trajectory in the reservoir.
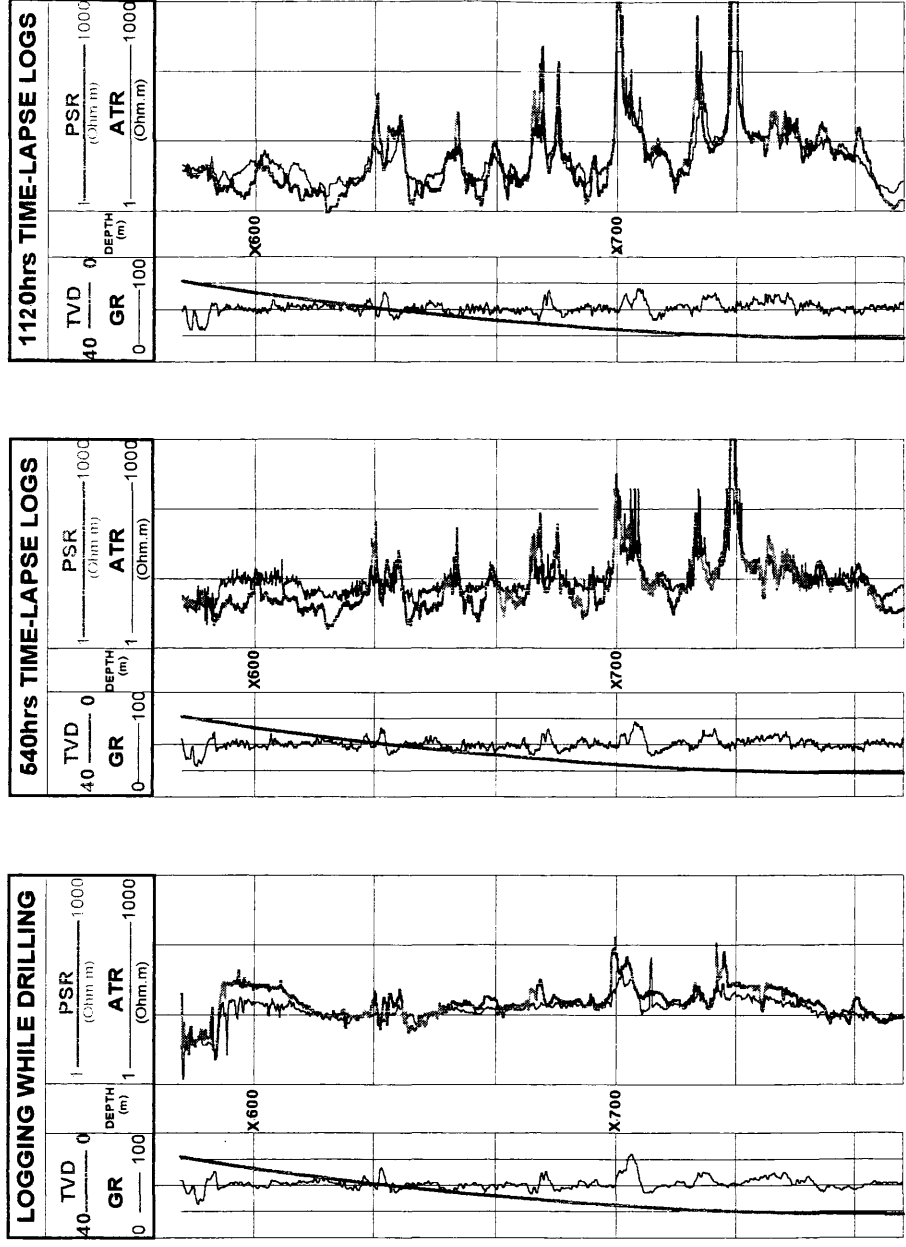
Figure 4 - Initial LWD (left) and time-lapse logs in the ABH-2 horizontal well, showing a growing pattern of resistivity spikes for increasing elapsed time. In the initial LWD logs, the horns are absent. Only small spikes occur, associated with low porosity layers. In several intervals, the PSR reads higher values than the ATR curve. The well was drilled with a salt-saturated mud. Resistivities are on a semi-log scale. The TVD scale represents relative vertical depth variation along the horizontal trajectory in the reservoir.

between vertical and horizontal wells, and to obtain a petrophysical model along the reservoir units. (4) Present the results of resistivity modeling programs, where the established petrophysical model and a conceptual invasion model are used to reproduce the effects observed on field resistivity logs of horizontal wells. The evolution of polarization horns with invasion is discussed, using different time-lapse log signatures of a 2 MHz LWD resistivity tool. (5) Quantify electrical anisotropy from one offsetting vertical well. Discuss the evolution of electrical anisotropy with invasion and the relationships between permeability and resistivity. (6) Integrate the results of the study in a forward modeling program to simulate resistivity log responses along the trajectory of two horizontal wells and check the proposed models.

1.3 - Database and Methodology

The database for this study was provided by Petrobrás (Petróleo Brasileiro S/A) and is summarized in **Table 1**. Data from five wells (three vertical and two horizontal) drilled by Petrobrás in the Albacora field, as well as seismic sections and a structural map were used to construct geologic cross-sections along the trajectories of two horizontal wells. A petrophysical model for the Namorado reservoir was built based on cores and logs from one of the vertical wells.

The database includes about 15,000 meters of electrical logs (wireline and LWD) run by Schlumberger/Anadrill or Halliburton; descriptions of 230 meters of cores made

by Petrobrás geologists; color photos and porosity/permeability measurements from plugs and by using a mini-permeameter.

Methodology used included:

1- Correlate between vertical and horizontal wells to construct geologic cross-sections along the path of the horizontal wells.

2- Integrate well logs, core descriptions, mini-permeameter and petrophysical data from offsetting vertical wells to differentiate lithologic classes on core photos.

3- Use the Coates free fluid and Archie equations to convert mini-permeameter and porosity measurements to resistivity values in order to obtain a squared resistivity profile along the reservoir.

4- Define a conceptual invasion model, applied in resistivity modeling programs (1D and 3D) to reproduce the environmental effects observed in 2MHz LWD resistivity logs with time-lapse runs.

5- Quantify vertical and horizontal resistivities and permeabilities from the established petrophysical model to study the evolution of anisotropy with invasion and to define permeability / resistivity relationships.

6- Use an integrated forward modeling program to reproduce induction and 2MHz resistivity logs along the path of the two horizontal wells.

Table 1: Database for the study with total depth (T. D.) of wells and total interval of logs in meters. CDR is the compensated dual resistivity tool.

Well	T.D. (m)	Wireline					LWD		Core (m)	Seismic Section	Structural Map
		Resistivity (m)	Gamma Ray (m)	Sonic (m)	Density/ Neutron (m)	Micro- Resistivity (m)	CDR (m)	CDR Time-lapse (m)			
ABV-1	3630	541	536	534	300	-	-	-	-		
ABV-2	3400	326	317	315	326	-	-	-	135		
ABV-3	3420	324	317	314	324	-	-	-	38		
ABH-1	3917	565	642	-	597	-	-	-	6		
ABH-2	4097	-	-	1989	1458	746	1989	2549	51		
TOTAL	18464	1756	1812	3152	3005	746	1989	2549	230	2	1

CHAPTER 2.

RESISTIVITY LOG INTERPRETATION IN HORIZONTAL WELLS:

THE ENVIRONMENTAL EFFECTS

The first step in log interpretation is a precise understanding of the various environmental effects on the tool response. In highly deviated or horizontal wells, several factors cause non-radial symmetry around the borehole. Laminated formations with highly variable properties give rise to anisotropy, geometric effects (shoulder beds and apparent dip) and asymmetric invasion, which are the main components of this non-conventional logging environment (**Figure 5**). Therefore, for log interpretation in horizontal wells, two features of tool response are of primary importance: the depth of investigation and whether the tool investigates all around the well, or is focused in one direction (Singer, 1991). Also, the mode of acquisition, real time or after drilling, and the type of tool must be known for correct log interpretation.

Resistivity tools measure several feet into the formation and, therefore, are most affected by heterogeneities above and below the horizontal borehole. Environmental effects will introduce errors in the resistivity measurements, varying according to the tool type and frequency. **Figure 6** shows a classification of the different resistivity tools according to the frequency of the electric or electromagnetic wave emitted into the
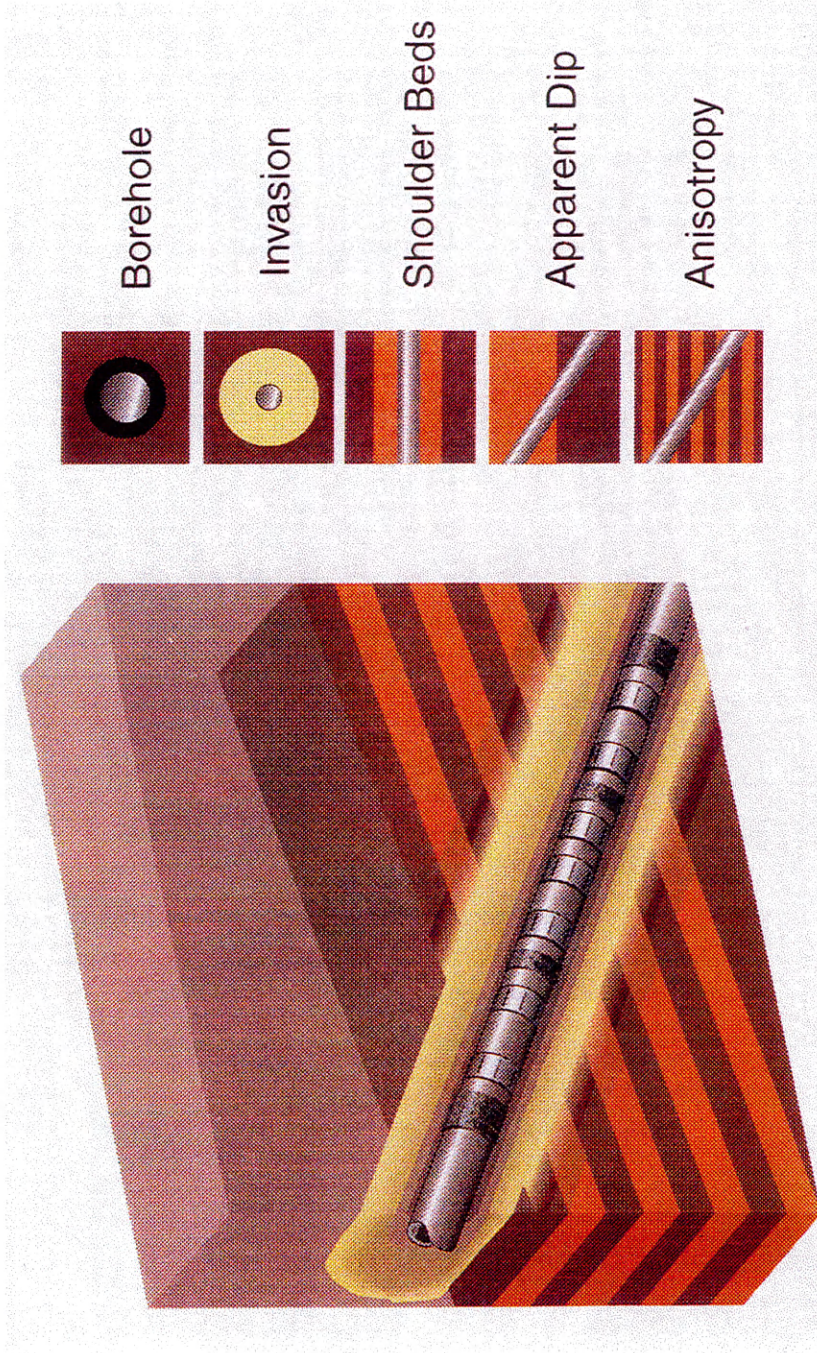
Figure 5 - Environmental effects acting in horizontal wells. Shoulder beds are beds above or below the horizontal well that may have an influence on signals recorded by a logging tool in that well. From Schlumberger (1997).
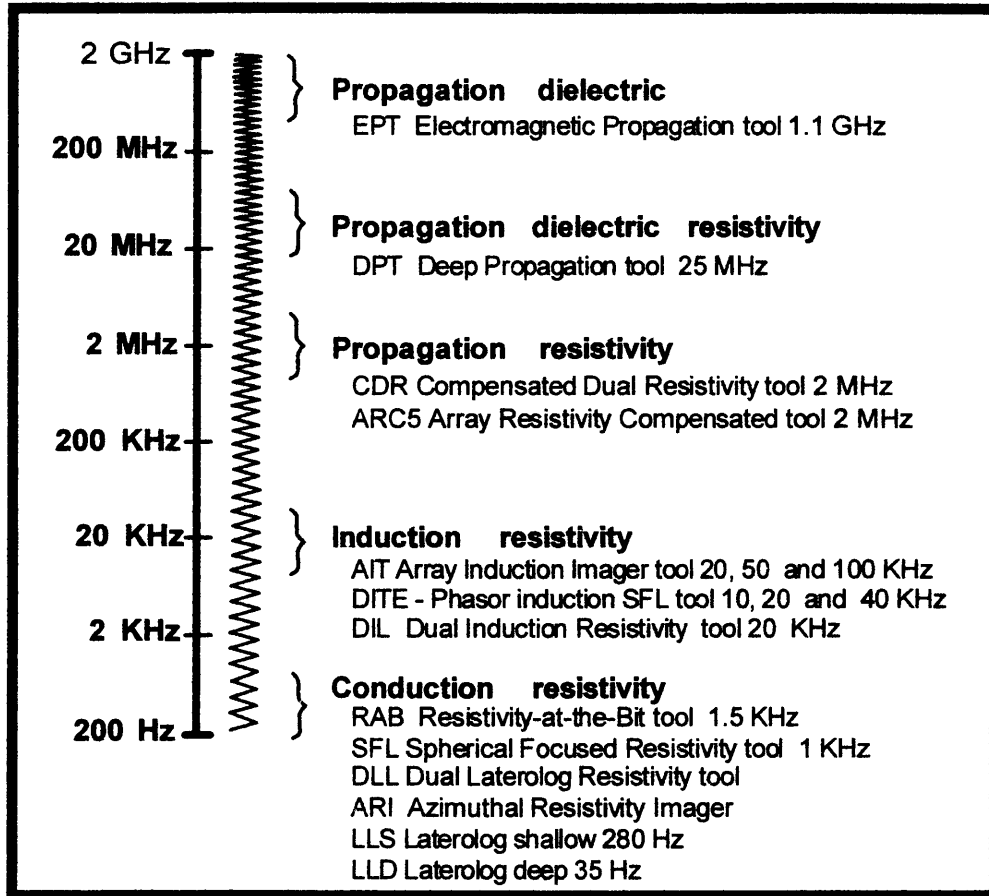
Figure 6 - Different resistivity tools according to the frequency of the electric or
electromagnetic wave emitted in the formation (Bonner et al., 1996).

formation. **Table 2** compares resistivity tools of different logging companies by tool type and frequency.

Electrical anisotropy, shoulder beds, relative dip and invasion are the main environmental effects on resistivity tool responses in horizontal wells. Two or more of these effects can contribute at the same time to alter the resistivity data.

2.1 - Electrical Anisotropy Effects

A formation is considered anisotropic when the magnitude of its physical properties varies in different spatial directions.

Sedimentary rocks are commonly deposited in horizontal layers of different composition with varying grain size and shape. As a consequence, they tend to exhibit some anisotropy in electrical, mechanical and fluid flow properties. Anisotropy may also be developed during processes that take place after deposition, such as diagenesis and mechanical deformation (Anderson et al., 1994). Most of the time, the formation parameters tend to be equal in the horizontal plane, parallel to the sedimentation, but differ in the vertical direction.

Electrical anisotropy and resistivity anisotropy are terms used to describe the situation in which the resistivity measured in one direction in a formation is different from that measured in another direction (Anderson et al., 1998). Sedimentary rocks normally have one resistivity parallel to the bedding plane, called horizontal resistivity (Rh) and a different resistivity perpendicular to the bedding plane, called vertical

Table 2 - Comparison table of resistivity tools for different logging companies. All mnemonics are defined in the nomenclature section at the end of the thesis.

Tool	Frequency		Schlumberger	Halliburton	Western
Electric	Wireline	35/280 Hz	DLL ARI HALS	DLL	DLL TBRT
		1 KHz	SFL MSFL MCFL	SFL	
	LWD	1.5 KHz	RAB		
Induction	Wireline	20 KHz	DIL	DIL HRI	DIFL
		10, 20 or 40 Hz	DITE		DPIL
		20, 50, 100 Hz	AIT		
	LWD	2 MHz	CDR ARC-5	CWRGD	

resistivity (Rv) (**Figure 7**). If the formation has a layered structure, Rv is normally larger

than Rh. The anisotropy, which depends on the size of the sample and the resolution of

the sampling method, can be defined as the ratio of Rv to Rh. The anisotropy coefficient

(λ) is also used to quantify electrical anisotropy:

$$\lambda = \sqrt{Rv/Rh}$$
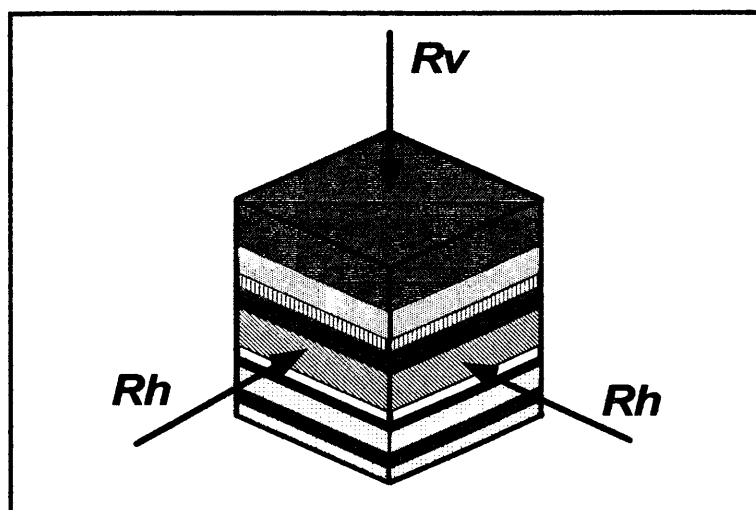
Figure 7 - Resistivity anisotropy in sedimentary rocks. Rv is normally higher
than Rh.

Electrical anisotropy occurs in sedimentary rocks mainly as a consequence of

depositional and or diagenetic processes. Depositional causes for resistivity anisotropy

are clean-sand anisotropy, grain anisotropy, shale anisotropy and sand-shale laminae

anisotropy (Chemali et al., 1987; Klein et al., 1995; Hagiwara, 1996; and Anderson et al., 1998).

Clean-sand anisotropy was first described by Klein et al. (1995). This form of anisotropy originates when clean sandstones have alternating thin beds of different grain size distributions. Variations in grain size often control capillarity and, as a consequence, the irreducible water saturation. Thus, in a hydrocarbon reservoir, water saturation of the finer grained layers will be higher than that of the coarser grained layers. This results in alternating resistive and conductive laminae with a very high anisotropy ratio. This is also termed macroscopic anisotropy since layer thicknesses are below the resolution of a standard induction or electrode resistivity device (Anderson et al., 1998).

Laboratory measurements and petrophysical models described by Klein et al. (1995) confirmed that water-wet formations with large variability in grain size between laminations could be highly anisotropic when oil or gas saturated, but nearly isotropic in the water leg or invaded zone. This dependence of anisotropy on fluid saturation is shown in **Figure 8**.

Another important conclusion from Klein et al. (1995) was the paradoxical relationship between resistivity and permeability in macroscopic anisotropic formations. This arises from both sand-shale laminations or grain size and capillarity variation in clean sands. In these cases, the authors observed that the horizontal permeability is proportional to the vertical resistivity and conversely, the vertical permeability is proportional to the horizontal resistivity.

Grain anisotropy results from the common orientation of plate-like clay grains parallel to the plane of deposition. The resulting pore structure allows current to flow more easily parallel than transverse to the bedding plane (Anderson et al., 1998). This property is referred to as microscopic anisotropy, because it is related to the micro-structure of the rocks (Chemali et al., 1987).

Shale anisotropy results from intercalations of layers with varying percentages of silt and clay, and is enhanced by the grain anisotropy of the clay minerals.
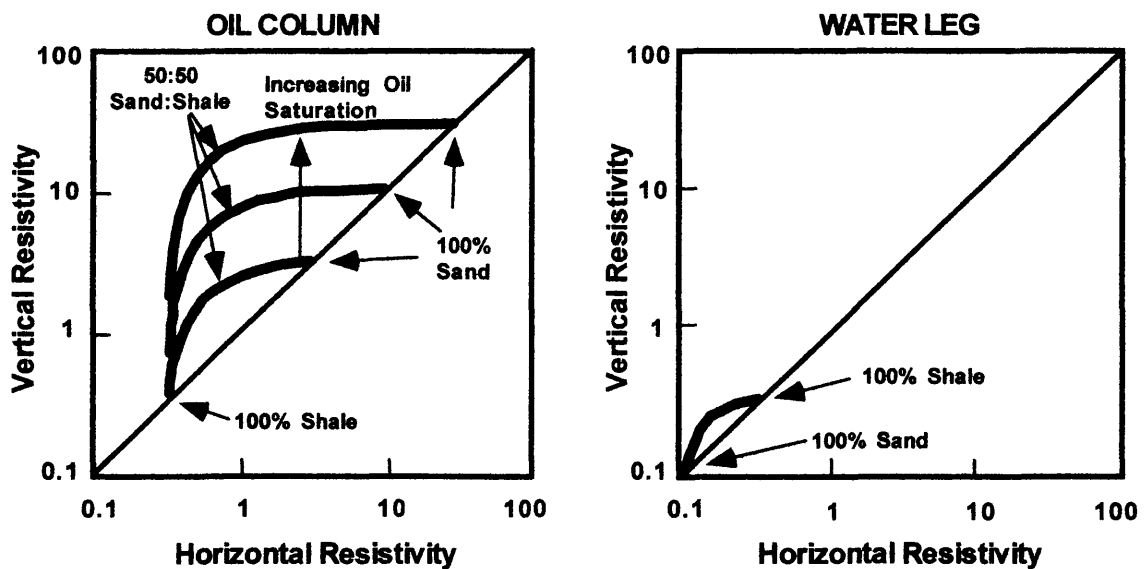
Figure 8 - Generalized plots of Rv versus Rh showing the dependence of anisotropy on fluid saturation. The same formation can be highly anisotropic when oil saturated, but nearly isotropic in the water leg (from Klein et al., 1995).

Laminated sand-shale sequences with lamina thickness below the logging tool's vertical resolution normally show what is called macroscopic anisotropy (Hagiwara, 1996). When the sand is hydrocarbon saturated, the ratio Rv/Rh can reach high values. Vertically, the layers will act like resistors in series, being mostly affected by the sand resistivity, while in the horizontal direction, the sequence of layers will appear as parallel resistors, mostly determined by the shale resistivity. In vertical wells this is one mechanism leading to the so-called low-resistivity pay (Anderson et al., 1998).

Diagenetic anisotropy results from intercalation of low porosity, high resistivity layers with porous sand layers. Carbonate cements are an important diagenetic constituent in sandstones, being one of the main causes of electrical anisotropy related to post-depositional processes.

Normally, the coefficient of anisotropy is much larger for macroscopic anisotropic formations than for microscopic anisotropic formations (Chemali et al., 1987). **Table 3** summarizes the main electrical anisotropy types, according to their origin, mechanisms, and expected Rv to Rh ratios.

Many researchers have addressed anisotropic effects on resistivity logs in recent years. Moran and Gianzero (1979) discussed the effects of formation anisotropy on the induction tool. Chemali et al. (1987) quantified the effects of shale anisotropy on laterolog and induction tools. Anderson et al. (1990 and 1995) studied the response of 2-MHz resistivity and induction tools in dipping beds and laminated formations. Klein (1991) and Hagiwara (1992) studied resistivity of anisotropic laminated sand-shale

Table 3: Electrical Anisotropy Types

ORIGIN	TYPE	MECHANISM	RESOLUTION SCALE	EXPECTED ANISOTROPY RATIO (Rv/Rh)	
				Hydrocarbon saturated reservoir	Conductive water saturated reservoir
	Clean Sand Anisotropy	Intercalation of layers of varying grain size and therefore of varying irreducible water saturation	Macroscopic	Very high	Nearly isotropic
	Grain Anisotropy	Non spherical, aligned grains, usually argillaceous minerals	Microscopic	Low. Varies depending on grain shape	
Depositional	Shale Anisotropy	Intercalation of layers with varying percentages of silt and clay; enhanced by grain anisotropy of the clay minerals.	Macroscopic	Low. Varies depending on shale composition	Low. Varies depending on shale composition
	Sand-Shale Anisotropy	Intercalation of clean sand layers with shale layers; enhanced by anisotropy of the shale layers.	Macroscopic	Medium	Low. Varies depending on shale composition
Diagenetic	Cemented Layer Anisotropy	Intercalation of low porosity, high resistivity layers with porous sand layers.	Macroscopic	Low	High

sequences for the induction tool. Lüling et al. (1994) discussed the processing and modeling of 2-MHz tools in dipping laminated anisotropic formations. Bittar and Rodney (1994) studied the effects of rock anisotropy on MWD electromagnetic wave resistivity sensors. Hagiwara (1994, 1995) discussed the response of induction and 2-MHz resistivity tools to shale anisotropy and thinly laminated formations. Klein et al. (1995) studied the petrophysics of electrically anisotropic reservoirs. Hagiwara (1996) presented a new method to determine horizontal resistivity in anisotropic formations. More recently Anderson et al. (1998) discussed the effect of crossbedding anisotropy on induction logs.

The effect of anisotropy on resistivity logs depends on the relative dip angle and the ratio between vertical and horizontal resistivities. The relative dip angle is defined as the angle between the borehole and the line normal to the bedding planes. Considering horizontally layered stratification, the relative dip angle will range from 0° in vertical wells to 90° in horizontal wells.

The magnitude of the anisotropy effect also varies with the type of resistivity logging tool, as a consequence of the distinct current flow paths and/or the different frequencies of the electromagnetic wave in the formation. Induction tools and LWD 2-MHz propagation devices cause current to flow in a loop around the borehole, in a plane that is perpendicular to the axis of the tool (**Figure 9**). In vertical wells, assuming thick- and flat-lying beds, these tools will measure only the horizontal resistivity, being blind to vertical resistivity. As the relative dip angle increases, from any combination of formation dip and borehole deviation, the measured resistivity grows to a value between

INDUCTION AND ELECTROMAGNETIC TOOLS
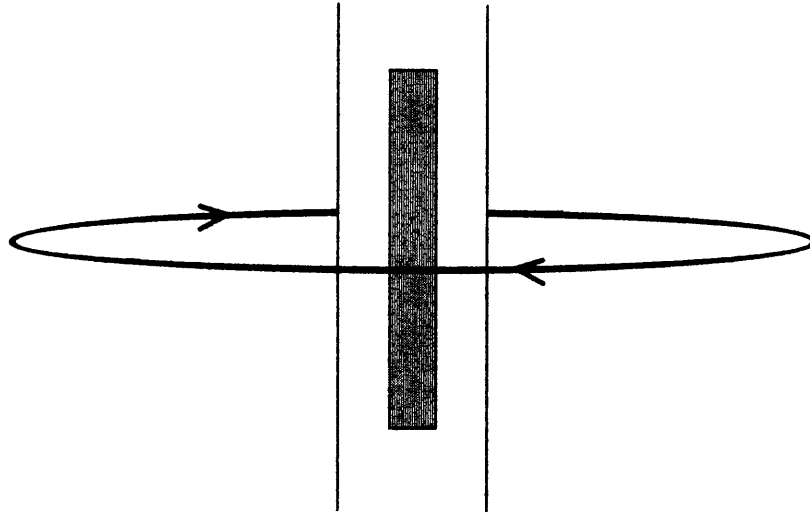
ELECTRIC TOOLS
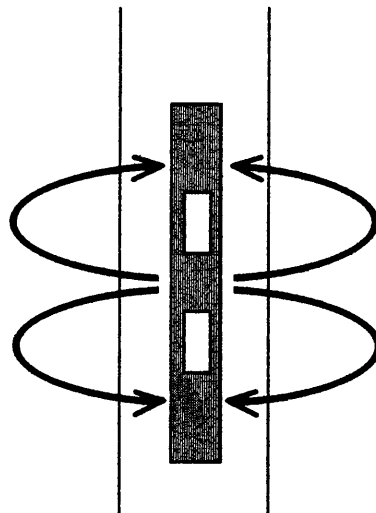
Figure 9 - Current flow paths for different resistivity tools. In induction and 2 MHz propagation tools, current flows in a loop around the borehole. In electric tools, current flows radially from an emitting electrode.

Rv and Rh. For wireline induction logs, the anisotropy effect is independent of coil spacing, appearing identical both to deep and medium induction logs (Hagiwara, 1994). For LWD 2-MHz propagation tools, the shallow phase shift measurement (PSR) and the deep attenuation measurement (ATR) will respond differently to the presence of anisotropy. The PSR measures the phase difference between receivers and the ATR measures the voltage attenuation between receivers. Because of its better vertical resolution, the PSR will read much higher resistivity than the ATR curve, separation being augmented at higher relative dip angles (**Figure 10**). As a consequence, the ATR and PSR curves at high relative dip angles can be processed using inversion to derive both the horizontal and vertical resistivities (Anderson et al., 1990; Bittar and Rodney, 1994; Hagiwara, 1994; Lüling et al., 1994).

In electric tools, such as wireline laterologs and LWD toroidal resistivity, the current flows radially outward in the formation from an emitting electrode on the tool. The current path is sometimes perpendicular and sometimes parallel to the borehole (**Figure 9**). Therefore, in vertical wells electric tools are sensitive to both horizontal and vertical resistivities. At large anisotropy coefficients, electric tools can easily read up to twenty percent higher than induction tools (Chemali et al., 1987). As the relative dip angle increases, the measured resistivities will increase proportionally with the amount of anisotropy. In general, for a given anisotropy, laterologs will read higher than induction logs when vertical, but less than induction logs when horizontal (**Figure 11**). LWD toroidal resistivity tools are affected by anisotropy in the same way as other electric tools.
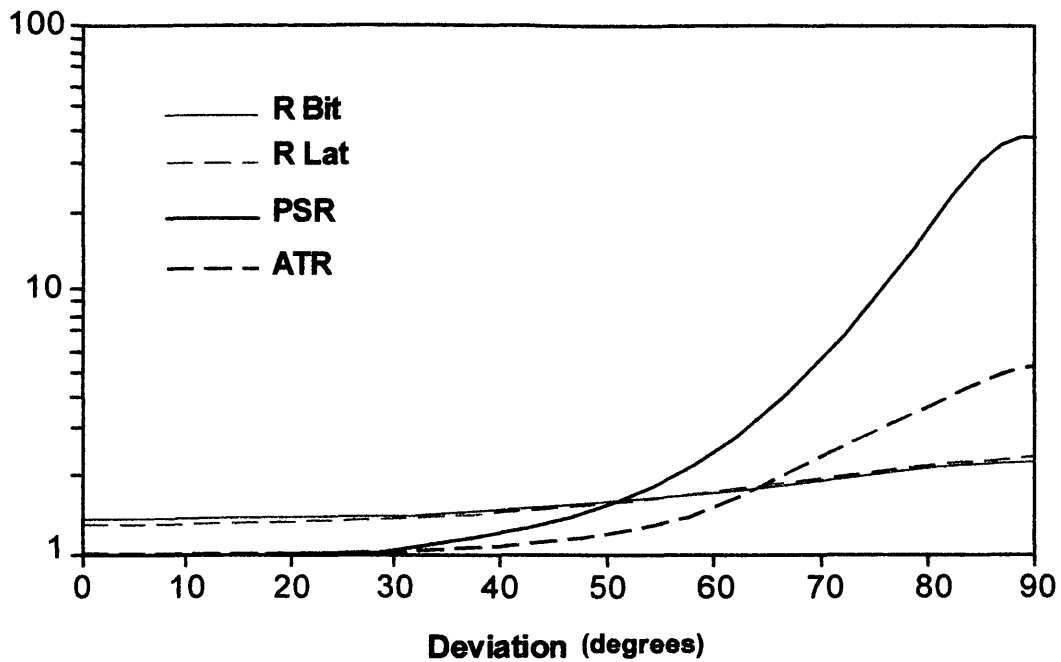
Figure 10 - 2 MHz propagation (PSR and ATR) and toroidal resistivity (Bit and Lat) tool responses to electrical anisotropy (Rv/Rh = 10) for varying hole deviation. Note the large resistivity range needed for the PSR curve (Schlumberger, 1995).
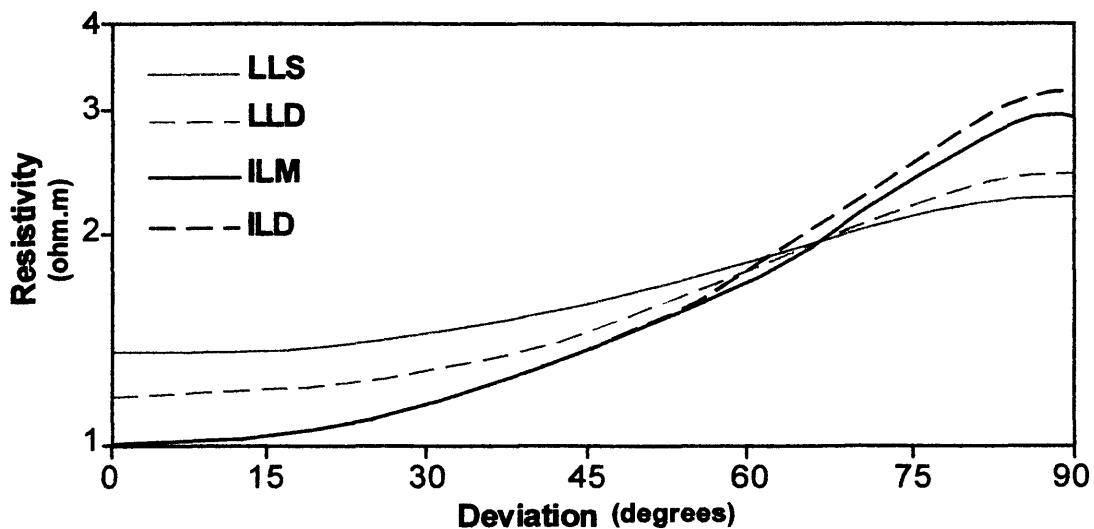
Figure 11 - Induction and laterolog tool responses to electrical anisotropy (Rv/Rh = 9) for varying hole deviation (Chemali et al., 1987).

In vertical wells, a small increase in resistivity is observed when compared to LWD propagation resistivity tools in anisotropic formations (**Figure 10**). In horizontal wells, measured toroidal resistivity can be as much as 4 times larger than Rh.

The effects of electrical anisotropy are particularly conspicuous for LWD propagation resistivity tools because the frequency of operation is much higher than it is for wireline induction or electric tools (Anderson et al., 1990; Hagiwara, 1996) (**Table 2**). Because anisotropic formations cause anomalously high resistivity readings in highly deviated and horizontal boreholes, calculated water saturations in horizontal wells can be too low, leading to overestimation of hydrocarbon reserves. Also, shale anisotropy may lead to erroneous geopressure gradient estimations (Hagiwara, 1996).

When anisotropy is the only factor affecting the resistivity measurements, it can be better identified and quantified from LWD logs. Techniques use the difference between the PSR and ATR curves for a fixed transmitter/receiver spacing (Anderson et al., 1990; Bittar and Rodney, 1994; Hagiwara, 1994 and 1996; Lüling et al., 1994), PSR or ATR curves from two different transmitter/receiver spacings (Bittar and Rodney, 1994; Hagiwara, 1994 and 1996), or PSR and ATR curves at two different frequencies (Hagiwara, 1994 and 1996). Once determined, the anisotropy coefficient can be used to characterize petrophysical properties of the reservoir that can be used to aid in well-to-well correlation. High anisotropy cofficients, in the presence of porous sediments, are good indicators of hydrocarbon pay, particularly thin-bedded, low resistivity pay (Klein

et al., 1995). Also, the inverted horizontal and vertical resistivities are used to model the resistivity tool response in horizontal wells.

2.2 - Geometric effects

2.2.1. Shoulder Beds

Adjacent beds, spaced closely to the wellbore, are known as shoulder beds. Resistivity tools, probing several feet into the formation around the borehole, are particularly affected by adjacent beds in horizontal wells. Unlike vertical wells, shoulder bed effects in horizontal wells are persistent along measured depth, asymmetric, and difficult to recognize.

Bed boundary effects can introduce significant errors in the resistivity measurements, leading to wrong oil-in-place and/or reserve calculations. However, these errors can be an asset if the objective is to signal an approaching bed or fluid contact, in a geosteering process (Gianzero et al., 1989).

Gianzero et al. (1989) investigated shoulder bed effects in horizontal wells for standard resistivity devices using tool response modeling. The response of a dual induction tool in a horizontal well near a bed boundary was computed via an analytic solution (**Figure 12**). Results of the modeling show that the induction curves detect an approaching resistive bed much more quickly than an approaching conductive bed. This is the reverse behavior when compared to a normal vertical situation. Also, differences in

depth of investigation between the deep induction (ILD) and medium induction (ILM) cause distinct responses to shouder bed effects for the two curves, leading to an observed separation.

The response of a dual laterolog tool in a horizontal well to the same bed boundary previously modeled is shown in **Figure 13**. In this case, because the borehole is an essential part of the problem, the tool response was computed using a numerical solution (Chemali et al., 1983). The results show that the dual laterolog is more sensitive to a nearby conductive bed than to a resistive bed. These response characteristics show that in horizontal wells, electric resistivity tools also reverse their behavior from the normal vertical well situation. The differences in depth of investigation between the laterolog deep (LLD) and laterolog shallow (LLS) curves cause separation between the two measurements.

The modeled responses of a LWD toroidal resistivity tool and a LWD 2-MHz propagation tool for the studied bed boundary are shown in **Figures 14** and **15**, respectively. As expected, the behavior of LWD resistivity tools in horizontal wells is similar to that of their correspondent wireline tools, and the same changes from a normal vertical situation are observed. For the LWD propagation tool, the differences in depth of investigation and vertical resolution between the PSR and ATR cause distinct shoulder bed effects and separation between the curves. The amount of separation is a function of relative dip angle, resistivity level and resistivity contrast (Anderson et al., 1990). **Figure 15** also points out an important artifact of induction type resistivity tools in horizontal
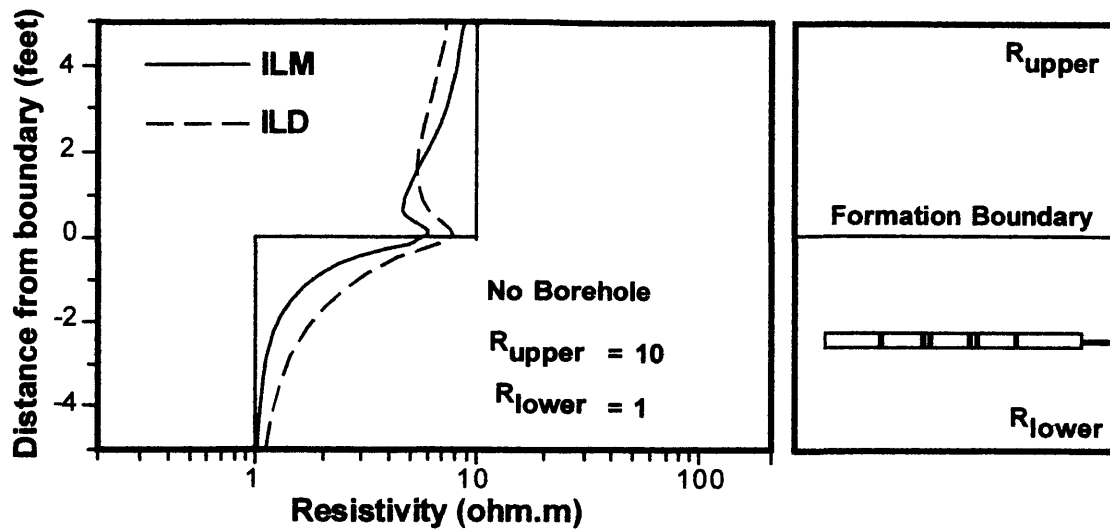
Figure 12 - Simulated response of a dual induction tool in a horizontal well, near a bed boundary (from Gianzero et al., 1989)
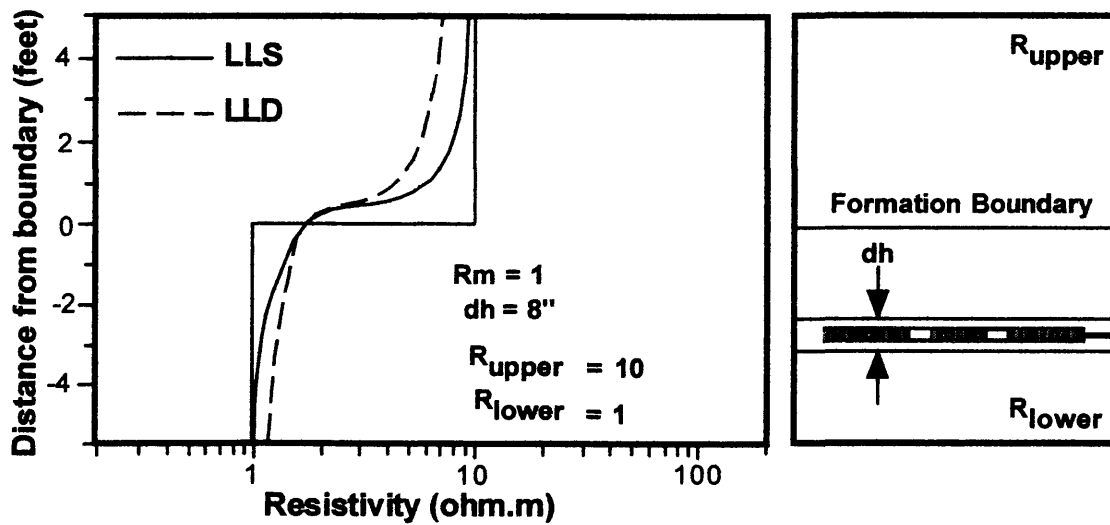
Figure 13 - Simulated response of a dual laterolog tool in a horizontal well, near a bed boundary (from Gianzero et al., 1989).

3

0

R Bit

R Lat

Rm = 1

R_{upper} = 10

R_{lower} = 1

Mandrel Dia. = 7"

dh = 9

R_{upper}

Formation Boundary

dh

R_{lower}

Distance from boundary (feet)
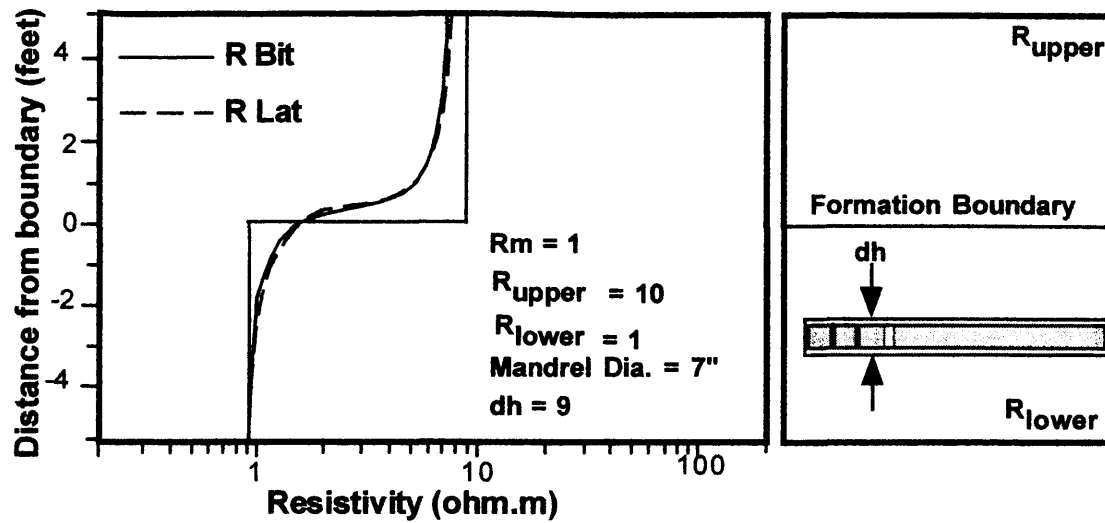
Resistivity (ohm.m)

Figure 14 - Modeled response of the LWD toroidal resistivity tool in a horizontal well, near a bed boundary (from Gianzero et al., 1989)

PSR

ATR

True Depth (inches)
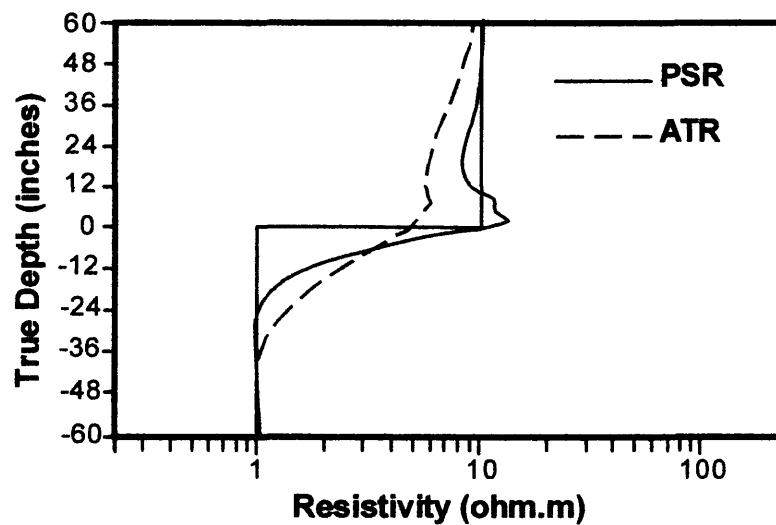
Resistivity (ohm.m)

Figure 15 - Modeled response of a LWD 2MHz resistivity tool in a horizontal well, near a bed boundary (from Anderson et al., 1990).

wells: a local and dramatic increase in apparent resistivity when the tool crosses the bed boundary. This physical phenomenon, called a polarization horn, is described in more detail in the following section.

2.2.2. Polarization Horns

Polarization horns are well-known resistivity features of induction tools in highly deviated and horizontal wells. They are characterized by an overshoot of the tool response directly at the bed boundary (**Figure 16**). Howard and Chew (1989) first explained the polarization horn effect. Further studies by Barber and Howard (1989) and Anderson et al. (1990) improved our understanding of this physical phenomenon.

Polarization horns are the result of charge build-up at bed boundaries, caused by a discontinuity of the electric field across the contact between beds of different resistivities. When a dipping bed boundary is encountered, the induced currents have to cross the boundary. The currents must be the same for a given current loop, but the electric field is different in the contrasting resistivity beds. As a consequence, the normal component of the electric field has a discontinuity across the boundary, which causes the charge build-up at the formation interface (Anderson et al., 1990). The polarization layer oscillates with the same frequency as the originating wave. This oscillating charge acts like a secondary transmitter. As the receivers move past the boundary, the received signal from the secondary transmitter suddenly increases, and the total received signal is distorted into a polarization horn (Anderson et al. 1990).
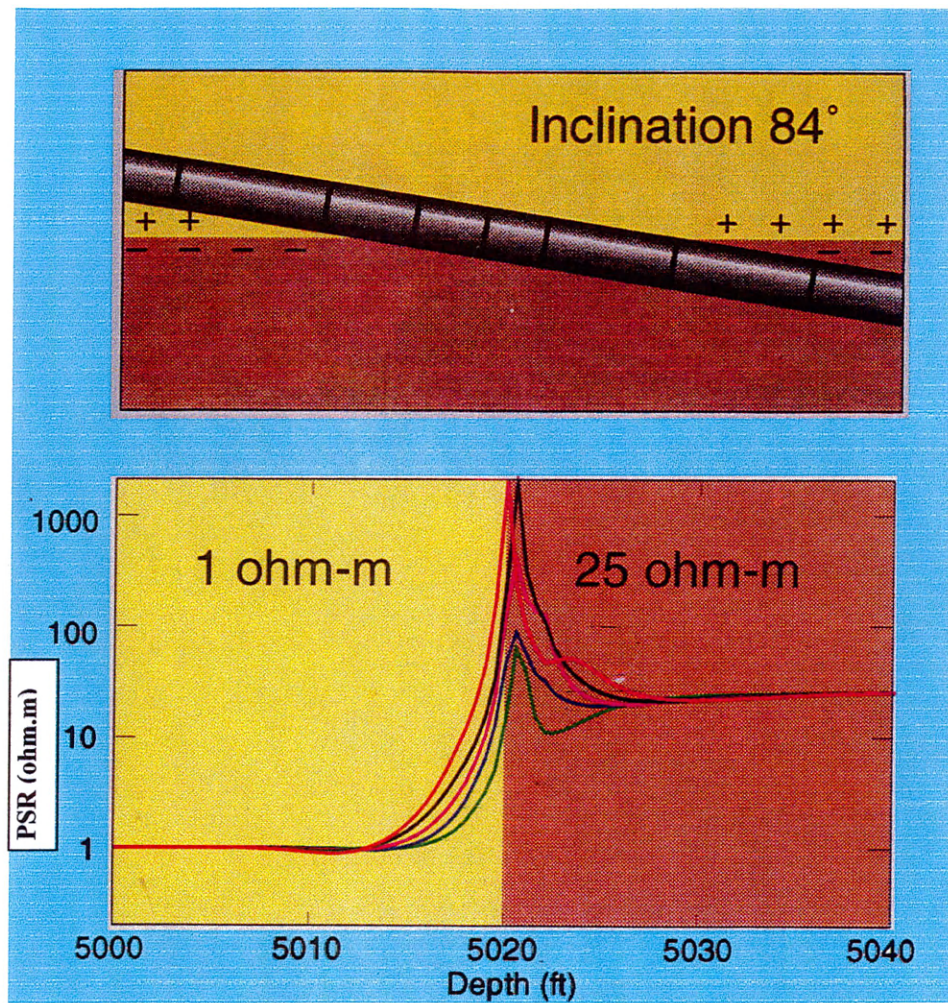
Figure 16 - Polarization horn developed with a LWD 2 MHz resistivity tool in a highly deviated well. The overshoot of tool response occurs on the resistive side of the bed boundary (from Schlumberger, 1997).

The magnitude of the polarization horns increases with the relative dip angle and the resistivity contrast, being more pronounced at low resistivity levels (Anderson et al., 1990). Theoretically, it is generally accepted that bed-boundary polarization charges start to develop at a relative dip angle of 50°, as long as at least one order of magnitude resistivity contrast exists between the two. Modeled horns are often larger than those seen on field logs. This can be explained because the assumed abrupt geological contrasts do not actually exist.

Although polarization horns do not reflect true resistivity variations, they are excellent bed boundary indicators for large resistivity contrasts encountered by highly deviated wells in relatively flat-lying beds. The absence of horns in horizontal wells crossing bed boundaries with large resistivity contrasts is a sign that the relative dip angle is less than 50°.

2.3 - Invasion Effects

Invasion effects on resistivity logs depend on the depth of investigation of the tool and the moment in time that the measurements are made (Peeters et al., 1999). Filtrate invasion in relatively high permeable formations (permeability greater than 10 md) is mainly controlled by mud and mudcake properties, not formation permeabilities (Allen et al., 1991; Woodhouse et al., 1991). Therefore, the diameter of invasion will vary inversely with porosity.

Besides mud and mudcake properties, a detailed understanding of the invasion profile is required for accurate log interpretation. Allen et al. (1991) provided a comprehensive study of the invasion processes and invasion zone geometry. The fluid loss can be classified in two distinct phases: spurt invasion and filtration invasion. The spurt invasion takes place as the drill bit exposes fresh rock. It is characterized by the whole mud flowing directly into the formation, before any mudcake is established. The filtration invasion phase begins after mudcake development and can occur under dynamic or static conditions. Dynamic filtration occurs while circulating or circulating and drilling. Static filtration occurs when there is no mud flow. Under static conditions the mudcake grows undisturbed, and filtrate loss rate decreases with time. Under dynamic conditions, the erosive actions of mud flow and drillstring prevent mudcake accretion. When mudcake deposition and erosion reach equilibrium, the dynamic invasion loss stays constant at the critical invasion rate. The differences between dynamic and static filtration are more evident in how the filtrate loss rate changes with time rather than in absolute loss rate magnitudes. However, since dynamic filtration normally acts over a much longer period than static filtration, most filtrate is lost under dynamic conditions (Allen et al., 1991; Woodhouse et al., 1991).

Laboratory experiments and field log examples (Peeters et al., 1999) demonstrate that after the initial spurt loss a steady invasion continues to develop until casing has been set (Fordham et al., 1988; Woodhouse et al., 1991). In hydrocarbon-bearing formations invaded by water-base mud, the invasion profile is better described by the two-front

model of invasion, which assumes the development of salinity and saturation fronts in the

reservoir (**Figure 17**). As the result of salinity equilibration by ion diffusion, invading

mud filtrate displaces formation water in front of it, which in turns displaces moveable

hydrocarbons. Two fluid banks are thus created behind the undisturbed reservoir: one

with water with mud filtrate salinity and the second with formation water salinity (Allen

et al., 1991; Peeters et al., 1999). This model is also known as the annulus invasion

profile, characterized by three radially distinct resistivity zones, including the annulus

resistivity and two invasion diameters (Allen et al., 1993). Recently, a prototype invasion

program was used to model LWD 2MHz resistivity curves in the ABH-2 horizontal well

of Albacora field (Peeters et al., 1999). The best fit between the measured and modeled
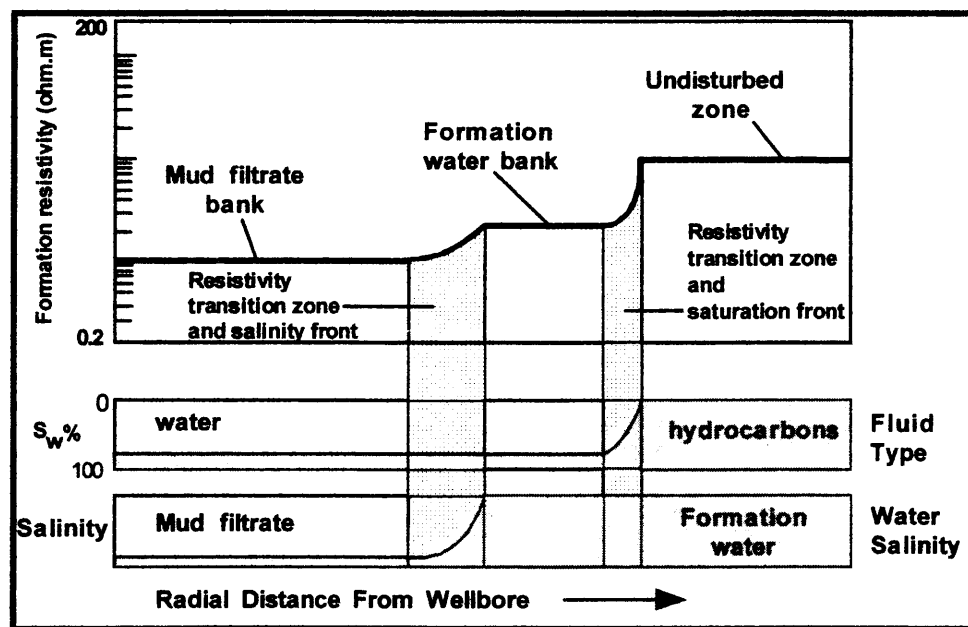
Figure 17 - Two-front model of fluid displacement during invasion (after Allen et al., 1991, in Peeters et al., 1999).

resistivity curves was only achieved when the simple stepwise invasion profile was changed to the more realistic two-front model of invasion.

Gravity also plays a role in the invasion profile. The fluid banks move up or down depending on the formation's vertical permeability and the density contrasts between mud filtrate and formation fluid (Allen et al., 1991; Woodhouse et al., 1991).

2.3.1 Invasion in Horizontal Wells

In horizontal wells the invasion pattern is quite different from vertical wells. In vertical holes the layered stratification is essentially normal to the wellbore and the effects of gravity remain symmetrical with respect to the axis of the borehole. In horizontal wells, however, the borehole is usually parallel to different bed boundaries, and gravity affects the borehole fluid and the invasion distribution in a highly non-symmetrical fashion (York et al., 1992).

Two different mechanisms control the asymmetrical invasion profile in horizontal wells. The first mechanism is related to the contrast between vertical and horizontal permeabilities commonly observed in sedimentary formations. Horizontally laminated formations tend to present a horizontal permeability (Kh) much larger than the vertical permeability (Kv), causing elliptical invasion geometry, the long axis being along the horizontal direction (York et al., 1992) **(Figure 18a)**. The second mechanism is gravitational segregation. The density contrast between mud filtrate and formation fluid can generate a pear-shaped invasion profile around the borehole when the vertical

permeability and the density contrast are large (**Figure 18b**). The orientation of the "pear" depends on density differences between the formation and invaded fluids.

Woodhouse et al. (1991) analyzed neutron log responses before and after invasion in gas-bearing horizontal wells, and proposed an invasion model where gravitational segregation caused the invasion front to move downward and away from the borehole (**Figure 19**). The contrast of vertical and horizontal permeabilities was found to affect filtrate mobility and segregation only when Kv/Kh ratio is greater than 0.01. The presence of reservoir heterogeneities like shale barriers, faults or cemented layers can distort the shape of the mud filtrate body.

2.3.2 Time-lapse logs

The rapid and continuous growth of LWD technology has provided a new and essential evaluation tool for the study of filtrate invasion: time-lapse logging. The time-lapse technique relies on the fact that LWD sensors make measurements shortly after the formation has been drilled, prior to significant mud filtrate invasion. Subsequent measurements after drilling (MAD), during bit trips for instance, will record changes in the formation properties through time, as a function of filtrate invasion. The rate, duration and magnitude of these changes permit the interpreter to hypothesize about the invasion processes, the invaded body geometries, and the associated reservoir properties (Chin et al., 1986; Cunninghan et al., 1990; Peeters et al., 1999).
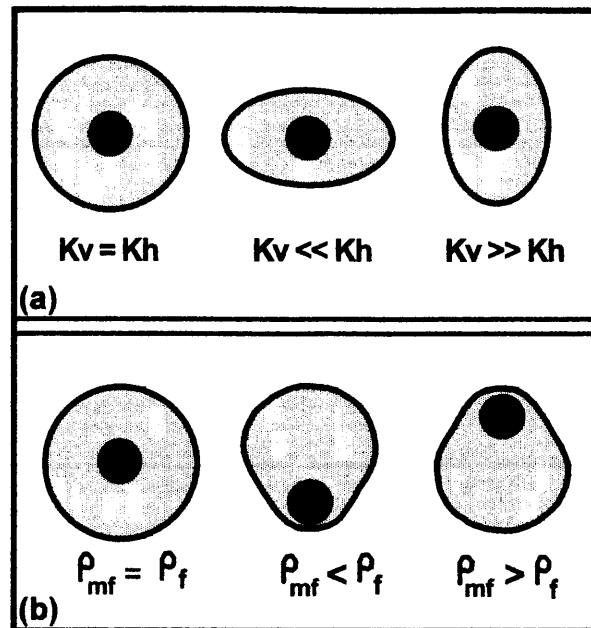
Figure 18 - Mechanisms controlling the invasion profile in horizontal wells. (a) Permeability anisotropy. (b) Gravitational segregation - differences in density between mud filtrate(ρ_{mf}) and formation fluids (ρ_f) result in a "pear-shaped" invasion profile (modified from York et al., 1992).
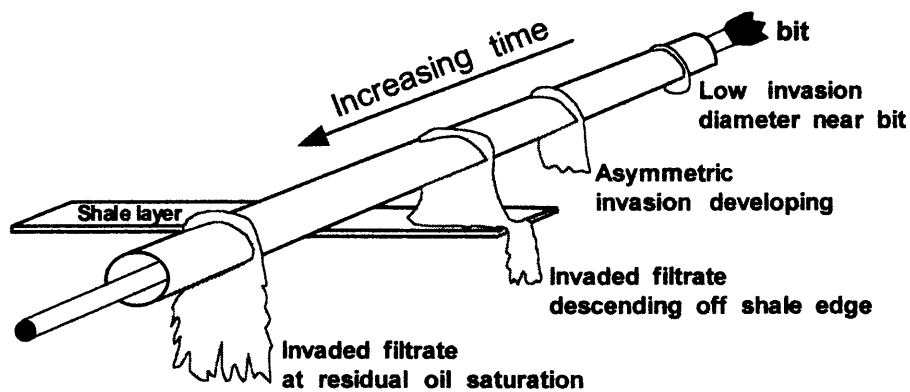
Figure 19 - Conceptual invasion model in a horizontal well as a function of time proposed by Woodhouse et al. (1991).

LWD resistivity sensors can be placed in the borehole assembly (BHA) directly behind the bit for navigation purposes in horizontal wells. They may also be placed 10-20 meters behind the bit, when combined with other LWD sensors. Depending on the bit-sensor distance and the rate-of-penetration (ROP), the time delay between drilling and making the measurement can be sufficient for significant mud filtrate invasion. In this case, the LWD measurements will not provide the formation resistivity (Rt). Subsequent MAD passes will show the evolution of the invasion profile with increasing formation exposure time.

2.4 - Resistivity Modeling

The various environmental effects disturbing resistivity tool response in horizontal wells can be present together. This can make the task of properly analyzing any of them to extract actual formation resistivity (Rt) a very complex problem. Beside the already discussed effects, borehole characteristics and high formation dielectric values can add new variables to the interpretation problem (Meyer et al., 1996).

The best solution to handle this combined influence of environmental effects in horizontal wells is by using resistivity modeling programs. This technique has had a great improvement in the last ten years. Today, sophisticated computer programs are available to simulate the response of resistivity sensors to a variety of environments and formation conditions (Anderson et al., 1990, 1997; Allen et al., 1993). Log simulation is particularly

important in interpretation of horizontal well logs, where conventional interpretation methods are not adequate.

Resistivity modeling inputs include the well trajectory, the geological model, and the electrical properties of the layers. A computed log can be generated and compared to the measured log and adjustments in the parameters can be made to obtain a match that will confirm the input geological model and formation properties. However, resistivity modeling does not generate a unique solution. Because there are many more unknowns than measurements, more than one set of formation parameters can match the acquired logs. Additional data of the studied area including cores, more logs (multi-depth investigation and time-lapse passes) and petrophysical analysis are necessary to solve the ambiguities and define the more reliable model.

CHAPTER 3.

GEOLOGIC SETTING

3.1 - Albacora Field, Campos Basin

Albacora field is one of the giant oil fields of the eastern Brazilian marginal basins. The field is located in the Campos basin, the main petroleum province of Brazil, which holds approximately 80% of Brazil's oil reserves. The Campos basin covers an area of about 100,000 km^2 along the southeastern Brazilian passive margin and extends roughly from 15 km inland to the 3400 m isobath. It is separated from southwestern and northeastern adjacent basins by the Cabo Frio and Vitoria basement highs, respectively (Guardado et al., 1989; Candido and Cora, 1991) (**Figure 1**).

Albacora field was discovered in 1984, under water depths ranging from 250 to 2000 m and incorporates an area of 235 km^2. The field is composed of several vertically stacked accumulations of sandstone turbidites, ranging in age from Albian to Miocene (Candido and Cora, 1991). The whole field contains volumes of oil in place reaching 2.26 billion bbl of crude from 18 to 30° API (Candido and Cora, 1991).

Upper Jurassic to Recent sediments of the eastern Brazilian marginal basins can be subdivided into six megasequences, which are linked to the continental breakup of Gondwanaland and the evolution of the Atlantic Ocean (Bruhn, 1998): 1- Continental

pre-rift megasequence (Upper Jurassic to Lower Neocomian); 2- Continental rift megasequence (Lower Neocomian to Lower Aptian); 3- Transitional evaporitic megasequence (Middle Aptian to Lower Albian); 4- Shallow carbonate platform megasequence (Lower to Middle Albian); 5- Marine transgressive megasequence (Upper Albian to lower Tertiary); 6- Marine regressive megasequence (Lower Tertiary to Recent). The chronostratigraphy of the Campos basin, outlining its main megasequences, is shown in **Figure 20**.

3.2 - The Namorado Reservoir

The Upper Albian Namorado reservoir accounts for 460 million bbl of original oil-in-place, and ultimate recoverable reserves of 85 million bbl, corresponding to 20% of the Albacora field. The oil acumulation covers an area of 40 km^2, between present water depths of 250 and 400 m (Bruhn et al., 1998). The turbidite reservoir is included in the marine transgressive megasequence which, in the Campos basin, spans from Upper Albian to Early Eocene. A generalized geological section for the eastern Brazilian marginal basins, highlighting the stratigraphic position of the Namorado reservoir in the Albacora field is shown in **Figure 21**.

The marine transgressive megasequence is characterized in the Brazilian continental margin by progressive coastal onlaps representing an overall deepening of water in the basin, following the generalized tendency of sea level rise in the Upper
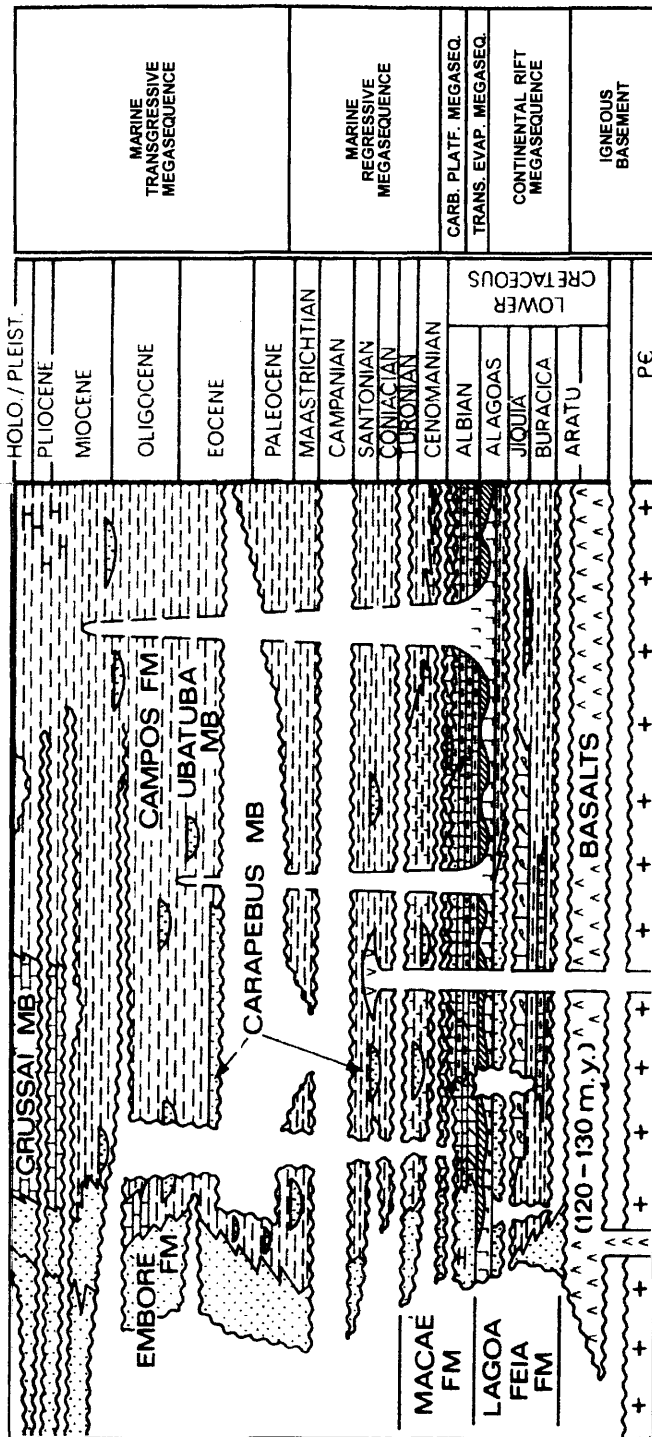
Figure 20 - Chronostratigraphy of the Campos basin (modified from Guardado et al., 1989).
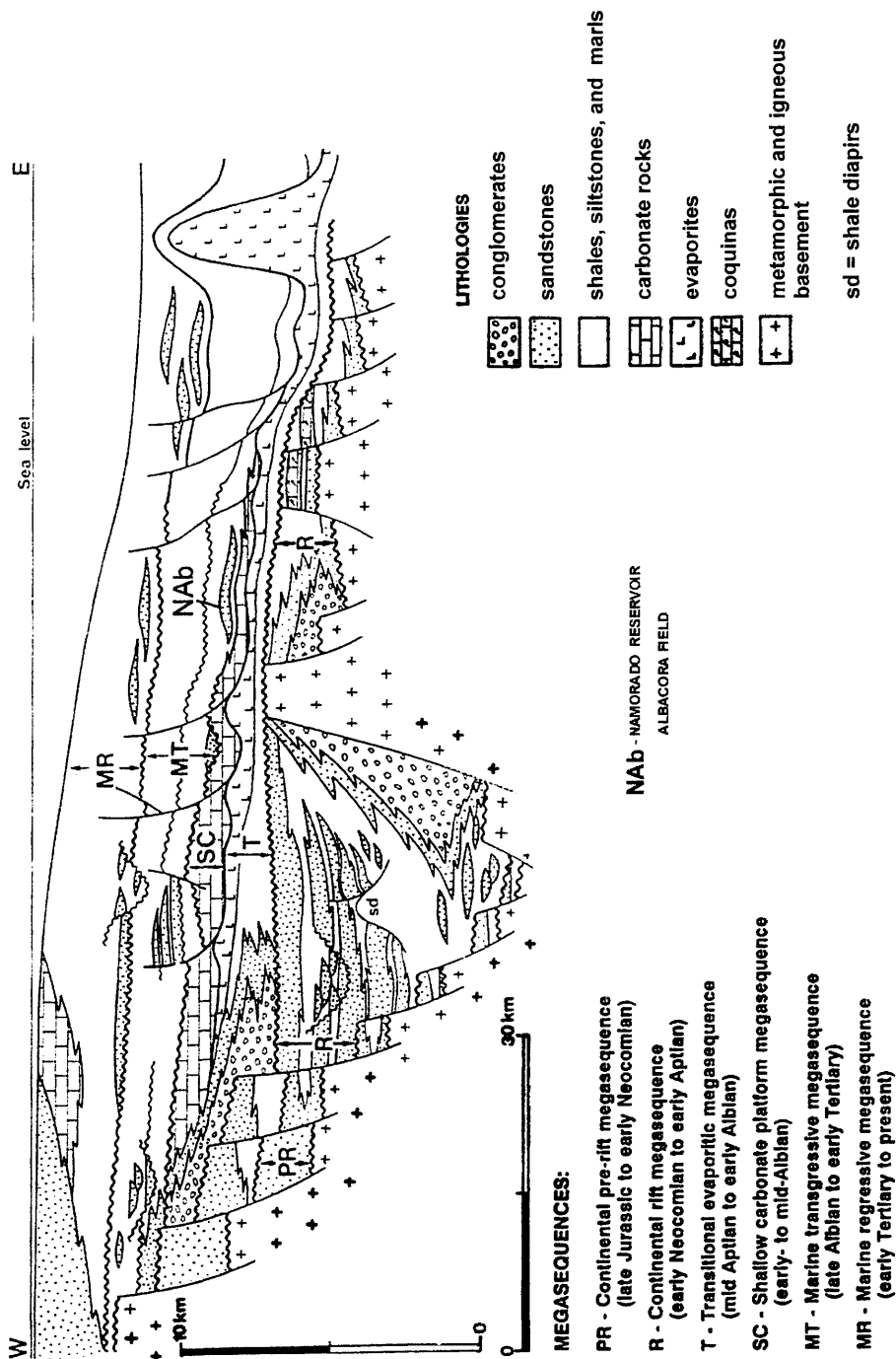
Figure 21 - Generalized geological section for the eastern Brazilian marginal basins (after Bruhn et al., 1995)

Cretaceous and Lower Tertiary (Chang et al., 1988; Guardado et al., 1989; Bruhn et al. 1998). Sedimentation started with deposition of calcilutites and marls. Then, the increasing rise in sea level and larger siliciclastic supply suppressed carbonate sedimentation and the transgressive megasequence became an essentially siliciclastic, muddy succession (Bruhn, 1998). In this scenario, sand-rich turbidites were deposited during falls of relative sea level, which could be related to relatively abrupt increases in the volume of sediment supply by episodic tectonic reactivation and or paleoclimatic variations in the source area and basin margins (Bruhn and Walker, 1995). The basal unconformity of the Upper Albian turbidite reservoir of Albacora field can be correlated with the Haq et al. (1988) eustatic sea level fall of 98 MA (Bruhn, 1998).

Paleoecological studies conducted by Dias-Brito (1982) and Koutsoukos and Dias-Brito (1987) inferred an outer neritic to upper bathyal setting (200-300m) for the Albacora area during Albian time.

Two fault systems are present in Albacora field, one affecting only the Cretaceous interval and the other influencing both the Cretaceous and Tertiary layers (Figure 21). Both fault systems resulted from salt collapse (Candido and Corá, 1991) and originated in paleolows where the Namorado turbidites were channeled (Arienti et al., 1995). The oil accumulation resulted from trapping in two anticlines oriented in the southwest-northeast direction, occurring throughout the Cretaceous and Tertiary strata (Candido and Corá, 1991). The Namorado reservoir is also affected by a series of approximately N-S normal faults with throws of up to 300 m. Some of these faults contribute to the definition of the

accumulation boundaries, but are not considered to be restrictive to the flow of fluids (Candido and Corá, 1991) (**Figure 2**).

The main source rocks are Late Barremian to Early Aptian lacustrine shales of the Lagoa Feia formation (Figueiredo and Mohriak, 1984), separated from the major reservoirs by a thick evaporitic section (**Figure 21**). The pathway for oil migration up to the field's accumulation were given by the fault systems already mentioned (Candido and Corá, 1991). The reservoir seals are hemipelagic marls and shales.

3.2.1 - Sedimentary Facies and Depositional Environment

Four major sedimentary facies have been distinguished in the Namorado sandstone, based mainly on texture and sedimentary structures (Bruhn, 1995): Facies 1- Massive Sandstone; Facies 2- Sandstones with Bouma sequence; Facies 3- Calcilutites, Marls and Shales; and Facies 4- Diamictites.

The massive sandstones are characterized by poorly sorted, very fine/fine-grained sandstones and subordinately by medium-grained sandstones (**Figure 22**). This facies may also exhibit subtle normal graded bedding, with coarse and medium grains at the base and fine or very fine grains at the top (Bruhn et al., 1995; Arienti et al., 1995). Composition is mainly of quartz, feldspars, and fragments of quartzofeldspathic high-grade metamorphic rocks. Mud matrix includes 3-30% silt and 1-6% clay. Fluid escape structures, mainly dish and pillar structures, occur locally (Bruhn, 1998). Individual beds have average thicknesses of 1 m, but amalgamated units may reach up to 20 m.
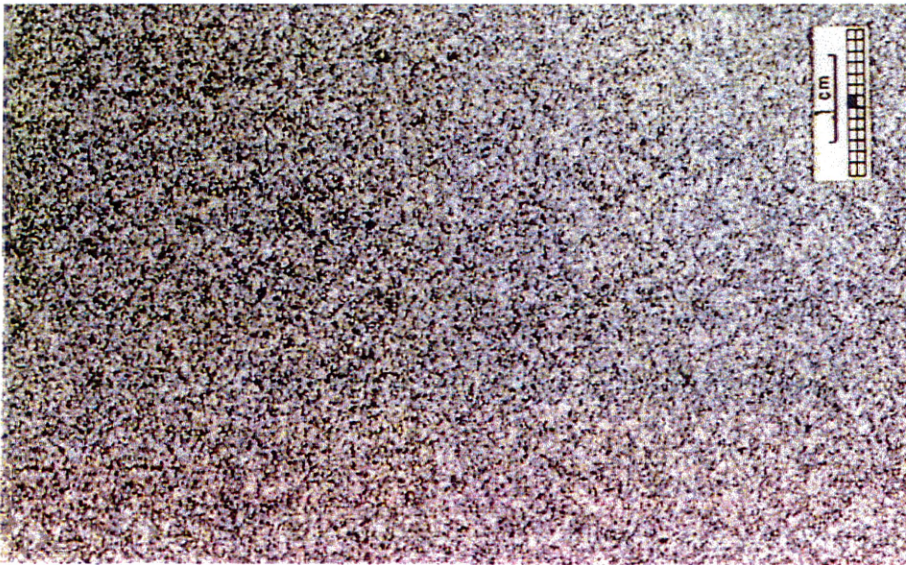
(A)
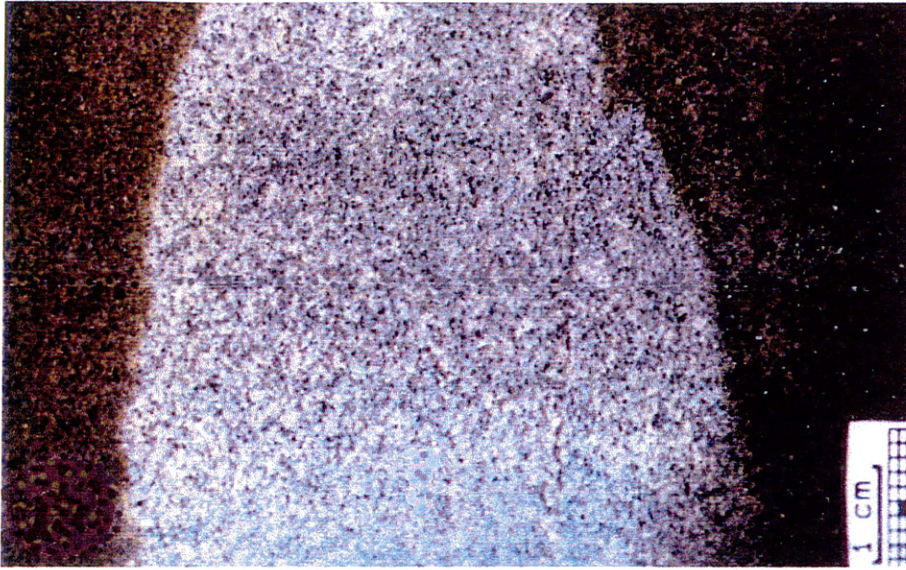
(B)

Figure 22 - Massive sandstone (A) with levels completely cemented by calcite (B). Core photos from vertical wells in the Namorado reservoir (from Bruhn, 1995).

Bioclastic-rich levels are common at the base and/or at the top of the turbidite cycles and represent heterogeneities in the reservoir that control the occurrence of levels completely cemented by calcite (Bruhn et al., 1995, Bruhn et al., 1998; Arienti et al., 1995) (**Figure 22**).

The massive sandstones are by far the main reservoir facies of the Namorado turbidites with up to 87% of the cored section in the well ABV-2 (Bruhn et al., 1995). The depositional mechanism was interpreted as the result of rapid deposition by high-density turbidity currents (Lowe, 1992; Bruhn et al., 1995; Arienti et al., 1995).

The sandstones with Bouma sequences are characterized by very fine/fine-grained sandstones with parallel laminations and climbing ripples (**Figure 23**). They contain amalgamated Bouma divisions Tab, Tabc,Tbc or Tc (Bruhn et al., 1995; Bruhn et al., 1998). Composition is the same as the massive sandstones, with beds ranging in thickness from 10 to 30 cm. Levels completely cemented by calcite are also present. This facies accounts for only 3% of the cored section in the well ABV-2 (Bruhn et al., 1995). The depositional mechanism was interpreted to be the result of low-density turbidity currents (Lowe, 1982; Bruhn et al., 1995; Arienti et al., 1995) with the development of structures from traction sedimentation.

The Calcilutite, Shale and Marl Facies is represented by an association of these three lithologies, with great continuity in the Albacora field (Arienti et al., 1995) (**Figure 23**). The calcilutites and marls show pervasive bioturbation. Individual lithologic beds are thinner than 1 m, but the total pelitic interval can reach 4 m (Bruhn et al., 1995; Arienti et
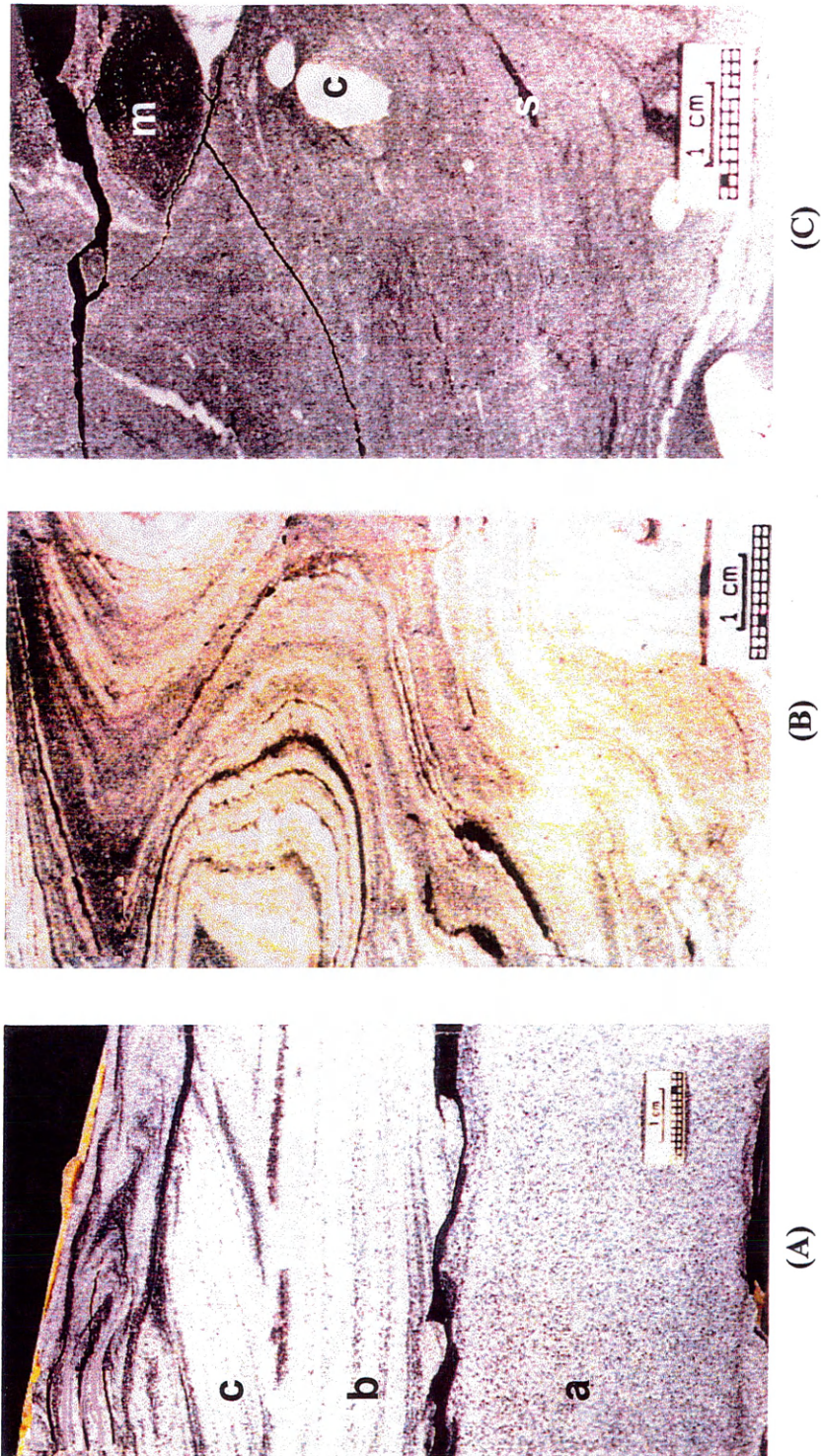
Figure 23 - **(A)**: sandstone with Bouma sequence Tabc; **(B)**: calcilutites and marls deformed by slumping; **(C)**: diamictite with calcilutite (c), shale (s) and marl (m) clasts. Core photos from vertical wells in the Namorado reservoir (from Bruhn, 1995).

al., 1995). Marls and calcilutites are commonly deformed by slumping. Shales are dark, laminated and bioturbated.

The pelitic facies represents 4% of the cored section in the well ABV-2 (Bruhn et al., 1995). This facies is representative of background sedimentation in an outer neritic to upper bathyal environment (Bruhn et al., 1998).

The diamictites are represented by granule- to cobble-sized mud and/or carbonate intraclasts dispersed in a matrix with variable content of mud and sand (Bruhn et al., 1995) (**Figure 23**). Diamictite beds range from 3 to 12 m thick (Arienti et al., 1995). Bruhn et al. (1995) and Arienti et al. (1995) interpreted the diamictite facies to be the result of slumping and debris-flow processes.

The Upper Albian turbidite sandstones of the Albacora field were interpreted by Bruhn (1998) as lobes deposited in broad intra-slope depressions. In this model, channel-levee complexes of the inner-fan environment grade to thick, massive sandstone-dominated sheet sands or lobes in the mid-fan environment (Moraes, 1989). Amalgamation of shallow and ephemeral channels in a low gradient can result in associations up to 50 m thick and with areal distribution greater than 10 km^2.

3.2.2 Stratigraphy

The Namorado turbidite reservoirs of Albacora field are confined to a NW-SE-oriented, 100 km-long and 40 km-wide sag (Martins et al., 1990; Bruhn et al., 1998) (**Figure 24**). This intra-slope depression where the turbidites were channeled is related to
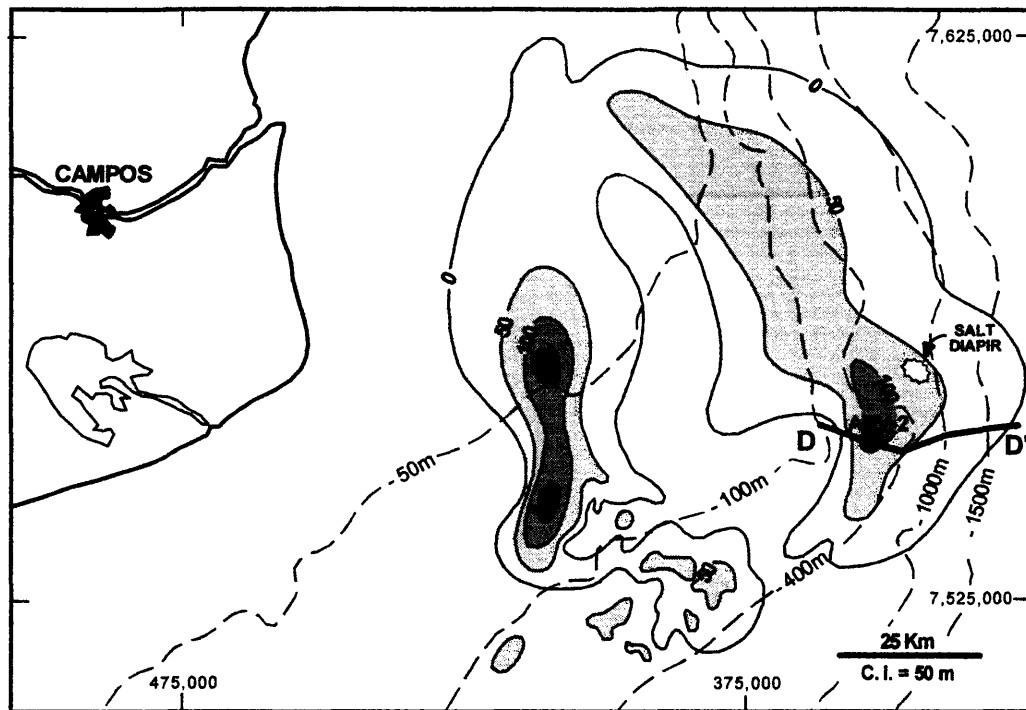
Figure 24 - Net sand map for the Upper Albian turbidites of Campos basin (after
Martins et al., 1990 in Bruhn et al., 1998). Well ABV-2 indicates
approximate location of Albacora field.

the eastward tilting of the Campos basin, with resulting downslope gliding of underlying Aptian evaporites (Bruhn et al., 1998) (**Figure 25**).

According to Bruhn et al. (1995) and Bruhn et al. (1998), the Namorado reservoir can be subdivided, from top to base, into two main sand-rich turbidite successions. The uppermost (Namorado I) is 0-12 m thick, and the lowermost (Namorado II) is 28-107 m thick. An 11-17 m thick succession of diamictites and bioturbated calcilutites, marls and shales separates these main stratigraphic units. Based on petrophysical properties from cores and well logs and the presence of thicker, widespread non-reservoir beds, the two stratigraphic successions were subdivided into 12 reservoir units, named 1 to 12, from oldest to youngest. Units 1 to 10 correspond to the Namorado II interval and units 11 and 12 to the Namorado I interval. The reservoir units comprise N-S to NW-SE oriented, 2-20 m thick, 6->20 km-wide lobate sand bodies. Correlation between the reservoir units in the studied area can be seen in the structural cross-section in **Figures 26**.

3.2.3 Reservoir Quality Controls

Diagenetic and depositional processes control porosity and permeability in the Namorado reservoir of Albacora field. Diagenesis, in the form of calcite cementation is the dominant factor controlling reservoir quality (Souza and Silva, 1998; Bruhn et al., 1998).

Additional reservoir quality controls are given by textural properties such as grain size, sorting and silt content. Coarser-grained sandstones are typically more poorly sorted
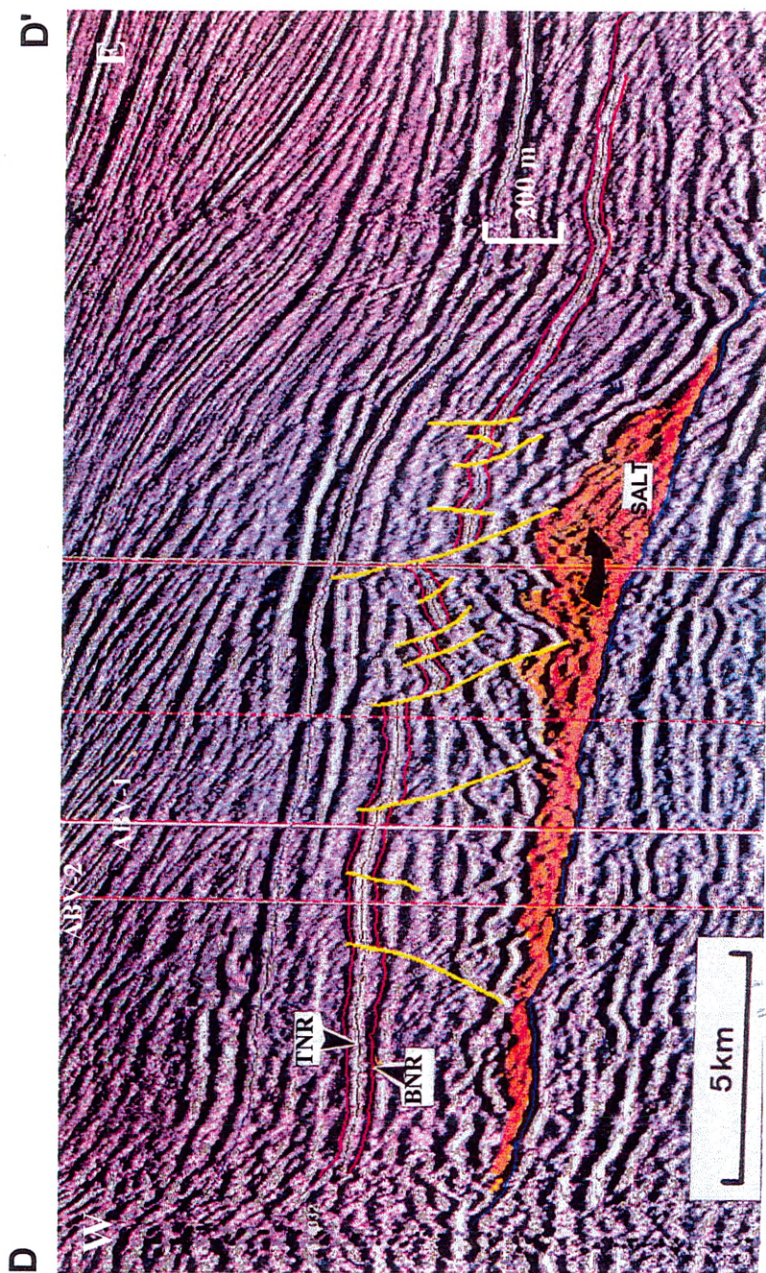
Figure 25 - Dip seismic profile for the Albacora field, located in Figure 24 (**D - D'**). **TNR** and **BNR** are the top and base of the Namorado reservoir. Turbidites are structured by N-oriented normal faults related to gravitational gliding of Aptian salt, indicated by arrow (after Bruhn et al., 1998).
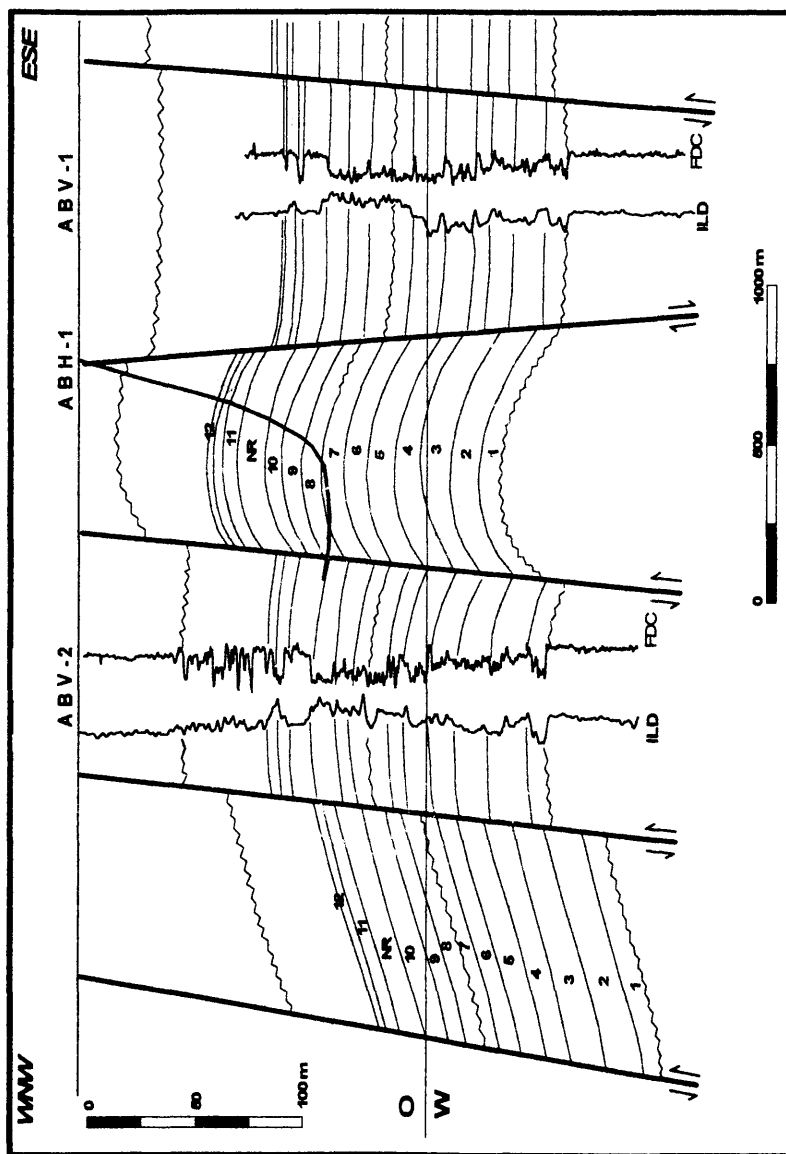
Figure 26 - Structural cross-section of Upper Albian turbidite reservoirs of Albacora field, showing correlation between reservoir units (1 - 12) crossed by wells ABV-1, ABV-2 and ABH-1. The density logs (FDC) show decreasing porosity values below the oil-water contact, revealing reduced reservoir quality in the water zone. Non-sealing normal faults allow pressure communication between the different reservoir units. Cross section in the same orientation as **Figure 25** (after Bruhn et al., 1998).

and tightly packed, and present lower porosity (Bruhn et al., 1998). Souza et al. (1995) recognized five distinct reservoir pore systems in the massive sandstone facies, where pore geometries create significant permeability variations in the reservoir. Besides calcite cementation, partial dissolution of framework grains and mechanical compaction were also found to be important diagenetic modifiers of the pore system in this reservoir.

The log-linear relationship between porosity and permeability measurements on core plugs from well ABV-2 is shown in **Figure 27**. Porosity and permeability ranges are 2-32% and 0.1-1620 md, respectively, with a main cluster of values from 20 to 25% porosity and 10 to 300 md permeability. The lower porosity and permeability values,
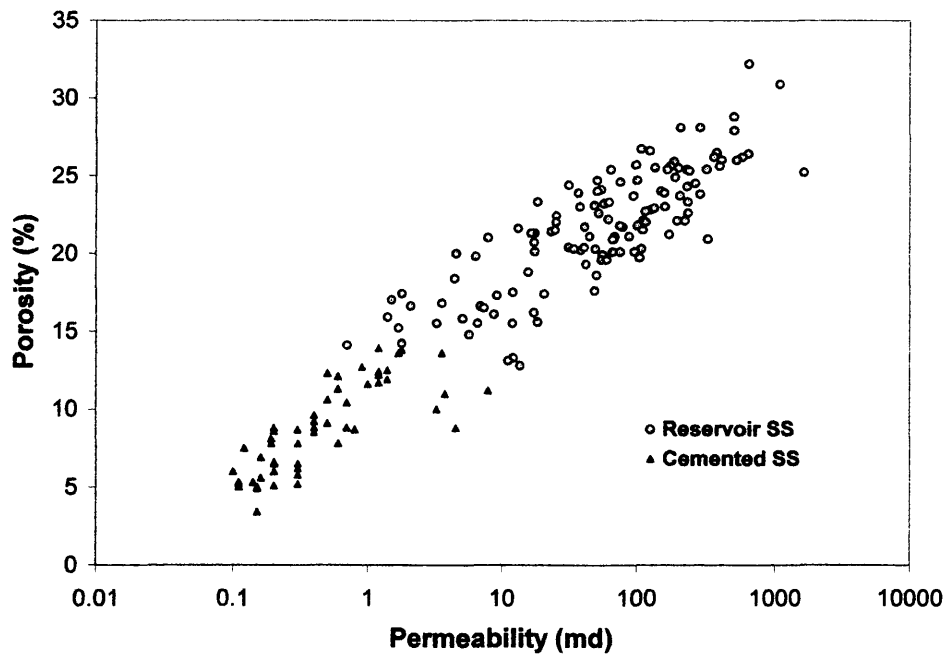
Figure 27 - Porosity vs permeability crossplot from core plugs of well ABV-2. Lower values of k and ϕ correspond to calcite-cemented sandstones.

below 14% and 10 md, are represented by calcite-cemented sandstones. The petrophysical properties improve with decreasing calcite-cement content, highlighting the first-order diagenetic control on reservoir quality in these rocks.

3.2.4 Internal Reservoir Heterogeneity

The variable distribution of non-reservoir, calcite-cemented sandstone bodies constitutes the main reservoir heterogeneity in the Upper Albian turbidites of Albacora field. The cemented zones range in thickness from 5 cm to 1 m, with an average thickness of 30 cm, characterizing 15 to 30% of the gross thickness of the turbidite reservoir (Carvalho et al., 1995; Sombra et al., 1995). The proximity of the turbidite deposits with the underlying Albian-Turonian carbonate rocks, in a faulted system (**Figure 21**), provided the ideal conditions for upward fluid movement and calcite precipitation within the reservoir (Souza and Silva, 1998). The cemented zones are chiefly formed by cement nucleation on bioclastic-enriched levels (Sombra et al., 1995). Thicker and more frequent examples of calcite-cemented beds occur below the oil-water contact because oil emplacement inhibited both calcite cementation and mechanical compaction within the reservoir. This resulted in higher porosity and permeability in the oil zone than in the water zone (Souza and Silva, 1998) (**Figure 26**).

Distribution patterns of calcite cement in sandstones have been studied by many authors for various depositional environments. Slatt and Hopkins (1990) mapped calcite-cemented zones in a North Sea turbidite field and observed lateral discontinuity along

individual stratigraphic horizons. Walderhaug and Bjorkum (1998), studying shallow marine sandstone outcrops, concluded that the most important calcite- cement geometries in these deposits are represented by continuously cemented layers, layers with stratabound concretions (**Figure 28**), scattered concretions and patchy or microconcretionary calcite cement. McBride et al. (1995) studied spatial patterns of calcite concretions in shallow and deep marine deposits. Concretion shapes were found to include spheres, oblate and prolate spheroids, tabular forms and irregular forms.

In the Namorado reservoir of Albacora field, calcite-cemented zones are chiefly formed by cement nucleation on bioclastic-enriched levels, resulting in concretions that include spherical, tabular and irregular geometries (Carvalho et al., 1995; Sombra et al., 1995; Souza and Silva, 1998). The presence of cemented sandstone bodies represents a major problem in the development of the Namorado reservoir because the cemented zones interfere with fluid flow, creating high complexity and heterogeneity within originally massive and homogeneus sandstones (Carvalho et al., 1995). The lateral continuity of these internal reservoir heterogeneities and their effectiveness as permeability barriers in the turbidite reservoirs of Albacora field is the target of current studies (Barroso et al., 1997).
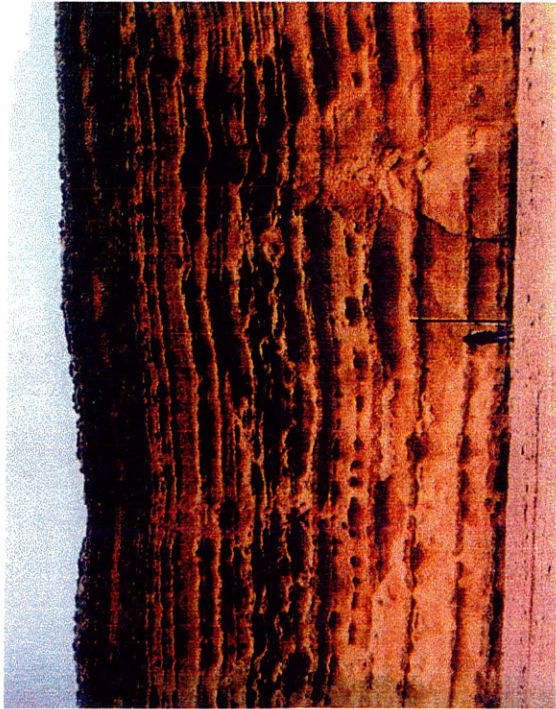
(A)
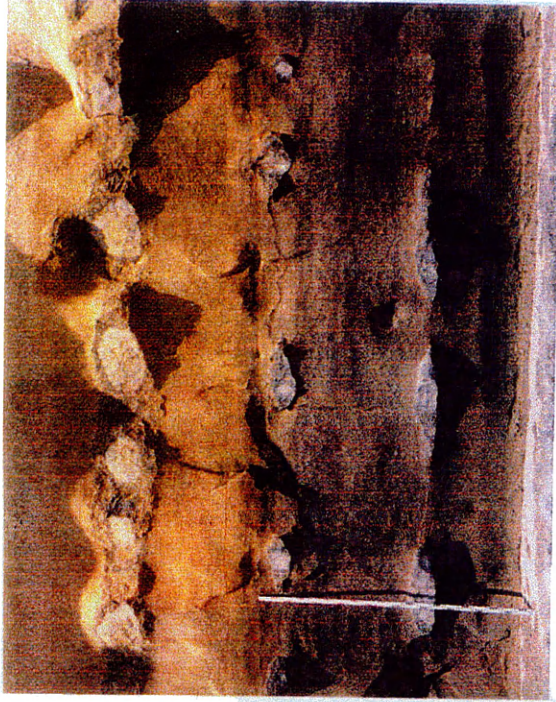
(B)

Figure 28 - Examples of calcite-cement geometries from shallow marine sandstone outcrop in the Lower Jurassic Bridport Sands, southern England (from Walderhaug and Bjorkum, 1998). (A): laterally extensive continuously calcite-cemented layers and layers of stratabound calcite-cemented concretions. Scale is 4 m long; (B): close-up view of two stratabound flattened concretions below a continuously calcite-cemented layer where an early concretionary growth stage can be seen by its lighter weathering color. Scale is 2 m long.

CHAPTER 4.

RESERVOIR CHARACTERIZATION

Extensive studies on the stratigraphy, sedimentology and diagenesis of the Upper Albian turbidite sandstones of Albacora field have resulted in a comprehensive reservoir description, based on a large data set (Abreu et al., 1992; Arienti et al., 1995; Souza et al., 1995; Sombra et al., 1995; Bruhn et al., 1995; 1998; Bruhn, 1998; Barroso et al., 1997; Souza and Silva, 1998). In this work I integrated data from cores, well logs and petrophysical analysis from three vertical wells (ABV-1 to 3) and two horizontal wells (ABH-1 and ABH-2) in the Albacora field (**Figure 2**). The main objective was the identification of reservoir heterogeneities to study their effects on resistivity log responses along the horizontal boreholes.

The presence of an oil/water contact (**Figure 26**) restricts the pay interval mostly to the upper six reservoir units (7 to 12). The detailed log correlation and reservoir description in this study was mainly focused on units 7 to 10, the target zones for horizontal wells in the Albacora field.

4.1 - Geologic Correlation

In order to obtain the reservoir geometry along the trajectory of the two horizontal wells, the upper reservoir units were correlated using well logs, core descriptions and a structural map based on 3D seismic (**Figure 2**, **Table 1**). The STRATLOG software package from Geoquest-Schlumberger was used to display the borehole profiles (vertical and horizontal) along with well logs, and to generate the geologic correlations between wells (**Figures 29** and **30**). Tops and bottoms of five reservoir units (7 to 11) and main non-reservoir intervals were picked on well logs in the three vertical and two horizontal wells (**Table 4**). The Z&S software from Baker Hughes was used to compute true vertical depth (tvd) logs for the two distinct deviated sections of the horizontal wells (less and greater than 90 degrees). Correlation between each pair of tvd plots in the horizontal wells (**Figures 31** and **32**) added to a more precise definition of reservoir unit boundaries in the repeated sections along the horizontal well trajectories.

The reservoir geometry along the path of the ABH-1 horizontal well is shown on the geologic section of **Figure 29**. Because the borehole traverses an anticlinal feature with increasing dip angles (66 to 91 degrees) after the lower stratigraphic position is reached at the base of reservoir unit 7, the well climbs stratigraphically, penetrating again units 7 and 8. A normal fault is crossed at the end of the horizontal trajectory, where the well leaves the reservoir, penetrating again an upper non-reservoir succession.

The reservoir geometry along the path of the ABH-2 horizontal well is shown on the geologic section of **Figure 30**. The upper reservoir units, with regional dip from 1 to
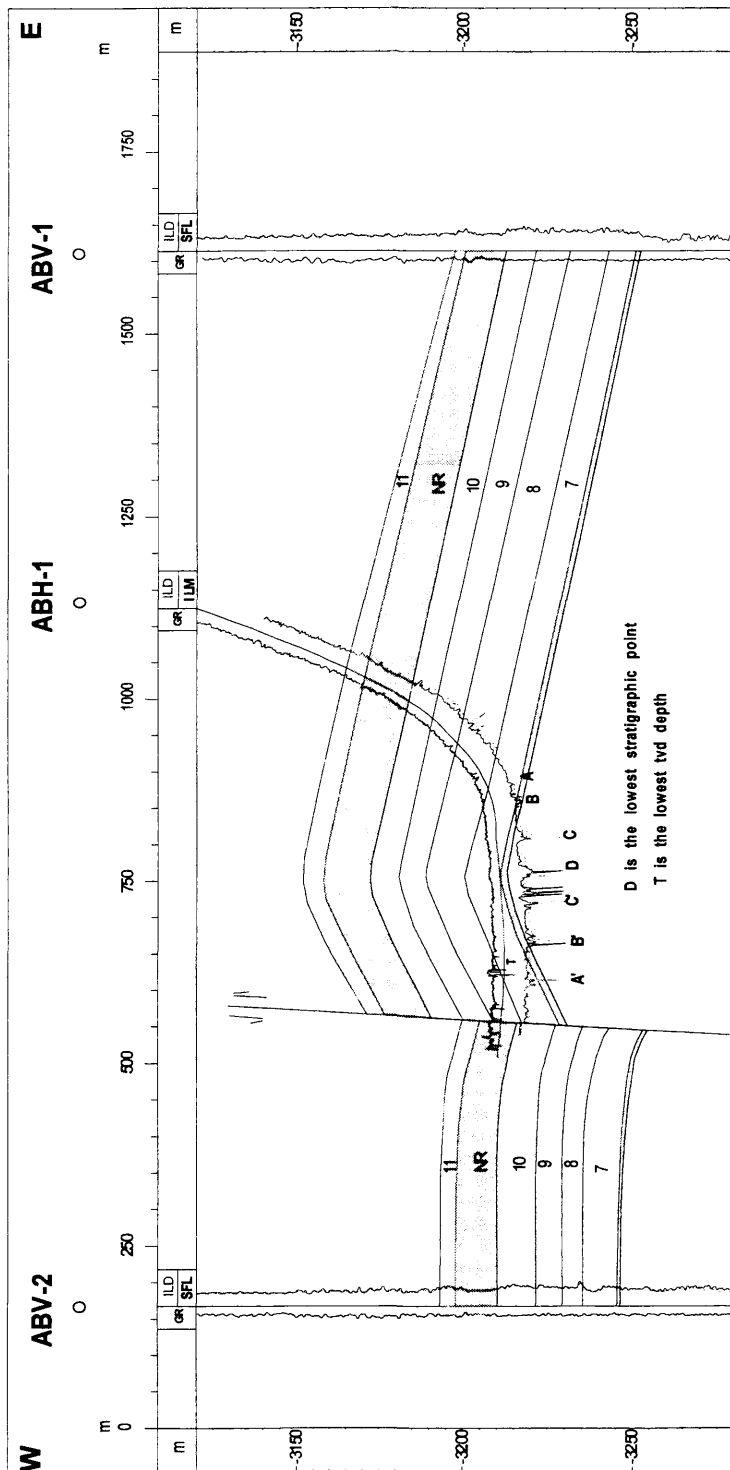
Figure 29 - Geologic section along the path of ABH-1 horizontal well. Induction (ILD and ILM) and gamma ray are displayed along the horizontal trajectory. Offsetting vertical wells are displayed with ILD, SFL and gamma ray curves. NR = non-reservoir. Numbers 7 through 11 are reservoir units.
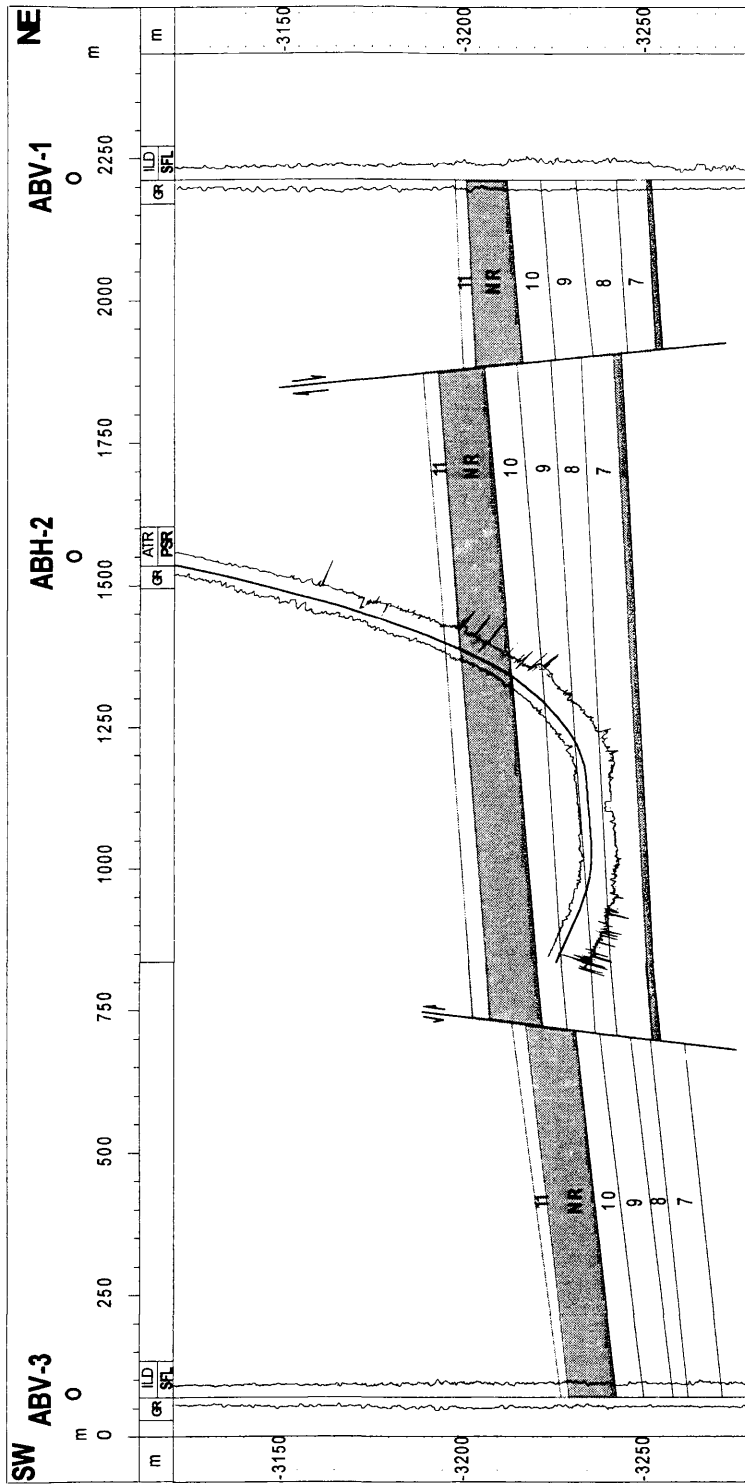
Figure 30 - Geologic section along the path of ABH-2 horizontal well. Logging while drilling (LWD) measurements (ATR and PSR curves) and gamma ray are displayed along the horizontal trajectory. Offsetting vertical wells are displayed with ILD, SFL and gamma ray curves. NR = non-reservoir. Numbers 7 through 11 are reservoir units.

Table 4 - Tops and bottoms of upper reservoir units and main non-reservoir (NR) intervals.

Reservoir units and non-reservoir intervals		ABV-1 (KB= 25 m)		ABV-2 (KB= 25 m)		ABV-3 (KB= 28 m)		ABH-1 (KB= 25 m)		ABH-2 (KB= 26 m)	
		Measured Depth (m)	Elev. (m)	Measured Depth (m)	Elev. (m)	Measured Depth (m)	Elev. (m)	Measured Depth (m)	Elev. (m)	Measured Depth (m)	Elev. (m)
11	Top	3223.5	-3198.5	3215.5	-3190.5	3251.0	-3223.0	3374.8	-3168.1	3521.0	-3195.0
11	Bottom	3226.5	-3201.5	3220.2	-3195.2	3253.5	-3225.5	3390.1	-3174.1	3534.0	-3198.5
NR	Top	3226.5	-3201.5	3220.2	-3195.2	3253.5	-3225.5	3390.1	-3174.1	3534.0	-3198.5
NR	Bottom	3238.0	-3213.0	3232.5	-3207.5	3266.5	-3238.5	3425.0	-3187.4	3589.5	-3215.5
10	Top	3238.0	-3213.0	3232.5	-3207.5	3266.5	-3238.5	3425.0	-3187.4	3589.5	-3215.5
10	Bottom	3247.0	-3222.0	3244.0	-3219.0	3274.0	-3246.0	3450.0	-3194.6	3637.0 4074.0*	-3223.5 -3227.5*
9	Top	3247.0	-3222.0	3244.0	-3219.0	3274.0	-3246.0	3450.0	-3194.6	3637.0 4074.0*	-3223.5 -3227.5*
9	Bottom	3256.9	-3231.9	3251.7	-3226.7	3282.0	-3254.0	3484.5	-3201.8	3707.0 3957.0*	-3232.2 -3235.1*
8	Top	3256.9	-3231.9	3251.7	-3226.7	3282.0	-3254.0	3484.5	-3201.8	3707.0 3957.0*	-3232.2 -3235.1*
8	Bottom	3268.2	-3243.2	3257.5	-3232.5	3286.0	-3258.0	3548.5 3818.0*	-3210.6 -3215.4*	------	------
7	Top	3268.2	-3243.2	3257.5	-3232.5	3286.0	-3258.0	3548.5 3818.0*	-3210.6 -3215.4*	------	------
7	Bottom	3276.5	-3251.5	3267.5	-3242.5	3295.5	-3267.5	------	------	------	------
NR	Top	3276.5	-3251.5	3267.5	-3242.5	------	------	------	------	------	------
NR	Bottom	3278.0	-3253.0	3268.5	-3243.5	------	------	------	------	------	------

* Tops and bottoms of reservoir units crossed twice by horizontal wells.
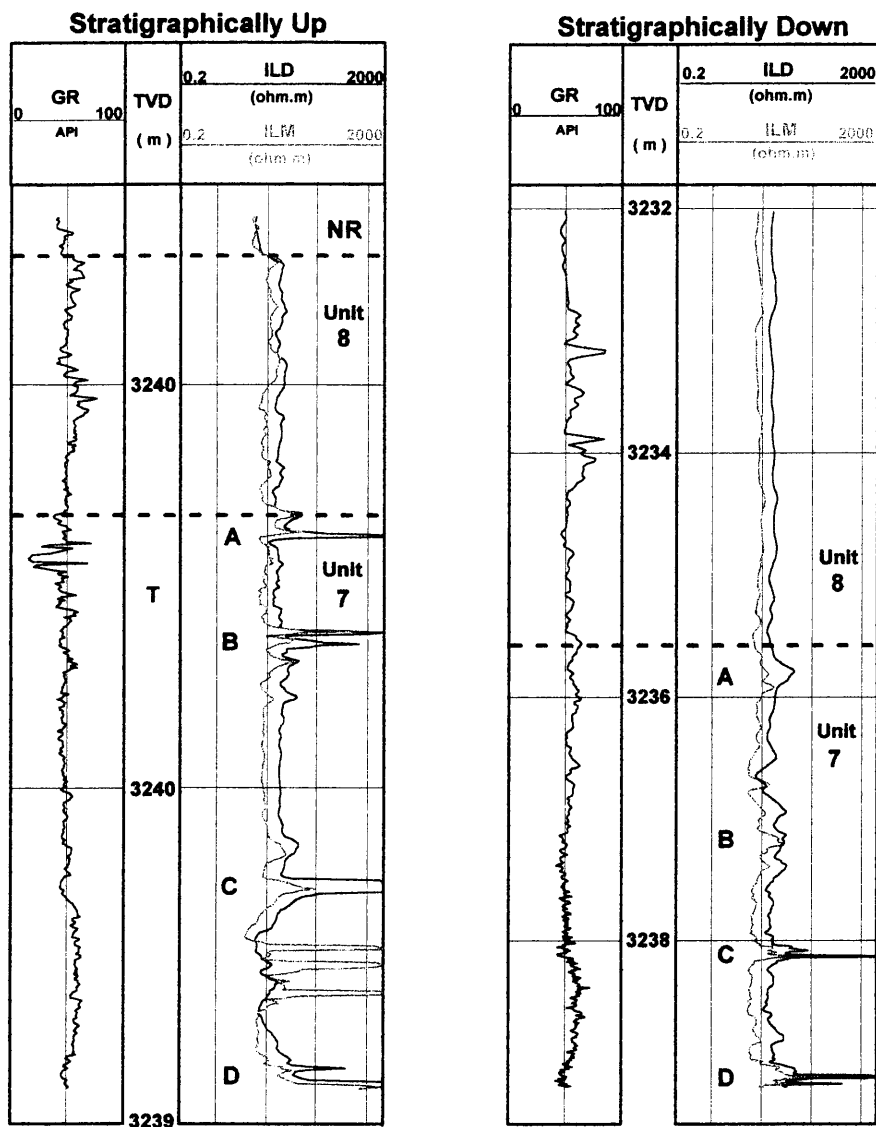
Figure 31 - True vertical depth (tvd) plots for the ABH-1 well. Plots are displayed to correlate repeated sections along the horizontal path. The lower stratigraphic position is reached at the base of Unit 7 (correlation point D). Note that the lowest tvd depth at 3240.6 m (point T in the left plot) is reached when the well is already going up stratigraphically (see **Figure 29**). **A, B, C**, and **D** are correlative points. Resistivities are plotted on a semi-log scale. Vertical scales on tvd plots are different.
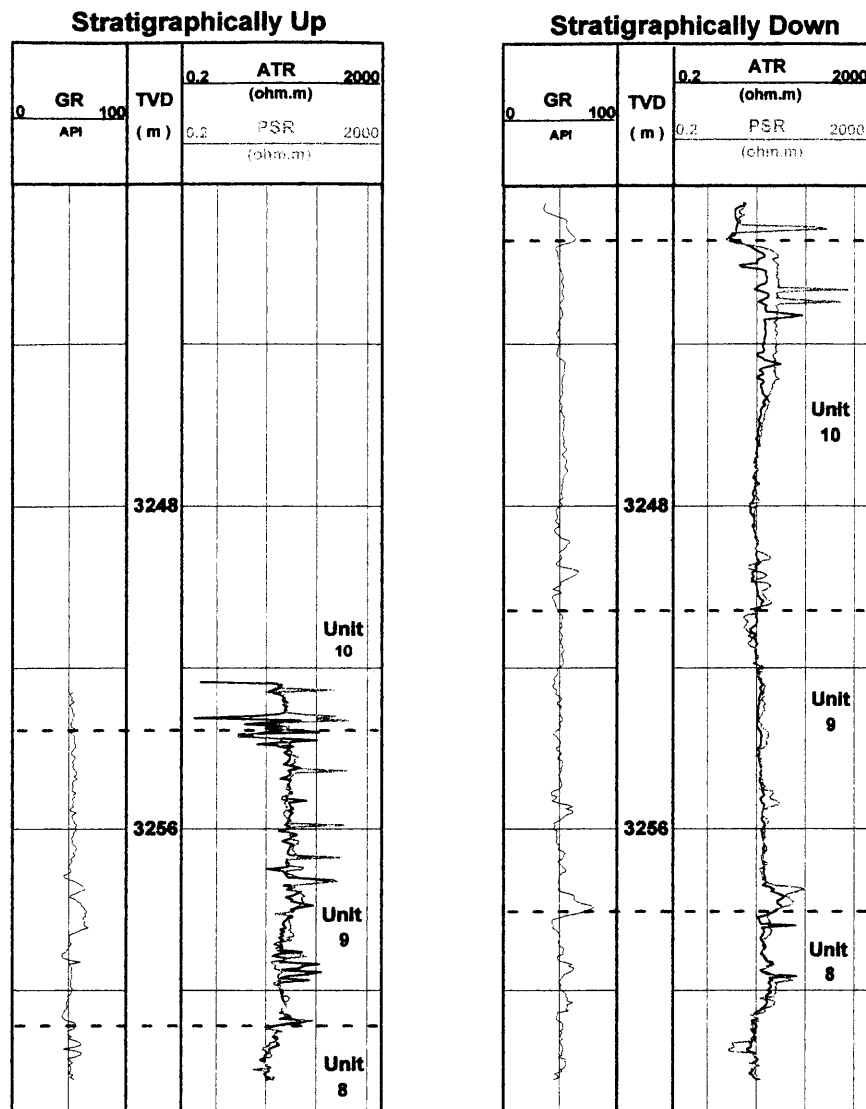
Figure 32 - True vertical depth (tvd) plots for theABH-2 well. Tops of units 7 and 8 are crossed twice by the well trajectory (see **Figure 30**). The lowest stratigraphic position, in the upper part of unit 8, is coincident with the lowest tvd measurement. Resistivities are plotted on a semi-log scale.

2 degrees SW, are crossed by the horizontal well in deviation angles from 70 to 94 degrees. After crossing reservoir units 10 and 9, the well reaches the lowest stratigraphic position in the upper part of unit 8. From this point, the well climbs stratigraphically, crossing again unit 9 and reaching the final depth at the base of unit 10. **Figure 33** shows the same geologic section along the trajectory of well ABH-2, changing the display of the LWD resistivity log to the 1120 hours time-lapse resistivity pass.

4.2 Petrophysical Model

The most complete cored section of the reservoir units was taken in vertical well ABV-2 **(Figure 34)**. This core data was used to build a detailed petrophysical profile for units 7 to 11, using core descriptions and, porosity and permeability measurements from plugs and mini-permeameter. The conventional logs available in the studied section have vertical resolutions that cannot distinguish the individual reservoir heterogeneities. The use of mini-permeameter measurements with 1 to 10 cm vertical spacing on slabbed cores provides a way to characterize the distinct lithologic intervals. These were then upscaled with tool modeling for correlation with the log measurements.

4.2.1 Lithologic Classes

For the purpose of this study, the sedimentary facies described in Chapter 3 were grouped into three main lithologic classes: reservoir sandstone (**R**), cemented sandstone (**C**) and non-reservoir rock (**NR**). The reservoir sandstone class is represented by both the
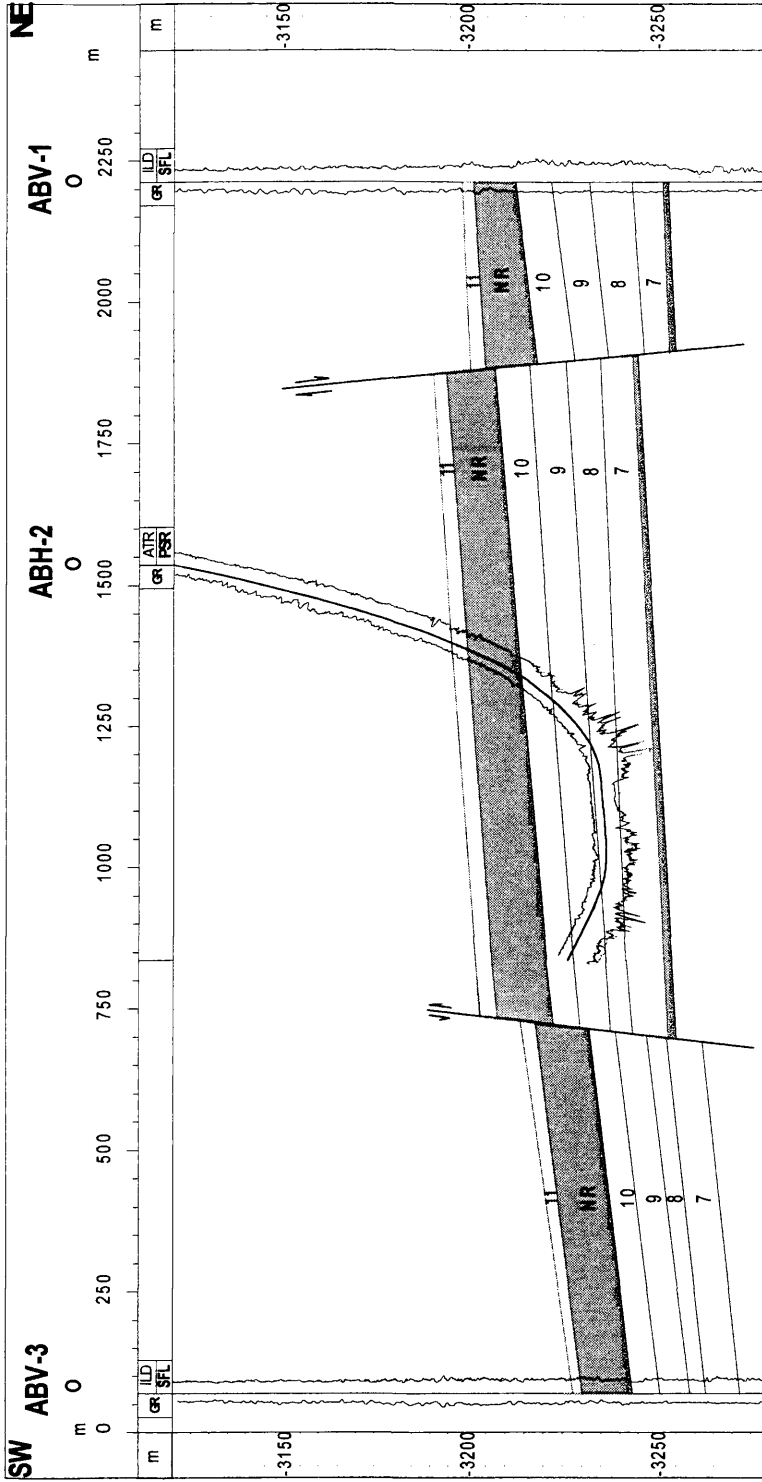
Figure 33 - Geologic section along the path of ABH-2 horizontal well. Time-lapse logs obtained 1120 hours after drilling (ATR, PSR, and gamma ray curves) are displayed along the horizontal trajectory. Offsetting vertical wells are displayed with ILD, SFL and gamma ray curves. NR = non-reservoir. Numbers 7 through 11 are reservoir units.
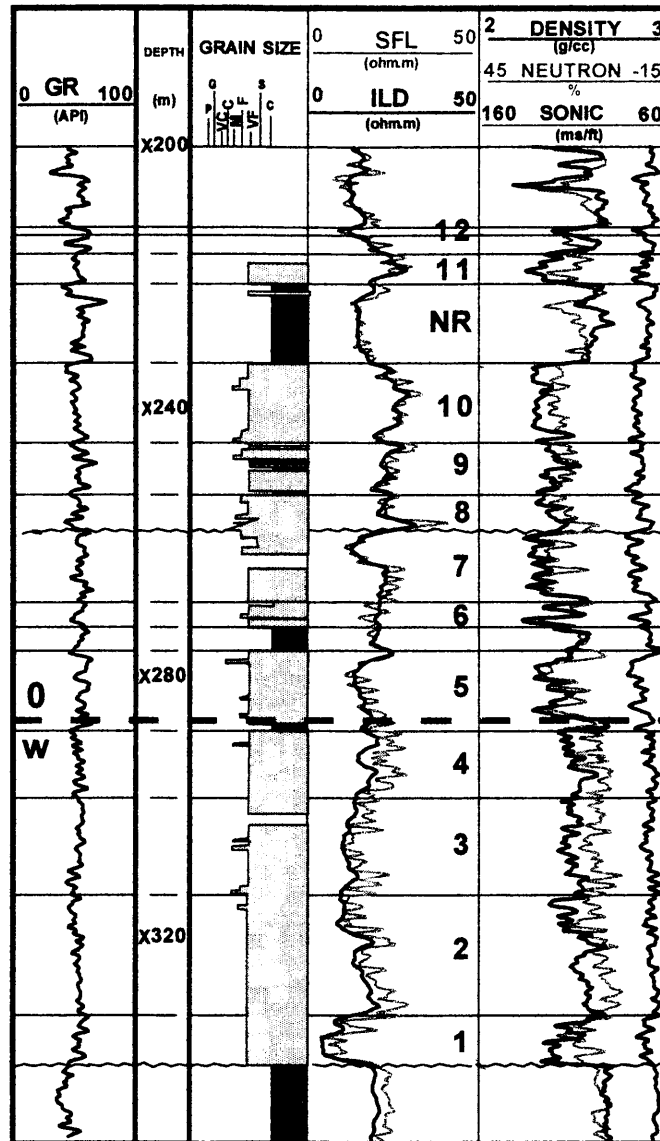
Figure 34 - Cored section of well ABV-2 with the 12 reservoir units of the Upper Albian turbidites in Albacora field. The main reservoir interval comprises the lowermost turbidite succession (units 1 to 10). Calcite cementation was inhibited above the oil-water contact (O-W), resulting in significant porosity contrast above and below this depth. Resistivities are plotted on a semi-log scale.

massive and Bouma sequence facies, corresponding to permeabilities above 10 md. The cemented sandstone class is represented by the same two facies, but with permeabilities less than 10 md, as a result of calcite cementation. The non-reservoir rocks are represented by the shale, marl, calcilutite and diamictite facies, also with very low permeability values. Class **R** was further subdivided according to standard permeability ranges of 10-50 md (**R4**), 50-100 md (**R3**), 100-500 md (**R2**), and above 500 md (**R1**). Lithologic classes and sub-classes were recognized on core photos and separated along reservoir units 7 to 11, in 50 m of continuous cores from well ABV-2. Because, in the studied cores, the intensity of oil stains is directly proportional to reservoir quality, this criterion was used to help define limits for the reservoir sandstone sub-classes **R1** to **R4**. Examples of the lithologic classification based on core photos and descriptions are presented for reservoir units 10 and 9/8 in **Figures 35** and **36**. A 3-m subset of the classification, including the reservoir sandstone sub-classes **R1** to **R4** is presented in **Figure 37.**

4.2.2 Heterogeneity Distribution

The total distribution of lithologic classes and mini-permeameter measurements for reservoir units 7 to 10 is shown in **Figure 38**. Gamma ray and resistivity logs are also displayed showing the poor resolution of the conventional logs for the thin reservoir heterogeneities. The petrophysical profiles reveal distinct vertical distribution of heterogeneities along the reservoir units. Unit 10 is characterized by a very low frequency
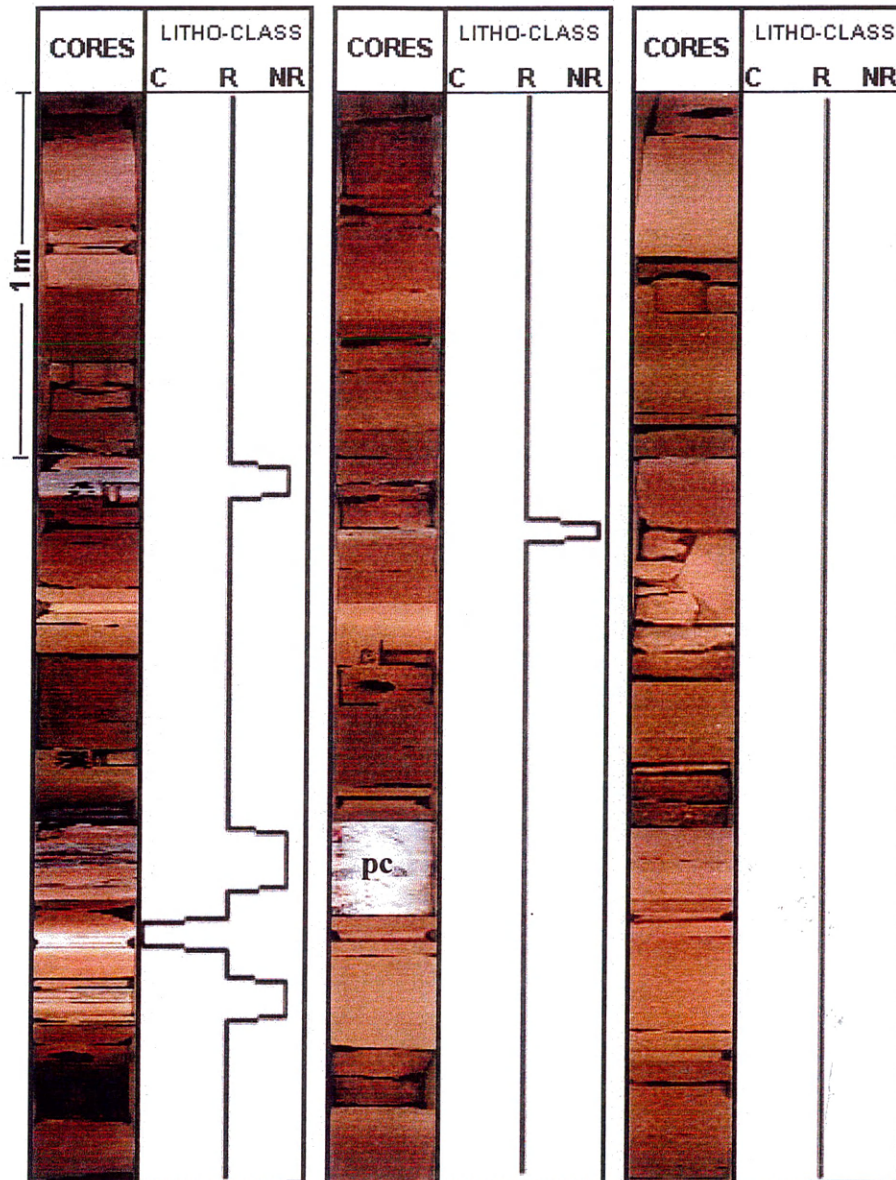
Figure 35 - Lithologic classification for reservoir unit 10. Lithologic classes are (**C**): cemented sandstone; (**R**): reservoir sandstone and (**NR**): non-reservoir rock. Cored interval is 3233.8 - 3242.8 m; (**pc**) is a preserved core piece of reservoir sandstone.
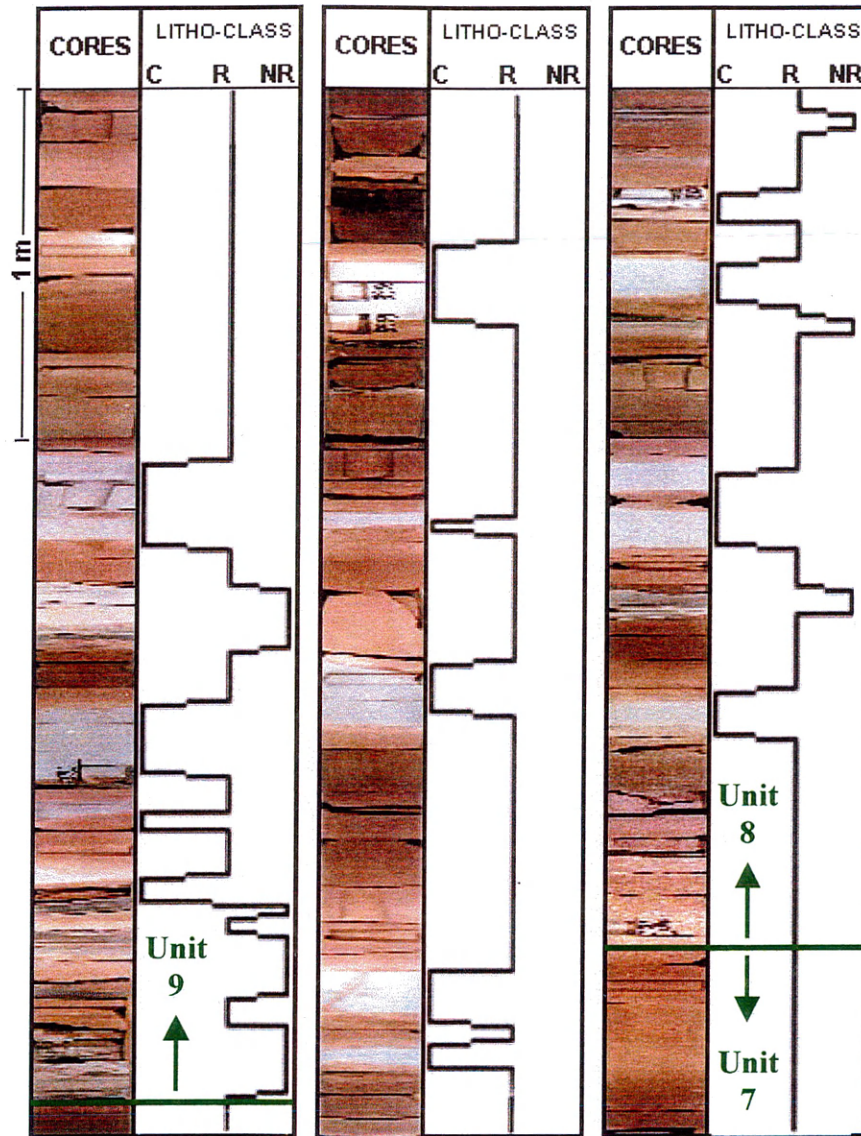
Figure 36 - Lithologic classification for reservoir units 9 (base), 8 and 7 (top). Cored interval is 3248.8 - 3257.8 m. Lithologic classes as in Figure 36.
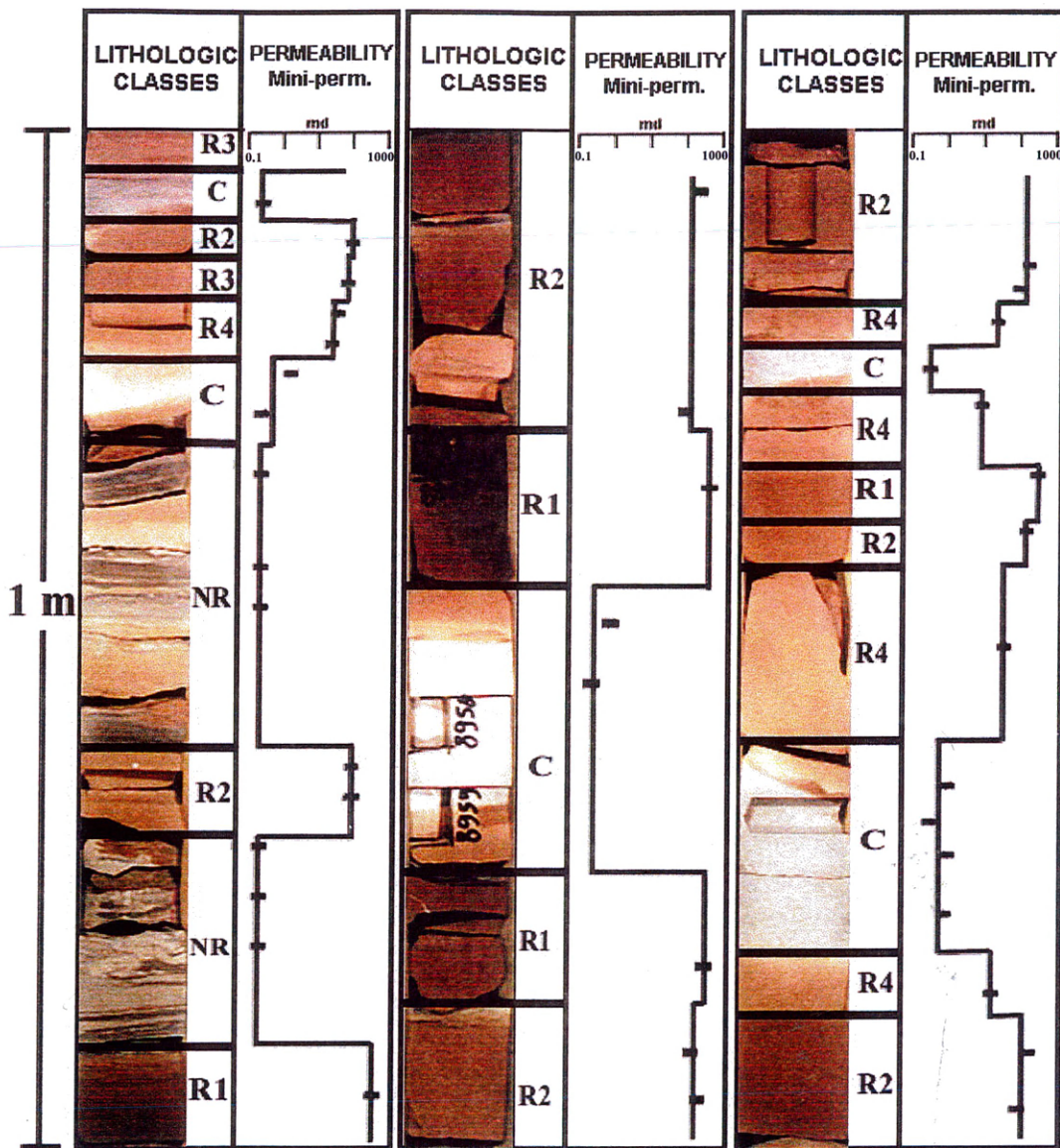
Figure 37 - Distribution of defined lithologic units for 3 m of cored section in well ABV-2: reservoir sandstone (**R1** - **R4**), cemented sandstone (**C**) and non-reservoir rock (**NR**). Reservoir sandstone sub-classes were defined according to permeability ranges of 10-50 md (**R4**), 50-100 md (**R3**), 100-500 md (**R2**), and above 500 md (**R1**). Oil stain intensity is directly proportional to reservoir quality and helps establish reservoir sub-class boundaries. Dots are mini-permeameter permeabilities.
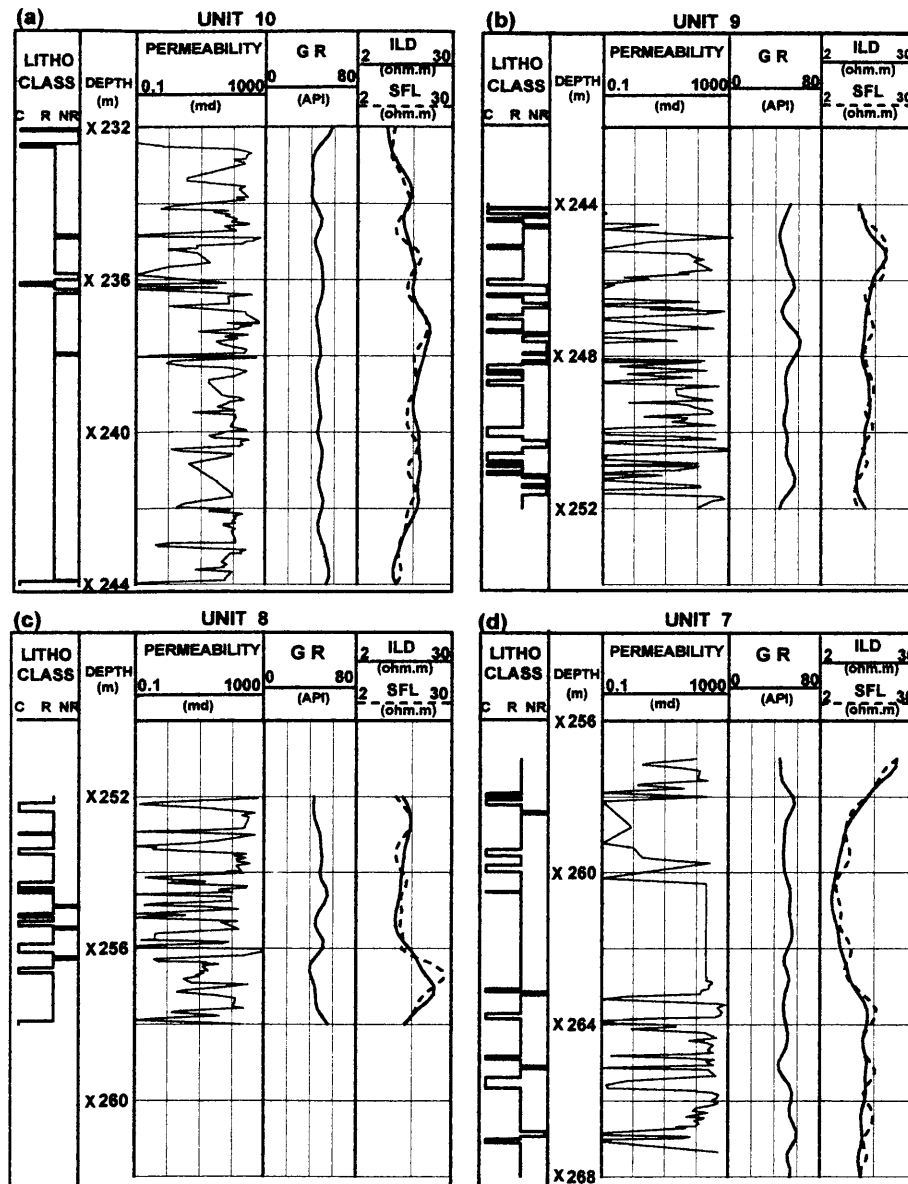
Figure 38 - Heterogeneity distribution along four reservoir units of well ABV-2. Unit 10 (a) has the the lowest frequency of cemented layers (C) and non-reservoir rocks (NR). Unit 9 (b) has the highest frequency of cemented sandstones and non-reservoir rocks. Units 8 and 7 (c and d) have high frequency of cemented layers but smaller amounts of non-reservoir intercalations. Resistivities and permeabilities are plotted on a semi-log scale.

of cemented layers and non-reservoir rocks (**Figure 35**). Also, a visible change in the intensity and contrast of permeability variations occurs from the middle part of the unit, showing much more diversity of the reservoir pore systems in the upper part of this reservoir unit. Unit 9 presents very high frequency of non-reservoir and cemented layers (**Figure 36**), resulting in intense vertical variation of permeabilities. Units 8 and 7 are also characterized by high frequency of cemented sandstones, but with fewer non-reservoir intercalations.

4.2.3 Permeability and Resistivity Transforms

In order to simulate the response of resistivity logs in horizontal wells of Albacora field, the 50 m stratigraphic profile delineated for the vertical well ABV-2 was considered as representative of the overall reservoir variation in the area. A squared resistivity profile along the reservoir units was obtained by converting the mini-permeameter measurements to resistivity values, using the Coates free fluid and Archie equations (Coates and Denoo, 1981):

$$k = \left[100 \; \phi^2 \left(\frac{\phi - BV_{irr}}{BV_{irr}} \right) \right]^2 \tag{1}$$

where k is permeability, ϕ is porosity and BV_{irr} is the bulk-volume of irreducible water, given by the product of total porosity and irreducible water saturation ($BV_{irr} = \phi \, Sw_{irr}$).

Sw_{irr} can be expressed as a function of resistivity (Archie equation):

$$Sw_{irr}^{\ w} = \frac{F\ R_W}{R_t} \qquad (2)$$

where F is the formation factor, Rw is the formation water resistivity, Rt is the formation resistivity, and w is the Coates-Dumanoir exponent (Coates and Dumanoir, 1973) equal to a common value assumed for the porosity exponent (m) and saturation exponent (n).

Resistivity can be expressed in terms of bulk-volume of irreducible water:

$$R_t = \frac{a\ R_w}{BV_{irr}^{\ w}} \qquad (3)$$

where a is the cementation exponent, and BV_{irr} is obtained from permeability and porosity (1).

For the calculations, we considered each distinct lithologic interval as homogeneous and isotropic. We assumed constant porosity values for the reservoir sandstone and non-reservoir rock classes. For the cemented sandstone, porosity was estimated using the log-linear relationship between permeability and porosity on **Figure 39**. The small-scale (1 to 10 cm sample rate) permeability values of each distinct lithologic interval (3 to 75 cm) were up-scaled by a geometric mean. The combined

permeability of each lithologic interval was transformed to resistivity, using equations (1)

and (3) and initial coefficient values of a = 0.81 and w = 2 (Appendix 1).
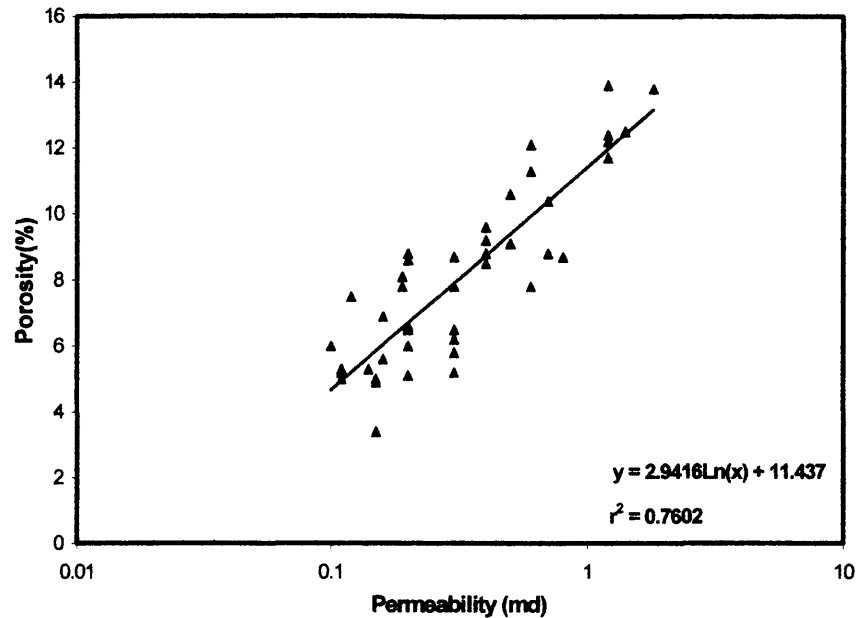
Figure 39 - Porosity vs permeability relationship in the cemented sandstones of well
ABV-2, used to estimate porosity values for the permeability-to-resistivity
transform.

The second step was to compute a resistivity log from the obtained petrophysical

model, and compare it to field resistivity logs from the offsetting vertical well ABV-2, to

adjust the input parameters. A best fit was accomplished using the following

petrophysical constants and coefficients: reservoir sandstone (ϕ = 20%, w = 2.2, a =

0.81); cemented sandstone (ϕ variable, related to k, w = 2.3, a = 0.81); non-reservoir rock

(ϕ = 16%, w = 2.0, a = 0.81). Rw of 0.028 ohm.m was calculated for the reservoir

interval, considering the formation water salinity of 110,000 ppm NaCl. **Figure 40** shows

the final petrophysical model from well ABV-2 with the comparison between the

simulated and field vertical resistivity logs for the entire cored section. A good match

between the simulated 2 MHz resistivity curves and the measured induction logs was

achieved. Local mismatches may be due to the presence of complex lithologies,

variability in clay type and differences in vertical resolution between modeled and field

logs.
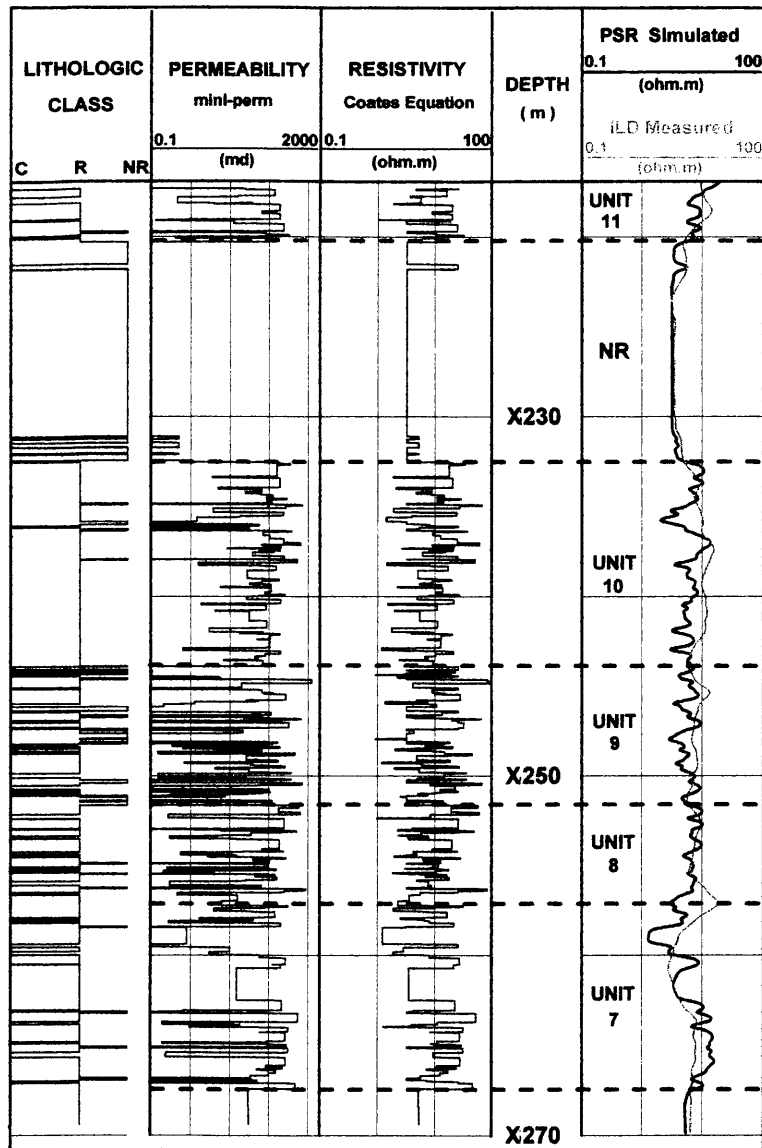
Figure 40 - Petrophysical model from offsetting vertical well ABV-2 along 50 m of cored interval. Mini-permeameter measurements were converted to resistivity using the Coates and Archie equations. The response of a 2 MHz tool was simulated (PSR curve) and compared to the field induction log (ILD curve), to adjust imput parameters. (C): cemented layers, (R): reservoir sandstone, (NR): non-reservoir rock. Resistivities and permeabilities are plotted on a semi-log scale.

CHAPTER 5.

RESISTIVITY MODELING

5.1 - 1D Model

In order to reproduce effects observed on the field resistivity logs of horizontal well ABH-2, the response of a 2 MHz resistivity tool was simulated from the established petrophysical model in Chapter 4, considering two extreme invasion situations. First, no invasion was assumed, to reproduce the initial LWD logs. Then, a complete salt-saturated mud filtrate invasion was taken into account, to reproduce the later time-lapse logs. To reproduce a complete invasion in the reservoir sandstone, the resistivity of the invaded zone (Rxo) was obtained using the salt-saturated mud filtrate resistivity (Rmf) of 0.016 ohm.m at reservoir temperature. The petrophysical constants for the reservoir sandstone were maintained, excepted for the coefficient w, which was lowered to 2.0 in order to reflect the smaller tortuosity expected in the invaded zone. The values of w = 2.2 for the oil saturated zone and w = 2.0 for the invaded zone are consistent with laboratory experiments for these sandstones (Barroso et al., 1997) that found m = 2.0 and n = 2.19. A maximum residual oil saturation of 30% was assumed, giving Rxo = 0.66 ohm.m. In cases where Sw exceeded 70%, Sxo was set equal to Sw. For the cemented sandstone and non-reservoir rocks, no invasion was allowed, so Rxo = Rt.

A 1D resistivity modeling program from Schlumberger (ANISBED) was used to simulate ATR and PSR responses from the resistivity model, considering a horizontal well. The simulation was done considering the tool in a horizontal position, moving vertically along the resistivity model (**Figure 41**). The results (Appendix 2) are shown in **Figure 42**. Polarization horns develop where reservoir sandstones occur adjacent to calcite-cemented layers, after a complete replacement of hydrocarbons by mud filtrate. This fluid replacement provides a sufficient resistivity contrast to generate the polarization horns.

5.2 - 3-D Model

5.2.1 Invasion Model

A conceptual invasion model for the horizontal well ABH-2 was constructed, considering the density contrast between mud-filtrate and formation fluid, the vertical permeability of the reservoir sandstones, and the presence of impermeable reservoir heterogeneities (calcite-cemented sandstones and non-reservoir rocks). The invasion model is presented in **Figure 43**, which displays the evolution of invasion fronts in two types of sandstone reservoirs. Reservoir types were separated by vertical permeability ranges, Type I representing the best reservoir quality, with vertical permeabilities above 100 md (sub-classes **R1** and **R2**), and Type II representing reservoir sandstones with
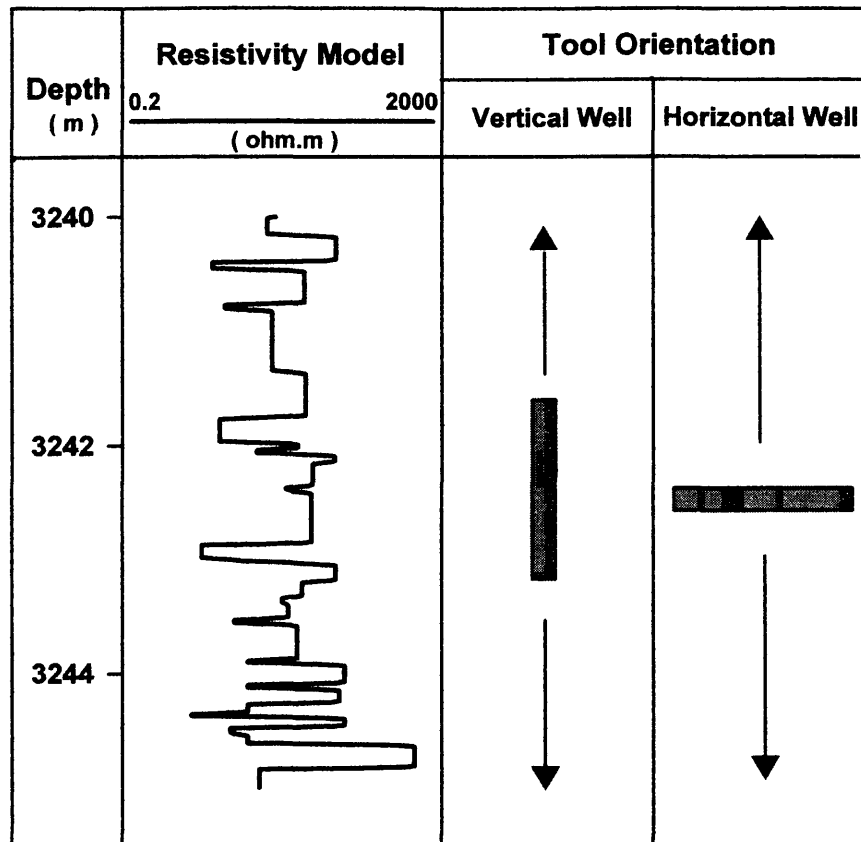
Figure 41 - Resistivity tool response modeling. To simulate log responses in a vertical well, the tool is considered in a vertical position, moving vertically along the resistivity model. To simulate log responses in horizontal wells, the tool is considered in a horizontal position, moving vertically along the resistivity model.

Figure 42 - 2 MHz tool modeled responses for a 90° deviated well using the established resistivity model from cores and mini-permeameter data in well ABV-2. When a complete conductive invasion is considered (right track), polarization horns develop in the positions where reservoir sandstones occur adjacent to calcite-cemented layers. Note that in Unit 10, only one horn was produced after invasion, associated with the cemented sandstone layer (Figure 36). Resistivities are plotted on a semi-log scale.

Figure 43 - Conceptual invasion model for well ABH-2, showing the evolution of a salt-saturated invasion front for two types of sandstone reservoirs. Type I corresponds to the reservoir sub-classes R1 and R2. Type II represents the reservoir sub-classes R3 and R4. Filtrate dissipation is controlled by formation exposure time, vertical permeability, gravitational segregation and the presence of impermeable layers (non-reservoir rocks and calcite-cemented sandstones).

vertical permeabilities less than 100 md (sub-classes **R3** and **R4**) (**Figure 37**). In early exposure times, the invasion pattern is similar for reservoir types I and II because no vertical migration occurs at this time and filtration is only controlled by mud and mud cake properties (Allen et al., 1991). With increasing formation exposure times, filtrate migration occurs only in Type I reservoirs, where the density contrast between the oil and the salt-saturated filtrate causes the latter to flow downward, until it spreads along impermeable cemented or non-reservoir layers. A final scenario is originated where thin, highly conductive "layers" overlie highly resistive calcite-cemented sandstones or low resistivity non-reservoir rocks. In Type II sandstone reservoirs, the low vertical permeabilities are insufficient to allow filtrate migration, and the invasion front grows symmetrically with respect to the borehole.

5.2.2 Electromagnetic Modeling Results

A 3D tool modeling program from Schlumberger (Anderson et al., 1997, 1998) was used to simulate 2 MHz tool response to the symmetric and asymmetric invasion proposed in our model.

The electromagnetic modeling results for symmetric invasion (Appendix 3) are shown in **Figure 44**. The case modeled is a 30 ohm.m layer placed between two 24 ohm.m Rt layers. At the lower interface, a thin 12 ohm.m non-reservoir layer separates the two. Polarization horns do not develop for these relatively small resistivity contrasts when no invasion is considered. A high resistivity contrast is introduced by modeling a
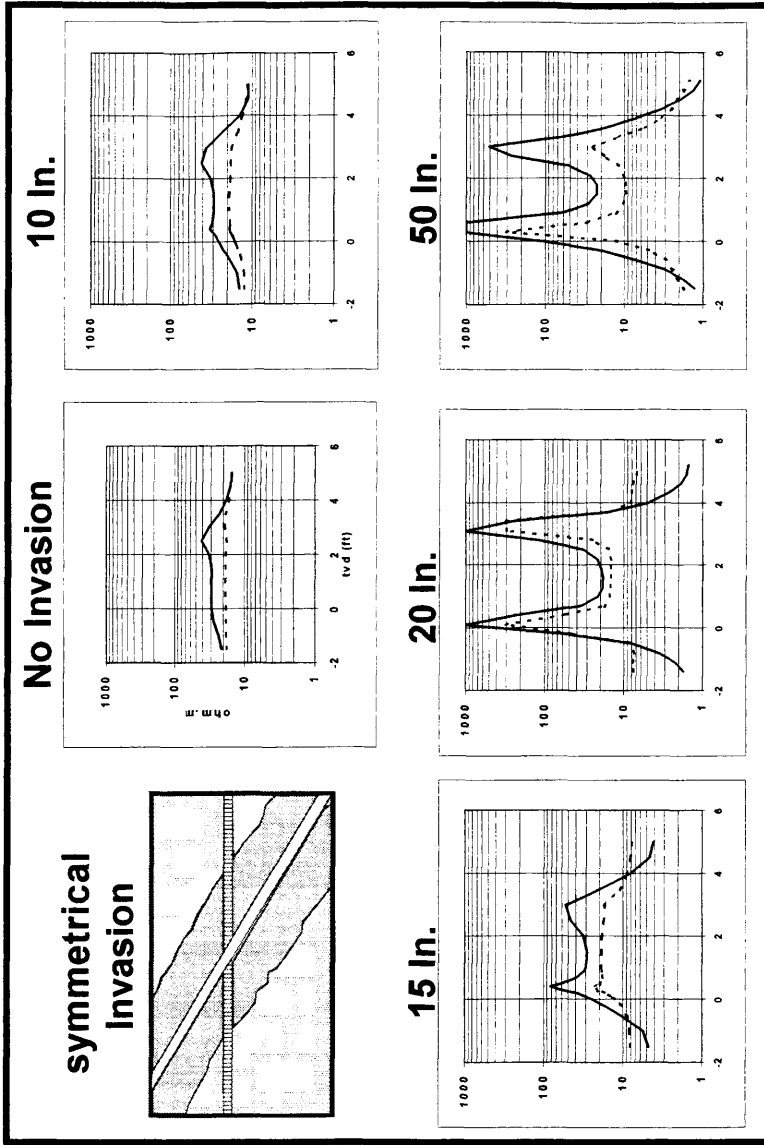
Figure 43 - 3D electromagnetic modeling for symmetric invasion. A minimum invasion radius of 15 to 20 inches is required for polarization horns to develop. Resistivities in vertical axis (ohm.m), PSR solid, and ATR dotted. True vertical depth in horizontal axis (ft).

low resistivity (1 ohm.m) cylinder in the 24 ohm.m layers centered about an 8 1/2 inch

borehole which is inclined at 88 degrees. As the radius of the low resistivity cylinder is

increased, polarization horns are seen to develop. An invasion radius in excess of 15

inches is required to develop horns comparable to those observed on the late time CDR

passes in ABH-2 well (**Figures 4** and **33**). The tool design modeled was a 4 3/4-inch

diameter ARC-5 tool, the phase shift and attenuation resistivity curves displayed are from

the 28-inch spacing and have not been borehole corrected. Borehole corrections were not

applied because they were not found to affect the polarization horns.

The electromagnetic modeling results for an asymmetrical invasion (Appendix 4)

are shown in **Figure 45**. The 1 ohm.m cylinder is modeled as being offset towards one

side of the borehole, as might occur in the presence of gravity segregation. The

simulation shows that a polarization horn develops when the low resistivity zone overlays

the high resistivity zone and the wellbore (**Figure 45a**). When the low resistivity zone is

between the wellbore and the high resistivity zone, a polarization horn does not develop

(**Figure 45b**).

The 3-D modeling results offer important clarification and insight into both the

log response observed in the horizontal well and into polarization horn physics. The

symmetric 3-D modeling (**Figure 44**) clearly shows the development of polarization

horns at the interface between reservoir layers and cemented layers. As is always the

case, the polarization horns on the log develop when the tool is just inside the resistive

layer. As invasion progresses, a low resistivity saturated region is progressively enlarged
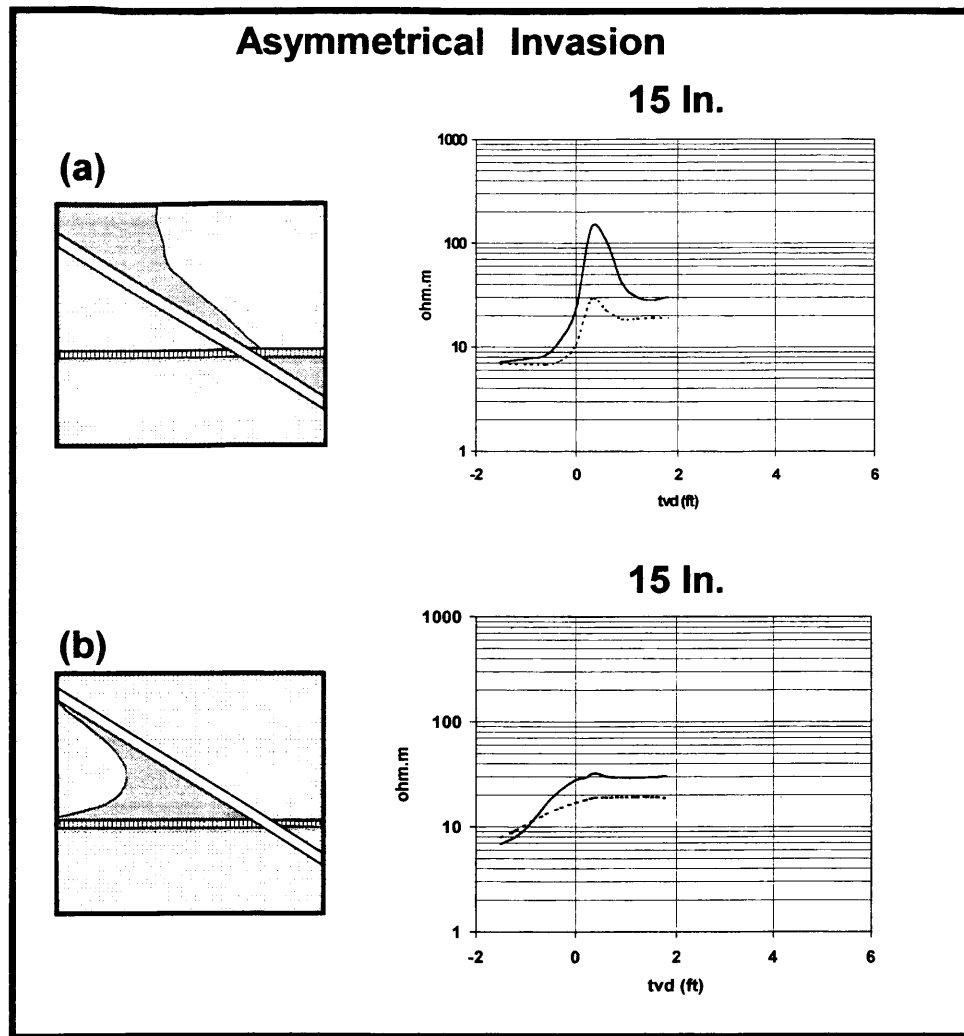
Figure 45 - 3D electromagnetic modeling for asymmetrical invasion. A polarization horn only develops when the low resistivity invaded zone overlies the wellbore and the high resistive cemented layer (a). When the invaded zone is between the wellbore and the cemented layer no polarization horn develops (b). Resistivities in vertical axis (ohm.m), PSR solid, and ATR dotted. True vertical depth in horizontal axis (ft)

around the wellbore in the reservoir sandstones and the polarization horns develop. Once this region exceeds a radius of 15 inches the polarization horns become well developed, consistent both with those observed on the late time CDR passes and with those computed using the 1-D model with Rxo used for the reservoir sand layers. A 20-inch radius of invasion is consistent with that computed for a nearby thick sandstone in this horizontal well by Peeters et al. (1999).

The asymmetrical 3-D modeling results demonstrate that gravity segregation, when present, dramatically reduces polarization horns both at the top and at the bottom of the sands. The vertical migration of mud filtrate, as proposed in **Figure 43**, will reduce the diameter of invasion in the top of the sands, reducing or eliminating polarization horns even at late times after considerable filtrate has been lost. At the same time, at the bottom of the permeable bed, offset of the low resistivity invaded zone beneath the wellbore also retards the development of polarization horns.

The 3-D modeling results add useful insights to our intuitive understanding of polarization horn development (Anderson et al., 1990). The symmetrical modeling results, which show that a considerable diameter of invasion is required for polarization horns to develop, reveals the limitation of the simple claim that the polarization horn phenomenon is a near wellbore effect. If this were the case, then the horns would have developed with just a few inches of invasion. For instance, see the case of 10 inches invasion radius (**Figure 44**). Resolution of the paradox is provided by the offset modeling. **Figure 45** reveals that the polarization horn phenomenon is a near tool effect.

In the geometry studied in **Figure 45a**, the low resistivity zone is very close to the tool while the tool is just inside the resistive layer, and polarization horns develop. In **Figure 45b**, the low resistivity zone is absent once the tool passes into the high resistivity zone.

In the Namorado reservoir of Albacora field, turbidite sandstones with varying permeabilities (Type I, and Type II reservoirs) occur intercalated with calcite-cemented layers. Both symmetric and asymmetric invasion occur along the path of the horizontal wells. The results of our resitivity modeling show that polarization horns are mainly associated with symmetric invaded zones near resistive cemented layers.

CHAPTER 6.

ELECTRICAL AND PERMEABILITY ANISOTROPY

Soares and Coutinho (1997) identified electrically anisotropic intervals in turbidite reservoirs of Albacora field based upon inversion of logging while drilling phase shift and attenuation resistivities (ATR and PSR), and related the differences in horizontal and vertical resistivities to depositional processes. In this work, we used a petrophysical model to quantify electrical anisotropy caused by intervals with or without calcite cementation, and to study the relationships between permeability and resistivity for the two different types of layering in the reservoir.

6.1 - Macroscopic Anisotropy

The vertical and horizontal resistivities for a one-meter window were obtained from the petrophysical model (Chapter 4), using arithmetic and harmonic averages respectively, of the lithologic intervals:

$$Rv = \frac{h_1 \, R_1}{hw} + \frac{h_2 \, R_2}{hw} + \ldots + \frac{h_n \, R_n}{hw} \tag{4}$$

$$Rh = \left[\frac{h_1/hw}{R_1} + \frac{h_2/hw}{R_2} + \ldots\ldots\ldots + \frac{h_n/hw}{R_n} \right]^{-1} \tag{5}$$

where *hw* is the thickness of the window (1 m), *h* is the thickness of the isotropic lithologic interval and *R* is the formation resistivity for the interval, from equations (1) and (3).

The horizontal and vertical permeabilities were obtained by the equations:

$$kv = \left[\frac{h_1/hw}{k_1} + \frac{h_2/hw}{k_2} + \ldots\ldots + \frac{h_n/hw}{k_n} \right]^{-1} \tag{6}$$

$$kh = \frac{h_1\, k_1}{hw} + \frac{h_2\, k_2}{hw} + \ldots\ldots\ldots + \frac{h_n\, k_n}{hw} \tag{7}$$

where *k* is the combined permeability of the isotropic lithologic interval.

Calculated Rv, Rh, Kv and Kh values for the entire cored section of ABV-2 well are presented in Appendix 5.

6.2 - Evolution of Electrical Anisotropy with Invasion

The resistivity anisotropy after invasion was obtained using equations (4) and (5), changing *R* to Rxo from the salt-saturated filtrate (Appendix 6). The new vertical and

horizontal resistivity values were named Rvsal and Rhsal, respectively. The obtained Rv, Rh, Rvsal and Rhsal values, displayed for units 7 to 10 in **Figure 46**, were used to analyze the resistivity anisotropy evolution with invasion. Unit 10 represents the best example of electrical anisotropy related to depositional processes, whereas unit 9, with the higher frequency of calcite-cemented layers, is representative of electrical anisotropy related to diagenesis (**Table 3**). Comparison of electrical anisotropy evolution between these two units shows that while the electrical anisotropy related to depositional processes in unit 10 tends to disappear with invasion, the electrical anisotropy related to calcite cementation in unit 9 increases with invasion. The electrical anisotropy in reservoirs with or without calcite cementation is affected in different ways by hydrocarbon saturation. In the first case the anisotropy effect tends to disappear with increasing water saturation, whereas in the second case this effect increases with water saturation.

6.3 - Permeability and Resistivity Relationships

In a layered formation, permeability and resistivity are averaged by the formation according to the same two laws: the vertical permeability and horizontal resistivity of the bulk formation are the harmonic average of the permeabilities and resistivities of the individual layers (equations 5 and 6). The horizontal permeability and vertical resistivity are the arithmetic average of the individual layers (equations 4 and 7). This symmetry in
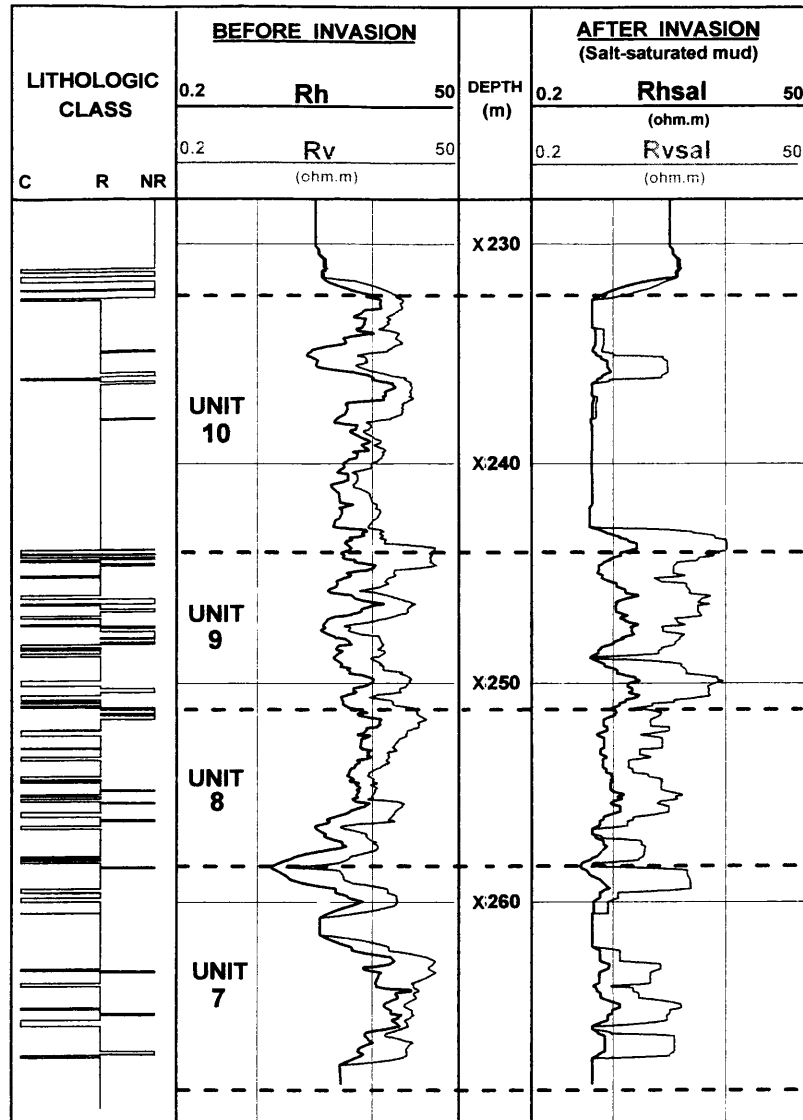
Figure 46 - Evolution of electrical anisotropy with invasion for different anisotropy-related processes. In unit 10, depositional processes cause electrical anisotropy, which tends to disappear with the evolution of invasion (Rvsal/Rhsal = 1). In units 9, 8 and 7, electrical anisotropy is related to diagenetic processes, and the anisotropy ratio increases with the invasion process. Resistivities are plotted on a semi-log scale.

response yields the paradoxical conclusion that in anisotropic formations, vertical permeability is computed from horizontal resistivity, and horizontal permeability from vertical resistivity (Klein et al., 1995). These relationships can be understood if we consider that in hydrocarbon-saturated formations the electrical resistivity is directly proportional to permeability. This occurs because as the flow path for the fluid (hydrocarbon volume) is increased, the flow path for electric current (irreducible water volume) is decreased. The resistivity and permeability relationships in anisotropic formations are explained in **Figure 47**. The horizontal permeability is dominated by the highest permeability layer, and the vertical permeability is dominated by the lowest permeability layer. Conversely, the horizontal resistivity is dominated by the lowest

Oil Saturated Sandstone		
layer 1	k = 100 md	Rt = 30 ohm.m
layer 2	k = 10 md	Rt = 2 ohm.m
layer 3	k = 30 md	Rt = 10 ohm.m

Figure 47 - Diagram showing an example of permeability and resistivity relationships in anisotropic hydrocarbon-saturated sandstone. Horizontal permeability and vertical resistivity are dominated by layer 1, whereas vertical permeability and horizontal resistivity are dominated by layer 2.

resistivity layer, and the vertical resistivity by the highest resistivity layer. In summary, both the vertical resistivity and the horizontal permeability are dominated by the same layer. Exactly the same correlation is obtained for horizontal resistivity and vertical permeability.

An extension of the Coates free fluid permeability equation to anisotropic formations (Klein et al. 1995) was used to calculate the horizontal permeability from our petrophysical model:

$$kh = \left[100 \; \phi^2 \; \frac{\left(\phi - BV_{irraniso}\right)}{BV_{irraniso}}\right]^2 \tag{8}$$

in which:

$$BV_{irraniso} = \sqrt{\frac{\phi^2 F \, R_w}{R_v}} \tag{9}$$

where Rv was computed as the arithmetic mean of the resistivities of all of the layers within a one-meter sliding window, and porosity (ϕ) was the mean porosity in the same sliding window.

The result is compared with the actual horizontal permeability (the arithmetic mean of the layer permeabilitites) in **Figure 48**, and is seen to agree extremely well. Vertical permeability, computed using Rh in equation (9) does not compare well with the actual vertical permeability (**Figure 49**). This is because the presence of cemented layers
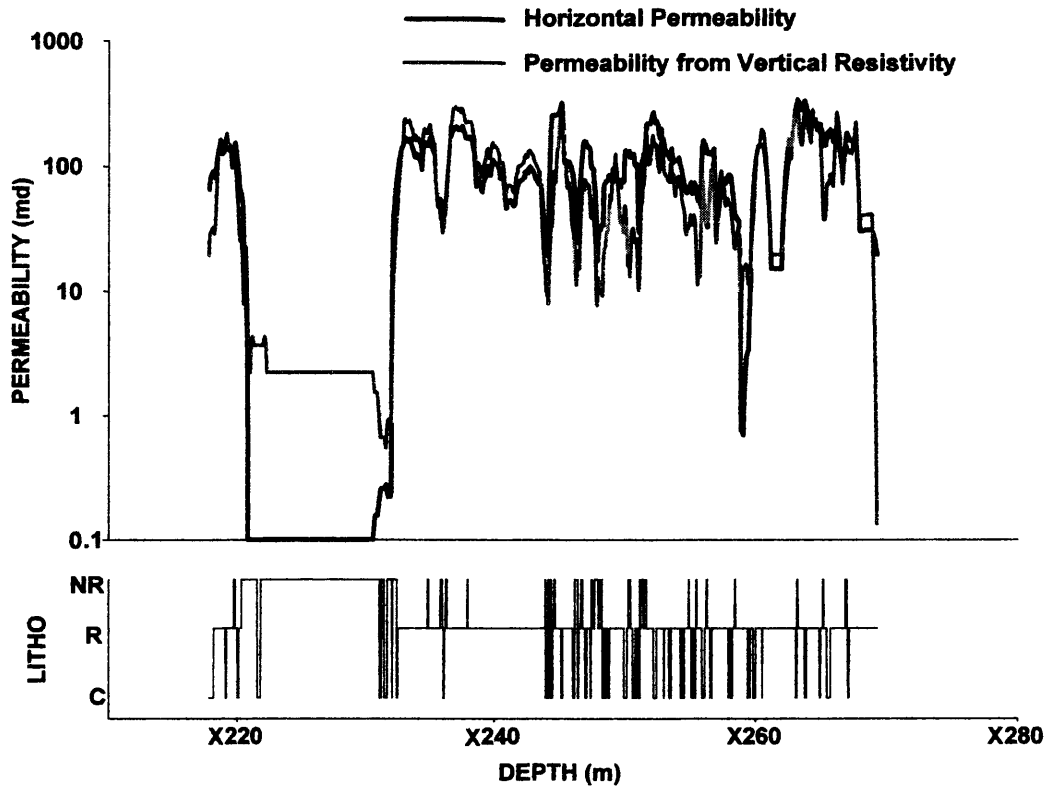
Figure 48 - Comparison between horizontal permeability from the arithmetic average of individual layers, and permeability from Coates and Archie equations. Permeabilities obtained from vertical resistivity agree extremely well with horizontal permeabilities in anisotropic intervals with or without calcite cementation.
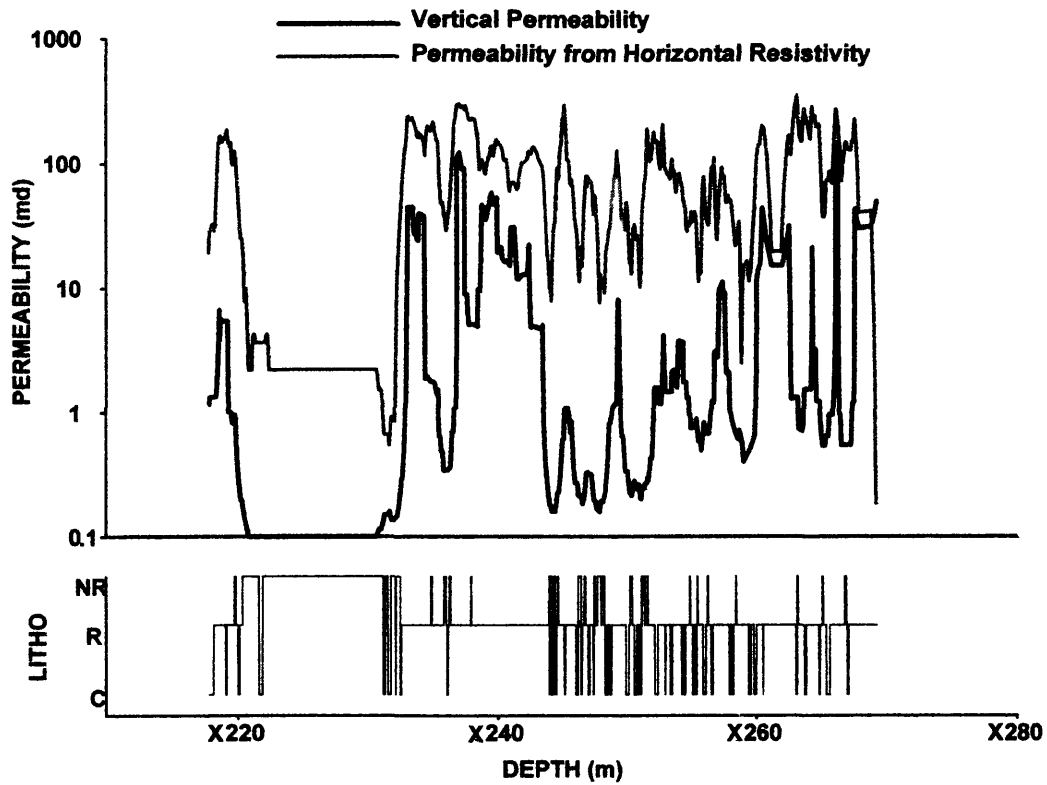
Figure 49 - Comparison between vertical permeability from the harmonic average of individual layers, and permeability from Coates and Archie equations. The presence of cemented-layers strongly influences vertical permeability, preventing a good correlation.

affects the vertical permeability to a much greater extent than they affect the horizontal resistivity.

Computed values for Kv and Kh using Coates and Archie equations and the arithmetic and harmonic means of the layer permeabilities are presented in Appendix 7.

CHAPTER 7.

FORWARD MODELING

The petrophysical properties obtained from the cored vertical well and the reservoir geometry from the geologic correlations (Chapter 4) were integrated using a 1D forward modeling program from Schlumberger (INFORM), to simulate resistivity logs along the trajectory of the horizontal wells ABH-2 and ABH-1.

7.1 - Horizontal well ABH-2

First, the response of a 2 MHz resistivity tool was simulated along the entire horizontal trajectory of well ABH-2 for a non-invaded situation to reproduce the measured real-time logs. The results are shown in **Figure 50**. The reconstructed resistivity curves match the measured logs, with main anisotropic intervals being indicated by separations between the PSR and ATR curves. Second, the defined invasion model was used to simulate 120 meters of the horizontal trajectory, to reconstruct the time-lapse logs. A petrophysical model, considering a complete salt-saturated mud filtrate invasion adjacent to resistive cemented layers, was assumed in the position where horns occurred in the field time-lapse logs. **Figure 51** shows the results of the simulation, with polarization horns being reproduced, matching the field logs.
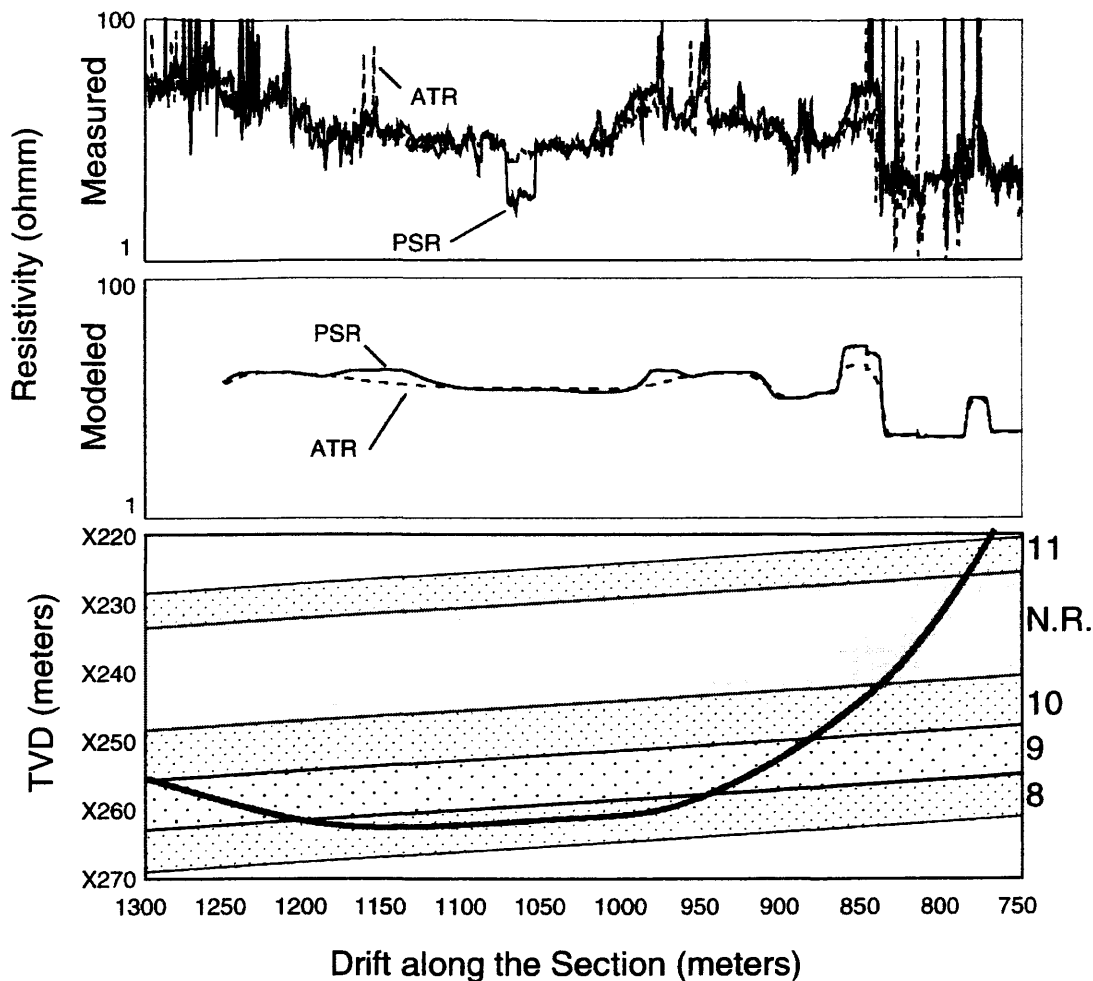
Figure 50 - Forward resistivity modeling for a 2 MHz tool along the horizontal trajectory of well ABH-2, considering no invasion. The modeled resistivity curves match the measured real-time logs. Main anisotropic intervals are indicated by separation between PSR and ATR curves. A large separation between PSR and ATR curves at 1055-1070 m indicates a cored interval where logs were measured after drilling and were affected by invasion. Reservoir units **11, 10, 9** and **8** are indicated on the right side of cross section. **NR** is the non-reservoir interval.
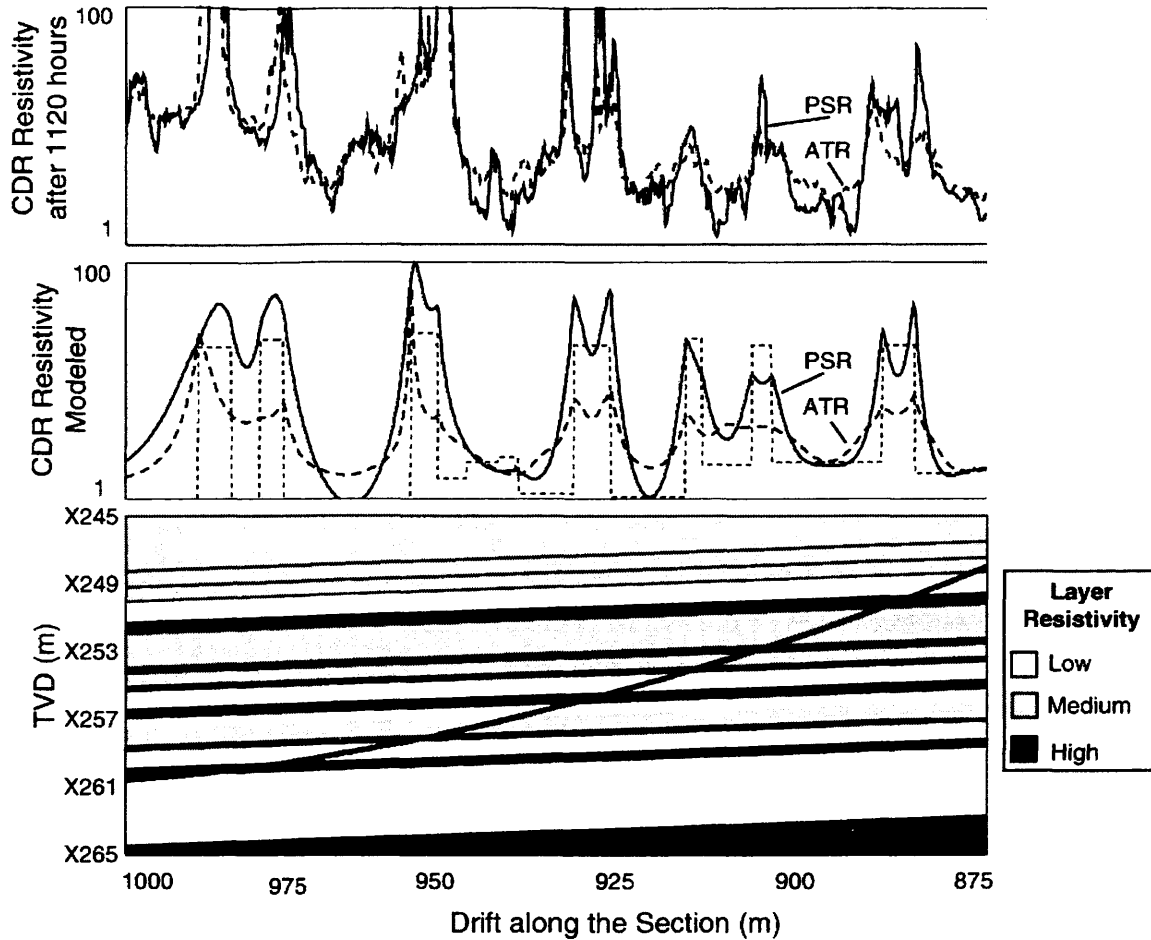
Figure 51 - Forward resistivity modeling for 120 m of the horizontal trajectory of ABH-2 well, showing the measured and reconstructed polarization horns. The geologic section is presented in a resistivity scale from black (high resistivity) to white (low resistivity).

7.2 - Horizontal Well ABH-1

The reservoir geometry along the trajectory of well ABH-1 (**Figure 29**) was reproduced in INFORM to model the induction logs (**Figure 52**). The established petrophysical model for the reservoir was loaded, now considering invasion of a brackish mud filtrate (Rmf = 0.058 ohm.m at reservoir temperature), resulting in Rxo of 2.39 ohm.m in the invaded reservoir. The induction tool response was simulated along the 200 meters section where unit 7 was crossed twice in the well path (**Figure 53**). Four resistive cemented layers were stratigraphically placed in reservoir unit 7 to reproduce the polarization horns of the field log. The reconstructed induction log shows growing horns at the position of the cemented layers. The presence of a horn effect is evident by the shape of the induction curve, which distinguishes it from a normal tool response for a resistive layer. Because the resistivity contrast created by brackish filtrate invasion is smaller than for salt-saturated filtrate invasion, the size of the polarization horns in the reconstructed induction logs of well ABH-1 are smaller than the ones modeled for the 2 MHz resistivity logs of well ABH-2. Differences in polarization horn intensities between reconstructed and measured induction logs could be related to sonde error effects or the presence of locally higher resistive cemented layers.

Correlation between the position of polarization horns in the reconstructed and measured induction logs can give clues about the lateral distribution of calcite-cemented layers in unit 7. The modeled induction log (**Figure 53**) shows that the well crosses downward three resistive cemented layers (a, b and c) and then goes up stratigraphically,
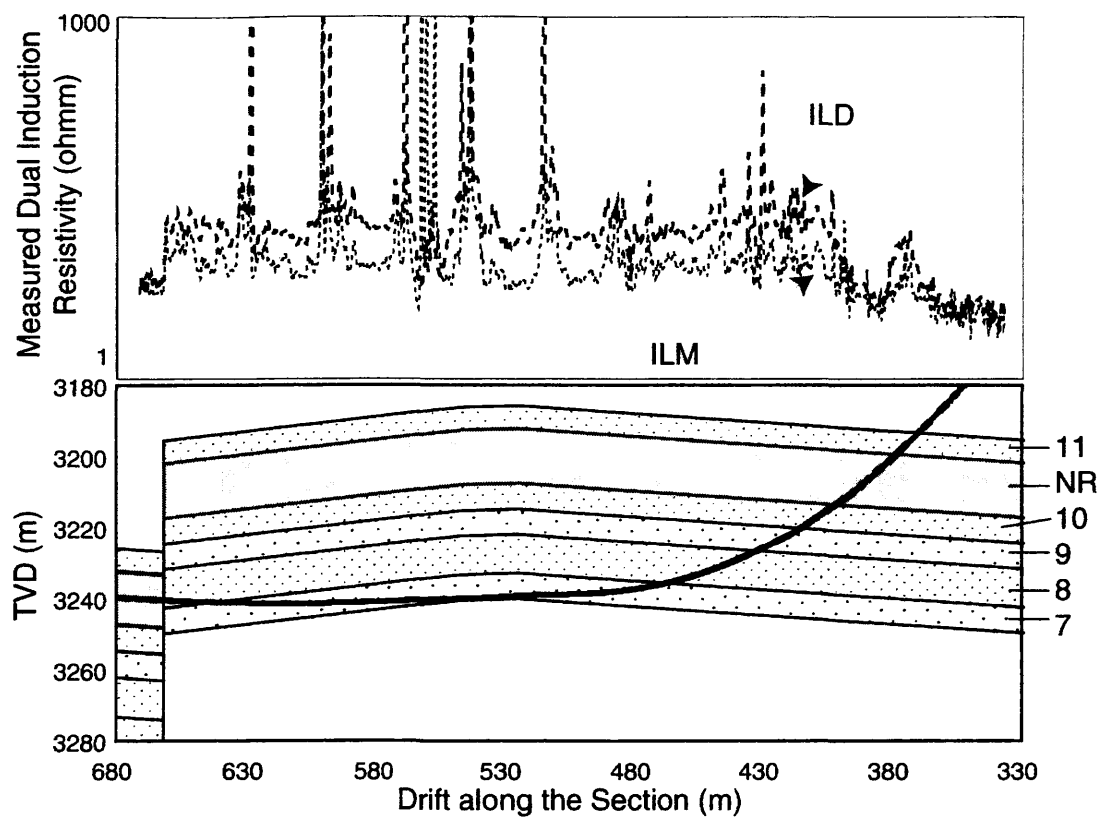
Figure 52 - Geologic model along the trajectory of horizontal well ABH-1 showing that the well crossed reservoir units 8 and 7 twice, and left the reservoir after reaching a normal fault. This reservoir geometry was used to reconstruct the measured induction logs.
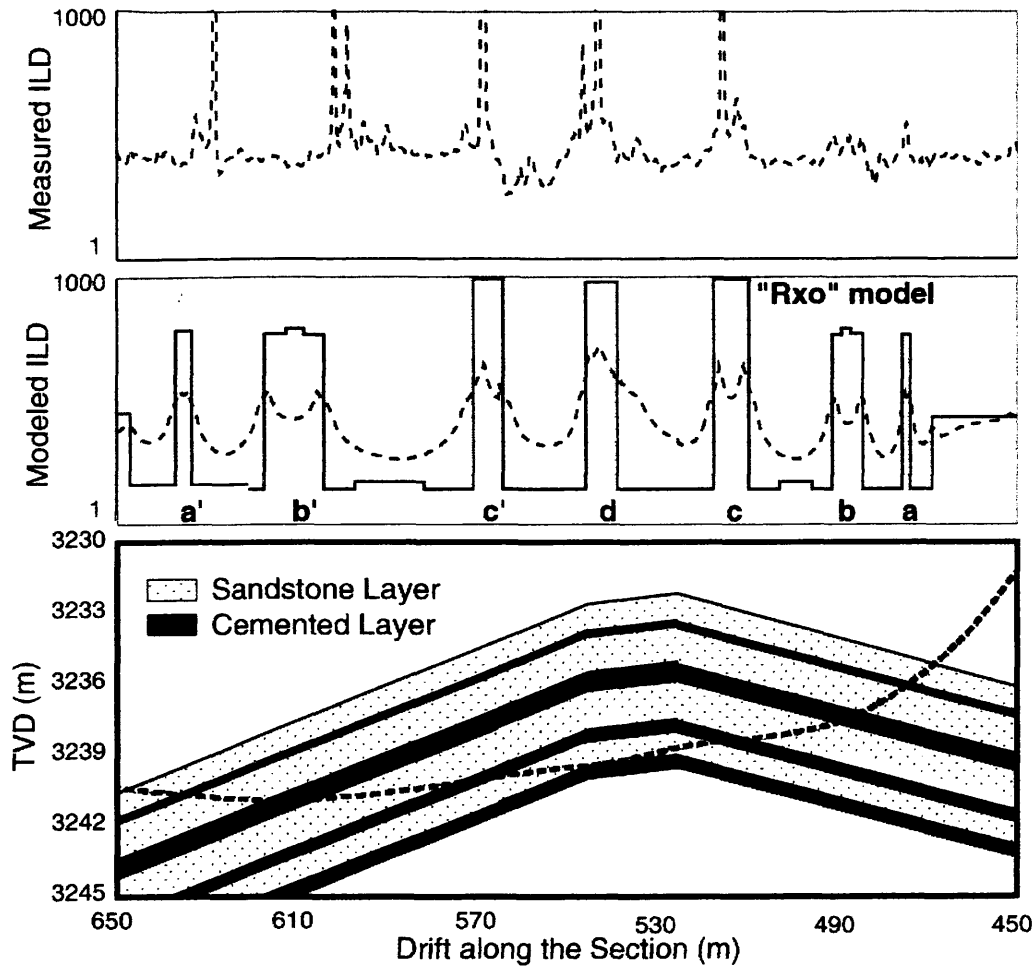
Figure 53 - Forward resistivity modeling along 200 m horizontal trajectory of well ABH-1 showing reservoir unit 7 being crossed twice by the well path. Four resistive cemented layers (a, b, c, and d) were modeled to reproduce the polarization horns of measured induction logs. Correlation between the position of measured and reconstructed polarization horns shows that only one modeled cemented layer (c) has a mirror image (c') precisely matching the field logs, indicating a lateral continuity of 60-70 m.

traversing again the upper three resistive layers, with stretched mirror images being created at positions a', b' and c'. Correlation with measured logs shows that slight depth shifts occur between predicted and measured horns for images a' and b'. This may be caused by errors in measured depth (Loermans et al., 1999), slight changes in stratigraphic thickness, or discontinuities in the cemented layers. For cemented layer c, a mirror image of the polarization horn (c') was reconstructed exactly in the same measured depth of a field log polarization horn. This allows us to interpret a lateral continuity of at least 60-70 m for this cemented layer.

CHAPTER 8.

DISCUSSION

Polarization horns and electrical anisotropy are important environmental effects acting in highly deviated and horizontal wells. For polarization horns to develop, a high relative dip angle and resistivity contrast is necessary. The invasion process can significantly modify the electrical properties in a reservoir, causing sufficient resistivity contrasts to grow polarization horns that were absent in a non-invaded situation. Electrical anisotropy is related to layered formations, which can originate from textural and pore geometry variations or diagenetic alterations in a reservoir. Both polarization horns and electrical anisotropy cause anomalously high resistivity readings, particularly in highly deviated and horizontal wells. These resistivity log anomalies must be appropriately identified and corrected in the well log evaluation process.

The Namorado reservoir of Albacora field provides an ideal situation and opportunity to study polarization horns and electrical anisotropy effects in resistivity logs. The turbidite sandstones were deposited above carbonate sediments, which sourced cation-rich fluids for calcite cementation in the reservoir. The calcite-cemented zones reduced oil productivity and recovery efficiency, leading to the use of horizontal wells to

develop the reservoir. In the horizontal wells, these carbonate-cemented zones caused resistivity log anomalies, related to electrical anisotropy and polarization horns.

LWD resistivity logs with time-lapse runs proved to be an essential tool for the study of electrical anisotropy and polarization horn effects in the horizontal well logging environment. A petrophysical model of the reservoir, from well logs and core data, and a conceptual invasion model were used to simulate resistivity measurements before and after invasion. Comparison between reconstructed logs and the logging while drilling and logging after drilling passes (LWD and MAD) led to the main conclusions in the evolution of polarization horns and electrical anisotropy during a progressive invasion process in horizontal wells.

This research should result in significant benefits. A better understanding of the main effects acting in the horizontal well log environment is needed to obtain correct reservoir resistivities for fluid saturation computations and hydrocarbon reserve estimations. The work has also identified a new methodology to recognize and correlate thin cemented layers in horizontal wells drilled with conductive mud. If the horizontal well crosses the same interval more than one time, polarization horns can be correlated along the trajectory. This gives important clues about the lateral continuity of these internal reservoir heterogeneities. Finally, the log interpretation approach applied in the horizontal wells of Albacora field can be extrapolated to other areas with horizontal well projects, helping in the formation evaluation process.

CHAPTER 9

CONCLUSIONS

Conventional wireline logs provided insufficient detail to determine the cause of polarization horns and electrical anisotropy observed in a 2MHz LWD log run in a turbidite sandstone reservoir. Instead, this study required a combination of core in a offset vertical well, extensive mini-permeameter readings, a geologic model which included correlations to the horizontal well, a petrophysical model that incorporated observed porosities, permeabilities, and resistivities, and an invasion model. The study also required time-lapse resistivity logs and a modeling approach that matched observed to predicted log traces.

The following conclusions were obtained for the studied reservoir:

1- Polarization horns develop at the boundary between high resistivity cemented layers and permeable reservoir sandstones after invasion by a conductive mud filtrate. The radius of invasion must exceed 15 inches for horns to develop in the case studied. Vertical segregation of mud filtrate can eliminate horns at the top and bottom of highly permeable reservoirs.

2- Reservoir anisotropy was observed as a result of both depositional and diagenetic processes. The first is related to pore geometry and textural variations in a massive sandstone. The second is due to the presence of calcite-cemented sandstones.

3- Hydrocarbon saturation affects electrical anisotropy in different ways, depending on the genesis of the anisotropy effect, which can be either depositional or diagenetic. In the first case the anisotropy effect tends to disappear with increasing water saturation, whereas in the second case this effect increases with water saturation.

4- Vertical resistivity is a robust indicator of reservoir quality in reservoirs with anisotropy related to the presence of calcite-cemented layers. Horizontal permeability may be quantified from vertical resistivity in anisotropic reservoirs with or without calcite-cemented layers.

5- Vertical permeability can be obtained from horizontal resistivity in reservoirs with anisotropy related to depositional processes, but this correlation does not apply to reservoirs with anisotropy related to the presence of calcite-cemented layers.

6- In horizontal wells, where vertical resistivity and horizontal resistivity are inverted from 2 MHz tool data at the well site, vertical resistivity should be used as an indicator of reservoir producibility.

7- The use of an integrated forward modeling program to simulate polarization horns along the horizontal well trajectories enriched the knowledge of the lateral distribution of cemented layers in the reservoir. In the ABH-1 horizontal well, a lateral continuity of at least 70 meters was interpreted for one of the cemented layers.

8- The integration of vertical and horizontal well data sets in a turbidite reservoir

of Albacora field enhanced the knowledge of resistivity log responses in horizontal wells.

The above conclusions for the studied reservoir can be extrapolated to aid resistivity log

interpretation in other areas with horizontal wells and LWD measurements.

NOMENCLATURE

a	=	cementation exponent
BV_{irr}	=	bulk-volume of irreducible water
$BV_{irraniso}$	=	bulk-volume of irreducible water in anisotropic formations
F	=	formation factor
h	=	formation thickness
hw	=	window thickness
k	=	formation permeability
kh	=	horizontal permeability
kv	=	vertical permeability
m	=	cementation exponent
n	=	saturation exponent
r^2	=	regression coefficient
Rh	=	horizontal resistivity
Rv	=	vertical resistivity
Rhsal	=	horizontal resistivity of salt-saturated invaded zone
Rvsal	=	vertical resistivity of salt-saturated invaded zone
Rmf	=	mud-filtrate resistivity

Rt	=	formation resistivity
Rw	=	formation water resistivity
Rxo	=	invaded zone resistivity
Sw	=	water saturation
Sw_{irr}	=	irreducible water saturation
w	=	Coates-Dumanoir exponent
ϕ	=	porosity fraction
λ	=	anisotropy coefficient
ARC-5	=	array resistivity compensated tool
ATR	=	attenuation resistivity curve
ARI	=	azimuthal resistivity imager tool
AIT	=	array induction imager tool
BHA	=	borehole assembly
CDR	=	compensated dual resistivity tool
CWRGD	=	compensated wave resistivity-gamma ray-directional tool
DIL	=	dual induction resistivity log
DIFL	=	dual induction focused log
DITE	=	phasor-dual induction tool
DLL	=	dual laterolog resistivity tool
DPIL	=	dual phase induction log
HALS	=	azimuthal laterolog sonde

HRI	=	high resolution induction tool
ILD	=	induction log deep curve
ILM	=	induction log medium curve
INFORM	=	integrated forward modeling program
LLD	=	laterolog deep curve
LLS	=	laterolog shallow curve
LWD	=	logging while drilling
MAD	=	measurement after drilling
MCFL	=	micro-cylindrically focused logging tool
MSFL	=	micro-spherically focused logging tool
PSR	=	phase-shift resistivity curve
RAB	=	resistivity-at-the-bit
R Bit	=	bit resistivity curve
R Lat	=	lateral resistivity curve
ROP	=	rate of penetration
SFL	=	spherically focused log
TBRT	=	thin-bed resistivity tool

REFERENCES

Abreu, C. J., Arienti, L. M., Backheuser, Y., Cândido, A., and Adams, T., 1992. Qualidade dos reservatórios turbidíticos do Arenito Namorado no Campo de Albacora, Bacia de Campos. PETROBRÁS/CENPES Internal Report, 182 p.

Allen, D. F., Auzerais, D., Dussan, E., Goode, P., Ramakrishnan, T. S., Schwartz, L., Wilkinson, D., Fordhan, E., Hammond, P., and Williams, R., 1991. Invasion revisited. Oilfield Review, v. 3, No. 3, p.10-23.

Allen, D. F., Anderson, B., Barber, T., Liu, Q. H. and Lüling, M., 1993. Supporting interpretation of complex, axisymmetric invasion by modeling wireline induction and 2-MHz LWD resistivity tools. SPWLA 34th Annual Logging Symposium, Calgary, Canada, June 1993, Paper U.

Anderson, B., Bonner, S., Lüling, M., and Rosthal, R., 1990. Response of 2-Mhz LWD resistivity and wireline induction tools in dipping beds and laminated formations. SPWLA 31st Annual Logging Symposium, Lafayette, LA, June 1990, Paper A.

Anderson, B., Bryant, I., Lüling, M., Spies, B., and Helbig, K., 1994. Oilfield anisotropy: its origin and electrical characteristics. Oilfield Review, v. 6, No. 4, p. 48-56.

Anderson, B., Barber, T., and Lüling, M., 1995. The response of induction tools to dipping anisotropic formations. SPWLA 36th Annual Logging Symposium, Paris, France, June 1990, Paper D.

Anderson B., Druskin V., Lee, P., Lüling, M. G., Schoen, E., Tabanou, J., Wu, P., Davydycheva, S., and Knizhnerman, L, 1997. Modeling 3D effects on 2-MHz LWD resistivity logs. SPWLA 38th Annual Logging Symposium, Houston, TX, June 1997, Paper N.

Anderson, B., Barber, T. D., and Gianzero, S. C., 1998. The effect of crossbedding anisotropy on induction tool response. SPWLA 39th Annual Logging Symposium, Keystone, Colorado, May 1998, Paper B.

Arienti, L. M., Backheuser, Y., Abreu, C. J., and Cândido, A., 1995. Estratigrafia e modelo deposicional do Arenito Namorado do Campo de Albacora, Bacia de Campos. Boletin de Geociências da Petrobrás, v. 9, p. 249-263.

Barber, T. D. and Howard, A. Q., 1989. Correcting the induction log for dip effect. SPE paper 19607, SPE 64th Annual Technical Conference and Exhibition, San Antonio, TX, p. 371-380.

Barroso, A. S., Bruhn, C. H. L., Lopes, M. R. F., Beer, R., Sombra, C. L., Romeu, R. K., Mihaguti, M., and Neto, G. S., 1997. The impact of reservoir characterization on oil exploitation from the Namorado sandstone, Albacora field, Campos basin, offshore Brazil. SPE paper 38987, Latin American and Caribbean SPE Conference and Exhibition, Rio de Janeiro, Brazil.

Betts, P., Blount, C., Broman, B., Clark, B., Hibbard, L., Louis, A. and Oosthoek, P., 1990. Acquiring and interpreting logs in horizontal wells. Oilfield Review, v. 2, p. 34-51.

Bittar, M., and Rodney, P., 1994. The effects of rock anisotropy on MWD electromagnetic wave resistivity sensors. SPWLA 35th Annual Logging Symposium, Tulsa, OK, June 1994, Paper PP.

Bonner, S., Fredette, M., Lovell, J., Montaron, B., Rosthal, R., Tabanou, J., and Wu, P., 1996. Resistivity while drilling - images from the string. Oilfield Review, Spring, 1996, p. 4-19.

Bruhn, C. H. L., and Moraes, M. A. S., 1988. Turbiditos Brasileiros: caracterização geométrica e faciológica. In Proceedings of the 35th Brazilian Geological Congress, Sociedade Brasileira de Geologia, Belém, Brazil, v. 2, p. 824-838.

Bruhn, C. H. L., Barroso, A. S., Abreu, C. J., Suarez, C. R., Stank, C. V., and Sarzenski, D. J., 1995. Arcabouço geológico do Arenito Namorado no Campo de Albacora, Bacia de Campos. PETROBRÁS/CENPES Internal Report.

Bruhn, C. H. L., and Walker, R. G., 1995. High-resolution stratigraphy and sedimentary evolution of coarse-grained canyon-filling turbidites from the Upper Cretaceous transgressive megassequence, Campos Basin, offshore Brazil. Journal of Sedimentary Research, v. B65, No. 4, p. 426-442.

Bruhn, C. H. L., Barroso, A. S., Lopes, M. R. F., Sarzenski, D. J., Abreu, C. J., and Silva, C. M. A., 1998. High-resolution stratigraphy and reservoir heterogeneities of Upper

Albian turbidite reservoirs of Albacora field, Campos Basin, offshore Brazil. AAPG Annual Convention, Salt Lake City, Utah, May 1998.

Bruhn, C. H. L., 1998. Petroleum geology of rift and passive margin turbidite systems: Brazilian and worldwide examples. AAPG International Conference and Exhibition, Rio de Janeiro, Brazil, November 1998, Part 2, Course 6.

Cândido, A., and Corá, C. A. P., 1992. The Marlin and Albacora giant fields, Campos basin, offshore Brazil. In Michel T. Halbouty ed., Giant oil and Gas Fields of the Decade 1978-1988: AAPG Memoir 54, p. 123-135.

Carvalho, M. V., De Ros, L. F., and Gomes, N. S., 1995. Carbonate cementation patterns and diagenetic reservoir facies in the Campos basin Cretaceous turbidites, offshore Eastern Brazil. Marine and Petroleum Geology, v. 12, No. 7, p. 741-758.

Chang, H. K., Kowsmann, R. O., and Figueiredo, A. M. F., 1988. New concepts on the development of East Brazilian marginal basins. Episodes, v. 11, p. 194-202.

Chemali, R., Gianzero, S.C., Strickland, R., and Tijani, S. M., 1983. The shoulder bed effect on the dual laterolog and its variation with the resistivity of the borehole fluid. SPWLA 24th Annual Logging Symposium, Calgary, Canada, June 1983, Paper UU.

Chemali, R., Gianzero, S.C., and Su, S.M., 1987. The effect of shale anisotropy on focused resistivity devices. SPWLA 28th Annual Logging Symposium, London, England, June 1987, Paper H.

Chin, W., Suresh, A., Holbrook, P., Affleck, L., and Robertson, H. 1986. Formation evaluation using repeated MWD logging measurements. SPWLA 27th Annual Logging Symposium, Houston, TX, June 1986, Paper U.

Coates, G. R., and Dumanoir, J. L., 1973. A new approach to log derived permeability. SPWLA 14th Annual Logging Symposium, Lafayette, LA, May 1973, Paper R.

Coates, G. R. and Denoo, S., 1981. The producibility answer product. The Technical Review, v. 29, No. 2, p. 55-63.

Cunningham, A. B., Jay, K. L., and Opstad, E. A., 1990. Application of MWD technology in nonconventional wells, Prudhoe Bay, North Slope, Alaska. SPWLA 31st Annual Logging Symposium, Lafayette, LA, June 1990, Paper D.

Dias-Brito, D., 1982. Evolução paleoecológica da Bacia de Campos durante a deposição dos calcilutitos, margas e folhelhos da Formação Macaé (Albiano e Cenomaniano?). Boletin Técnico da Petrobrás, v. 25, No. 2, p. 84-97.

Figueiredo, A. M. F., and Mohriak, W. U., 1984. A tectônica salífera e as acumulações de petróleo da Bacia de Campos. In Proceedings of the 33rd Brazilian Geological Congress, Sociedade Brasileira de Geologia, Rio de Janeiro, Brazil, v. 3, p. 1380-1394.

Fordham, E. J., Ladva, H. K. J., Hall, C., Baret, J. F., and Sherwood, J. D., 1988. Dynamic filtration of bentonite muds under different flow conditions. SPE paper 18038, SPE 63rd Annual Technical Conference and Exhibition, Houston, TX, p. 219-226.

Gianzero, S., Chemali, R., and Su, S. M., 1989. Induction, resistivity, and MWD tools in horizontal wells. SPWLA 30th Annual Logging Symposium, Denver, Colorado, June 1989, Paper N.

Guardado, L. R., Gamboa, L. A. P., and Lucchesi, C. F., 1990. Petroleum geology of the Campos basin, Brazil: a model for a producing Atlantic-type basin. In Edwards, J. D., and Santogrossi, P. A. eds., Divergent/Passive Margin Basins: AAPG Memoir 48, p. 3-79.

Hagiwara, T., 1992. Macroscopic anisotropy model: analysis of thinly laminated sand/shale binary formations. Third Archie Conference, October 1992.

Hagiwara T., 1994. Response of 2MHz resistivity devices in thinly laminated formations (anisotropic resistivity and EM log interpretation). SPE paper 28426, SPE 69th Annual Technical Conference and Exhibition, New Orleans, LA, p. 667-676.

Hagiwara,T., 1995. Induction log analysis of thinly laminated sand/shale formation, SPE Formation Evaluation, June 1995, v. 10, No. 2, p. 86-90.

Hagiwara T., 1996. A new method to determine horizontal-resistivity in anisotropic formations without prior knowledge of relative dip. SPWLA 37th Annual Logging Symposium, New Orleans, LA, June 1996, Paper Q.

Haq, B. U., Hardenbol, J., and Vail, P. R., 1988. Mesozoic and Cenozoic chronostratigraphy and cycles of sea-level changes: an integrated approach. SEPM Special Publication 42, p. 71-108.

Howard, A.Q., and Chew, W.C., 1989. A variational model of induction logging in a dipping bed environment. IGARSS Symposium, Vancouver, Canada, July 1989, Paper 5.

Klein, J., 1991. Induction log anisotropy corrections. SPWLA 32nd Annual Logging Symposium, Midland, TX, June 1991, Paper T.

Klein, J.D., Martin, P.R., and Allen, D. F., 1995. The petrophysics of electrically anisotropic reservoirs. SPWLA 36th Annual Logging Symposium, Paris, France, Paper HH.

Koutsoukos, E. A., and Dias-Brito, D., 1987. Paleobatimetria da Margem Continental do Brasil durante o Albiano. Revista Brasileira de Geociências, v. 17, p. 86-91.

Loermans, A. M., Kimminau, S., and Bolt, H., 1999. On the quest for depth. SPWLA 40th Annual Logging Symposium, Oslo, Norway, June 1999, Paper B.

Lowe, D. R., 1982. Sedimentary gravity flows: II. Depositional models with special reference to the deposits of high density turbidity currents. Journal of Sedimentary Petrology, v. 52, p. 279-297.

Lüling, M., Rosthal, R., and Shray, F., 1994. Processing and modeling 2-MHz resistivity tools in dipping, laminated, anisotropic formations. SPWLA 35th Annual Logging Symposium, Tulsa, OK, June 1994, Paper QQ.

Martins, F. A. L., Sad, A. R. E., Scarton, J. C., Oliveira, J. Q., and Moreira, J. L. P., 1990. Mapeamento regional dos turbiditos da Bacia de Campos: do Neo-Albiano ao Mioceno. In Proceedings of the 4th Brazilian Petroleum Congress, Instituto Brasileiro do Petróleo, Rio de Janeiro, Brazil.

McBride, E. F., Milliken, K. L., Cavazza, W., Cibin, V., Fontana, D., Picard, M. D., and Zuffa, G. G., 1995. Heterogeneous distribution of calcite cement at the outcrop scale in Tertiary sandstones, Northern Apennines, Italy. AAPG Bulletin, v. 79, No. 7, p. 1044-1063.

Meyer, W. H., Maher, T., and McLean, D. J., 1996. New methods improve interpretation of propagation resistivity data. SPWLA 37th Annual Logging Symposium, New Orleans, LA, June 1996, Paper O.

Moraes, M. A. S., 1989. Diagenetic evolution of Cretaceous-Tertiary turbidite reservoirs, Campos basin, Brazil. AAPG Bulletin, v. 73, No. 5, p. 598-612.

Moran, J. H., and Gianzero, S., 1979. Effects of formation anisotropy on resistivity-logging measurements. Geophysics, v. 44, No. 7, p. 1266-1286.

Peeters, M., Allen, D., Gomes, R. M. R., and Kristiansen, J. I., 1999. Invasion in space and time. SPWLA 40th Annual Logging Symposium, Oslo, Norway, June 1999, Paper A.

Singer, J., 1992. An example of log interpretation in horizontal wells. The Log Analyst, v. 33, No. 2, p. 85-95.

Slatt, R. M., and Hopkins, G. D., 1990. Scaling geologic reservoir description to engineering needs. Journal of Petroleum Technology, February 1990.

Soares, G. F., and Coutinho, M. R., 1997. Identification of electrical anisotropy in Cretaceous turbidite reservoirs through log simulation in horizontal wells. SPE paper 39012, SPE Latin American and Caribbean Conference and Exhibition, Rio de Janeiro, Brazil, September 1997.

Sombra, C. L., Souza, R. S., Silva, C. M. A., and Pereira, C. A. F., 1995. Camadas cimentadas por calcita no Arenito Namorado, Campo de Albacora. PETROBRÁS/CENPES Internal Report.

Souza, R. S., Silva, C. M. A., Backheuser, Y., and Anjos, S. M. C., 1995. Caracterização integrada dos sistemas porosos do Arenito Namorado, no Campo de Albacora, Bacia de Campos. PETROBRÁS/CENPES Internal Report.

Souza, R. S., and Silva, C. M. A., 1998. Origin and time of calcite cementation in the Namorado sandstone, Albacora field, offshore Brazil: implications for oil recovery. In: Morad, S., ed., Carbonate Cementation in Sandstones, International Association of Sedimentologists Special Publication, London, No. 26, p. 309-325.

Walderhaug, O., and Bjorkum, P.A., 1998. Calcite cement in shallow marine sandstones: growth mechanisms and geometry. In: Morad, S., ed., Carbonate Cementation in Sandstones, International Association of Sedimentologists Special Publication, London, No. 26, p. 179-192.

Woodhouse, R., Opstad, E. A., and Cunninghan, A. B., 1991. Vertical migration of invaded fluids in horizontal wells. SPWLA 32nd Annual Logging Symposium, Midland, Texas, June 1991, Paper A.

York, P., Donovan, M., and Chemali, R., 1992. Horizontal hole vs. vertical hole well log evaluation: the differences. Conexpo Arpel Conference, Rio de Janeiro, Brazil, p. 1-12.